

**OPTIMIZATION OF BRACHYTHERAPY
TREATMENT PLANNING
USING ADJOINT FUNCTIONS**

by

SUA YOO

A dissertation submitted in partial fulfillment of
the requirement for the degree of

Doctor of Philosophy
(Medical Physics)

at the
UNIVERSITY OF WISCONSIN – MADISON
2003

© Copyright by Sua Yoo 2003

All rights reserved

Acknowledgements

This work was pursued from fall 1999 to summer 2003 in the Department of Medical Physics at the University of Wisconsin – Madison. Dr. Douglass Henderson, who has been my advisor during my graduate studies, offered me this project in 1999. This offer was the very first step, which introduced the field of radiation therapy to me. I would like to thank Dr. Henderson. He was patient with my slow learning at the beginning and generous to allow various opportunities to me. Most of all, I appreciate him for letting me contribute to this study.

Regarding this project, I would like to thank Dr. Bruce Thomadsen and Michael Kowalok. Dr. Thomadsen reviewed my papers, and gave direction to my research, commented about research results, and offered me great clinical opportunities. I also would like to thank Dr. Rock Mackie who listened to my concerns and helped me when I felt lost. He encouraged the idea of obtaining the adjoint data from the forward data.

Michael who shared the office space with me for three years is the one of those who have contributed the most. He frequently shared ideas about adjoint and optimization with me, and has been an excellent co-worker in many ways. I am sorry that I could not list everything for which I am grateful.

Other individuals contributed to this work. Dr. Chuan Wu taught me to understand GAMS code, and shared ideas about optimization. Dr. Warren D’Souza helped me to start DANTSYS code and GAMS code. Dr. Gustavo Olivera was an admirable post-doc who frequently checked my status and situation when he was around the university. I appreciated that Dr. Harry Keller was nearby. I could quickly go and ask him any questions. He has always been nice and encouraging. Dr. Robert Jeraj has been a good personal who helped me understand

optimization and transport. I would like to acknowledge Dr. Robert Meyer who corrected my understanding of the branch-and-bound method, Dr. Paul DeLuca and Dr. Steven Wright who reviewed my thesis and participated in my committee, Mr. Heath Odau who provided the clinical data for this study, and Dr. Tim Bohm who shared ideas about dosimetric issues and computer codes.

Finally, I thank my parents and my sister without whose love and prayers this work could have not been accomplished.

Abstract

Sua Yoo

Under the supervision of Professor Douglass L Henderson

At the University of Wisconsin – Madison

The adjoint approach commonly used in nuclear reactor applications is employed in radiation therapy treatment planning. For this work, we define the adjoint function for a region of interest (ROI) as the sensitivity of the average dose in the ROI to a source placement. We investigate an implementation of this adjoint function for optimization of brachytherapy treatment planning. The purpose of this study is to develop an efficient optimization algorithm.

This study specifically focuses on prostate permanent seed implants. The goal of an optimization process for prostate implants is to find a seed configuration that delivers a desired dose to the target while sparing the critical structures.

The adjoint functions are combined in one format, or combined into a single metric, which is the adjoint ratio. The adjoint ratio is the ratio of the adjoint functions of critical structures to the adjoint function of the target. This adjoint ratio as a function of source positions can provide a ranking of source positions based on their ability to achieve the optimization goal.

As an optimization tool, we propose the greedy heuristic, which makes a decision at each step and does not revise the decision in subsequent steps. The greedy heuristic constructs a seed configuration by selecting a source based on the adjoint ratio. Constraints are applied to support this seed selection procedure.

The results prove that the adjoint approach provides a framework for the development of an efficient optimization algorithm for radiation therapy treatment planning.

Table of contents

• Acknowledgements	i
• Abstract	iii
• Table of contents	iv
• List of figures	vi
• List of tables	ix
Chapter 1 Introduction	1
1.1 Prostate permanent seed implants	1
1.2 Treatment planning	4
1.3 Optimization process	5
1.4 Thesis objectives	7
Chapter 2 Background information	10
2.1 Optimization methods for prostate implant treatment planning	10
2.1.1 Simulated annealing	11
2.1.2 Genetic algorithms	13
2.1.3 Branch-and-bound methods	14
2.1.4 Observation	19
2.2 Transport	20
2.2.1 Forward transport and dose computation	20
2.2.2 Adjoint transport and dose computation	23
Chapter 3 Adjoint ratio	28
3.1 Adjoint data acquisition	29
3.1.1 DANTSYS: Diffusion Accelerated Neutral particle Transport System code	30
3.1.2 Transposing dose matrix	37
3.1.3 Task Group No. 43 dose calculation	39
3.2 Adjoint function of a region-of-interest	41
3.3 Adjoint ratio	47
3.4 Discussion	49
Chapter 4 Greedy heuristic for a seed-configuration	51
4.1 Introduction	51
4.2 Method and materials	52
4.2.1 Greedy heuristic	52
4.2.2 Isodose surface constraint	59
4.2.3 Termination criterion	63
4.2.4 Branch-and-bound for a basic mixed-integer programming model	64
4.2.5 Optimization environments	66
4.3 Results and discussion	67
4.4 Conclusion	77

Chapter 5 Greedy heuristic for seed- and needle- configuration	79
5.1 Introduction	79
5.2 Method and materials	82
5.2.1 Greedy heuristic	82
5.2.2 Selection of constraints	87
5.2.3 Branch-and-bound including a hard constraint for the number of needles	91
5.3 Results and discussion	92
5.4 Conclusion	102
Chapter 6 Greedy heuristic with an automatic selection of the constraint values	105
6.1 Introduction	105
6.2 Method and materials	106
6.2.1 Greedy heuristic	106
6.2.2 Selection of ranges for constraint values	109
6.2.3 Branch-and-bound including a constraint for the number of needles in the objective function	113
6.3 Results and discussion	115
6.4 Conclusion	132
Chapter 7 Conclusions and Future work	135
7.1 Conclusions	135
7.2 Future work	138
Reference	141
Appendix A Isodose curves for Chapter 6 patient results	148

List of figures

Figure 1.1	Patient positioning in the transrectal ultrasound-guided prostate implant.	3
Figure 2.1	Diagram of an instance of branch-and-bound tree [44, 45, 69].	16
Figure 2.2	Diagram of forward transport. (a) Brachytherapy case: A source is inside of the detector field, which consists of detector voxels. (b) External beam therapy case: A source is placed at the LINAC gantry and the detector voxels are in the patient (Courtesy of Micheal Kowalok). ‘S’ indicates a source.	22
Figure 2.3	Diagram of adjoint transport. (a) Brachytherapy case: A detector is placed at the patient geometry and sources are in the source field, which is equivalent to the detector field for brachytherapy case. (b) External beam therapy case: A detector is placed at the patient geometry and the sources are along the LINAC gantry (Courtesy of Micheal Kowalok). ‘D’ indicates a detector.	25
Figure 3.1	Flux-to-dose-rate conversion factor for photons in tissue vs. photon energy. ...	33
Figure 3.2	(a) Forward detector response distribution. The dose-rate scale is logarithmic [$\text{Gy}\cdot\text{hr}^{-1}$]. (b) Adjoint sensitivity distribution of the detector response. The scale is the logarithmic sensitivity of dose-rate per source-unit [$(\text{Gy}\cdot\text{hr}^{-1})/0.4\text{mCi}$]. Horizontal and vertical axes depict the x-y plane spacial extend in [mm].	36
Figure 3.3	Dose [Gy] in logarithmic scale along distance [mm] obtained by TG43 formalism (equation 3.14).	41
Figure 3.4	(a) One slice of prostate transrectal ultrasound image with the ROIs contoured. The ROIs are target ROI, urethra ROI, rectum ROI and margin ROI. The rest surrounding area is the normal tissue ROI. (b) Adjoint function of the target ROI in image-space. The adjoint function is in [Gy/S_u]. (c) Adjoint function of the margin ROI in image-space. (d) Adjoint function of the urethra ROI in image-space. (e) The adjoint function of the rectum ROI in image-space. (f) The adjoint function of the normal tissue ROI in image-space with the contoured ROIs on the image plane. Adjoint function is the sensitivity of the dose per source-unit [Gy/S_u] in the ROI from a source at an arbitrary seed position, where the source-unit, S_u , is $0.4\text{mCi} \ ^{125}\text{I}$ permanent seed.	43
Figure 3.5	Adjoint functions of ROIs at each seed position. The horizontal axis indicates seed positions and the vertical axis in the adjoint function as the dose per source-unit [Gy/S_u]. This value is the average dose deposited to each ROI by a $0.4\text{mCi} \ ^{125}\text{I}$ permanent seed as a function of seed position.	46
Figure 3.6	Adjoint ratio in image-space. The adjoint ratio is obtained using equation 3.17 with all weightings set to unity. The seed position that has the minimum adjoint ratio is marked ‘o’ in this image-space..	48

Figure 3.7	Adjoint ratio, $R(j)$, and ROI adjoint functions at each seed position. The horizontal axis indicates seed positions, the left vertical axis indicates the adjoint function as the dose per source-unit [Gy/S _u], and the right vertical axis indicates the unitless adjoint ratio.	49
Figure 4.1	Flowchart of the greedy heuristic.	58
Figure 4.2	Placement of firsts four sources in the greedy heuristic. See text.	59
Figure 4.3	Isodose surface constraint at each step – (a) 1 st , (b) 2 nd , (c) 3 rd , (d) 4 th , (e) 20 th and (f) 57 th step. 3-D prostate image; red is target (prostate), dark hole at the center is urethra, yellow is rectum and blue surface is the isodose surface. The search space X is inside of the red area but excludes the volume enclosed by the blue surface.	61
Figure 4.4	Isodose plots with the seed configurations of the greedy heuristic (left column) and the branch-and-bound method (right column). 200%, 150%, 100% (thicker line) and 90% of the prescribed dose isodose lines (solide lines) are shown with the ROIs (dotted lines). The seed placements are marked in ‘X’. The first two, middle two and last two slices are shown.	69
Figure 4.5	The dose-volume histogram (DVH) comparison between the greedy heuristic (solid line) and the branch-and-bound method (dashed line) for (a) target, (b) urethra, (c) rectum, and (d) normal surrounding tissue. The vertical dotted line in (a) indicates the prescribed dose 145Gy. 360Gy dose line is indicated for the urethra (b), and 90Gy for the rectum (c).	71
Figure 5.1	Flowchart of greedy heuristic for the optimization of a seed- and needle-configuration.	86
Figure 5.2	A plot of the number of needles used in 48 treatment plans versus the target volume. $y = 0.24x + 11.33$ (equation 5.2) is a fit function to the data. (Courtesy of Heath Odau in UWCCC).	90
Figure 5.3	Isodose plots with the seed configurations of the greedy heuristic (left column) and the branch-and-bound method (right column) for Case I ($C_{needle}=18$ and $U_{needle}= 18$). 200% (red), 150% (yellow), 100% (green) and 90% (blue) of the prescribed dose isodose lines are shown with the ROIs (dotted lines). The seed placements are marked in ‘X’. The first two, middle two, and last two slices are shown.	94
Figure 5.4	Dose-volume histogram (DVH) comparison between the greedy heuristic (GH) and the branch-and-bound method (GH) for Case I ($C_{needle}=18$ and $U_{needle}= 18$). The dotted horizontal line is the line for the prescribed dose, which is 145 Gy.	96
Figure 5.5	Dose-volume histogram (DVH) comparison between the greedy heuristic (GH) and the branch-and-bound method (GH) for Case II ($C_{needle}=20$ and $U_{needle}= 20$). The dotted horizontal line is the line for the prescribed dose, which is 145 Gy.	97

Figure 5.6 Dose-volume histogram (DVH) comparison between the greedy heuristic (GH) and the branch-and-bound method (GH) for Case III ($C_{needle}=22$ and $U_{needle}= 22$). The dotted horizontal line is the line for the prescribed dose, which is 145 Gy	98
Figure 6.1 Flowchart of greedy heuristic.	107
Figure 6.2 The predetermined needle configuration for patient J. The prostate images consist of 11 slices, which are projected on to one plane. The target and urethra are contoured and the needle positions are marked ‘n’.	114
Figure 6.3 A comparison of dose-volume histograms (DVH) between the greedy heuristic (GH) in solid lines and the branch-and-bound method (BB) in dashed lines. Figures (a) to (j) correspond to Patient A to J. Red lines are for the target DVHs, green lines for the urethra DVHs, yellow lines for the rectum DVHs and blue lines for the normal surrounding tissue.	117
Figure 6.4 V100 (target coverage) comparison between the greedy heuristic (red) and the branch-and-bound method (blue).....	123
Figure 6.5 V150 (high dose region) comparison between the greedy heuristic (red) and the branch-and-bound method (blue)	124
Figure 6.6 DNR (dose non-uniformity ratio) comparison between the greedy heuristic (red) and the branch-and-bound method (blue).....	125
Figure 6.7 CN (Conformation number) comparison between the greedy heuristic (red) and the branch-and-bound method (blue).....	126
Figure 6.8 Comparison of percentage urethral volume greater than or equal to $U_{urethra}$ between the greedy heuristic (red) and the branch-and-bound method (blue).....	127
Figure 6.9 Comparison of R90 between the greedy heuristic (red) and the branch-and-bound method (blue).....	128
Figure 6.10 Comparison of percentage rectal volume greater than or equal to U_{rectum} between the greedy heuristic (red) and the branch-and-bound method (blue)	128
Figure 6.11 Comparison of the number of seeds used in the greedy heuristic (red) and the branch-and-bound method (blue).....	129
Figure 6.12 Comparison of the number of needles used in the greedy heuristic (red) and the branch-and-bound method (blue).....	130
Figure 6.13 Comparison of the computational time spent by the greedy heuristic (red) and the branch-and-bound method (blue)	131

List of tables

Table 3.1	Forward and adjoint sources for the discrete energy groups.	35
Table 3.2	The anisotropy factors of ^{125}I model 6711.	40
Table 4.1	Definition of parameters in the pseudo-code 4.2.	57
Table 4.2	Constraints and weightings for the basic model.	66
Table 4.3	Comparison of the greedy heuristic and the branch-and-bound method with the evaluation parameters.	73
Table 5.1	Definition of parameters in the pseudo-code 5.1.	85
Table 5.2	Constraint values.	92
Table 5.3	Comparison of the greedy heuristic (GH) and the branch-and-bound (BB) method with the evaluation parameters.	100
Table 6.1	Ranges for the constraint values.	112
Table 6.2	Automatically selected constraint values, which produce a seed configuration successfully in the greedy heuristic for 10 patients.	116
Table 6.3	Comparison of the greedy heuristic (GH) and the branch-and-bound (BB) method with the evaluation parameters for patients A to J.	121

Chapter 1

Introduction

Brachytherapy (brachy- means close in Greek) is a radiation therapy, which is given by placing radioactive source materials directly into the cancerous tissues or close to it. The purpose of this study is to verify the usefulness of the adjoint concept from the theory of radiation transport and the information it provides for brachytherapy treatment planning optimization. This chapter focuses on introduction of the subject and motivation of our study.

1.1. Prostate permanent seed implants

Prostate cancer is the most common form of male cancer and the second leading cause of male cancer deaths in the United States [9]. Common treatment options are radical prostatectomy, radiation therapy, chemotherapy, hormonal therapy, and several other methods. Prostate permanent seed implants have become a major treatment option for early stage prostate cancer [33]. Prostate permanent seed implants, called prostate implants, are a type of internal radiation

therapy given by placing radioactive sources directly into the cancerous tissue. The radioactive sources are called seeds, and they deliver high dose to the target with minimal side effects. Prostate implants are performed under imaging and template guidance for precise placement of sources [5].

Prostate implants have a few advantages over external beam treatment. More precise localization is possible for prostate implants with the transrectal-ultrasound imaging technique. Higher dose can be administered to the target volume while sparing the rectum and bladder, due to the rapid dose fall-off of the sources. Unlike fractionated external beam treatments, only a one-time procedure is required. Prostate implants also show advantages over prostatectomy. It is minimally invasive, requiring short procedure time and a short recovery time. It has been reported that prostate implant cure rate surpasses that of radical prostatectomy and competes favorably with external beam treatment [2, 54, 82, 83]. It is also reported that the risk of side effects and complications after prostate implants are competitively low compared to the prostatectomy or external beam treatment [26, 54].

Historically, free-hand placement of sources was performed in an open surgical procedure [71]. Later on, the transrectal ultrasound (TRUS) guided prostate implant technique was introduced by Holm *et al.* [28]. Since Blasko *et al.* refined this procedure in the following years [5, 6], prostate implants have become popular. The American Associate of Physicists in Medicine Task Group No. 56 (TG56) and Task Group No. 64 (TG64) describe a brachytherapy procedure in a step-by-step guide [49, 81]. We can simplify this procedure in a three-step process: volume study followed by treatment planning; actual seed implantation; and post-implant evaluation. For the volume study, the patient lies in a supine position with his legs raised, as shown in Figure 1.1. A TRUS probe is inserted through the rectum and takes a series of cross-sectional images of the

prostate and surrounding area. The series of ultrasound images are examined to map regions-of-interest (ROIs), such as the target (prostate), margin, urethra, rectum, and surrounding normal tissue. ROI information is entered into a treatment planning process, which determines a seed configuration. The seed configuration is the design of seed positions where sources will be implanted. A couple of weeks after the volume study, seeds are loaded in needles according to the treatment plan, and the needles are inserted through the template with ultrasound guidance. A few weeks after the treatment, the treatment is evaluated based on CT images, which is called the post-implant procedure.

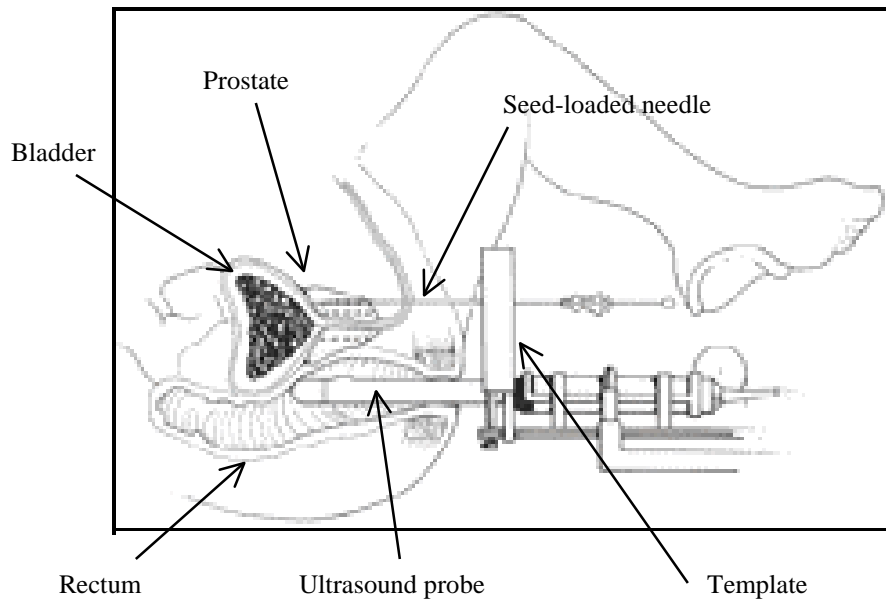


Figure 1.1 Patient positioning in the transrectal ultrasound-guided prostate implant

1.2. Treatment planning

One of the important aspects of a successful treatment is the dosimetric treatment planning stage. The goal of dosimetric treatment planning is to determine a seed and needle configuration that achieves a desired dose distribution to the target, while sparing the critical structures. The planning procedure, in general, starts with the prostate images taken at 0.5 cm interval by TRUS. The images, with ROIs contoured, are analyzed. Given the prescribed dose and source strengths, the plan should determine the number of seeds, the number of needles, the seed configuration, and the needle configuration.

In the early history of the prostate implant before the introduction of TRUS, free hand insertion of needles was performed using an open surgical procedure via the retropubic approach [71]. A nomograph was developed to establish spacing rules for sources using this procedure [3]. This nomograph is based on the correlation between the number of seeds, the source strength, and the average target dimension. However, the nomograph does not take into consideration the critical structures and the irregular shape of the target.

The manual treatment planning system is currently practiced in many clinics. It is a ‘trial-and-error’ process that can be time consuming and labor intensive. With the prostate images entered into the system, a user determines a seed configuration manually and reviews the resulting dose distribution. The seed configurations are modified repeatedly until a satisfactory dose distribution is achieved. In general there are about 300 to 500 possible seed positions available within the target, and the number of seeds implanted ranges from 50 to 100. Therefore, there are approximately $10^{60} - 10^{100}$ possible seed configurations. Since configurations are evaluated

manually, in practice, only a limited number of configurations can be investigated in a short time period.

1.3. Optimization process

The limitation of the manual system motivated the development of an automated treatment planning system, called optimization or inverse planning. An optimization process is a search strategy that is utilized to explore a large number of possible seed configurations automatically within a short time. With the given patient geometry and the desired dose distribution, source positions, also called seed positions, are searched until an optimal seed configuration is reached. Several optimization methods have been explored for the prostate implant problem, a few of which include simulated annealing (SA) [52, 55], genetic algorithms (GA) [22, 38, 79], and branch-and-bound (BB) methods [19, 38].

The strategies employed by these optimization methods can be loosely generalized as a three-step iterative procedure. The first step involves the consideration of a seed configuration. The current seed configuration under consideration is modified from the previous iteration. All optimization methods have different strategies to modify a seed configuration from the previous iteration. In the second step, the dose distribution is computed for this current seed configuration. Some other parameters such as the number of seeds, the number of needles, and the biological effectiveness are computed in this step as well. In the third step, the objective function, that represents a mathematical goal of the treatment planning, is analyzed. A solution at the current iteration is determined to be feasible if all constraints are met. If the solution is feasible, and if the resulting objective function value is improved from the last iteration or within a permitted range,

the seed configuration is updated. Then, the first step is repeated to search for an improved seed configuration. However, if the resulting objective function value is not an improvement or is beyond a permitted range, the current seed configuration is rejected (disregarded). The first step is repeated again with the previous seed configuration. The objective function primarily includes information of the dose delivered to the target and critical structures. The above mentioned other parameters can also be associated with the objective function.

The process of the first step depends on strategies employed by the optimization methods. A stochastic method such as simulated annealing and genetic algorithms relies on random-selection and probability functions. A deterministic method such as branch-and-bound utilizes a schematic search strategy. The process of the second step is the same for all optimization methods. All parameters are computed for a current solution. The process of the third step also depends on optimization strategies. Simulated annealing [52] and genetic algorithms [79] make a decision of acceptance or rejection with a probability function, which is related to the evaluation of the current solution. In the case of acceptance, the first step generates a new configuration modified from this accepted solution. In the case of rejection, the first step generates another configuration modified from the previous solution, which means the current iteration has achieved no solution. Branch-and-bound has different mechanism of accepting and rejecting. The detailed process of the branch-and-bound method will be discussed in Chapter 2.1.3.

For these optimization methods, in the first step, a seed position or configuration is considered based on a random process or computational scheme, which does not have a physical basis. There is no means to measure the physical significance of a seed position until the second step of dose computation and the third step of evaluation. Because of this lack of information

about seed positions, many trials that succeed in the first step are rejected in the third step, having accomplished nothing. This process takes unnecessary computational time.

The automated treatment planning can take several days if all possible seed configurations for a full three-dimensional (3-D) treatment plan were checked. The above-mentioned rejections in the third step consume computational time without achieving a result. Therefore, most optimization processes are terminated intentionally when a solution becomes feasible and acceptable, even though it may not be an optimal solution. In recent studies, in order to save computational time expense, time and data reduction strategies were adopted. The optimization method studied by Lee *et al.* [38] used a coarse computational resolution in the optimization process, and refined the resolution after the termination of the process. Poulit *et al.* [52] predetermined the needle configuration so that the optimization searched seed positions only along those restricted needle positions. Yu *et al.* [79] determined the seed-loading pattern in needles in advance, and then a needle configuration was optimized. Interactive two-dimensional (2-D) image slices were used in D’Souza *et al.*’s [18, 19] method. These studies using the time- and data-reduction strategies required about 10 to 30 minutes to arrive at a feasible and acceptable, though not optimal, solution.

1.4. Thesis objectives

There is in general about a two-week period for treatment planning between the volume study and the actual treatment procedure. However, the treatment-planning process should be accomplished in the shortest amount of time possible because of time and labor expenses. Moreover, it has been pointed out that preplanning has a downside mostly related to the mismatch between the prostate

images on the day of the seed insertion and those acquired in the volume study [21, 46]. Therefore, the need for treatment plan re-optimization or intra-operative planning is increasing. Computational time becomes more expensive for the re-optimization or intra-operative treatment planning than preplanning. Hence interest in the computational time for the optimization process is growing.

As pointed out in Chapter 1.3, current optimization strategies require many iterations to achieve an acceptable feasible solution because of numerous rejections and infeasible solutions. Our study is motivated by current optimization methods. As mentioned earlier, they have no means to measure the significance of seed positions until dose computation. This thesis reports on an efficient optimization algorithm for prostate implant treatment planning. The search strategy we study is based on a greedy heuristic and the adjoint concept adopted from radiation transport theory [4]. From radiation transport theory, we developed an adjoint function for each ROI, which is defined as the average dose deposited in the ROI by a unit-strength seed placed at any seed position. In this approach, the adjoint function relates the sensitivity of the average dose deposited in the ROI to changes in seed position. Therefore, the adjoint function provides a physical significance to each seed position and enables ranking of seed position for treatment planning. This adjoint concept is implemented in a greedy heuristic. A greedy heuristic is a simple-minded algorithm, which is known to be very fast. A complete seed configuration can be generated efficiently, which exploits the physical significance available from the adjoint functions of the ROIs.

The adjoint function of an ROI is obtained from the adjoint transport, which is the opposite of the forward transport. Chapter 2 provides background information on (1) current optimization methods for prostate implants treatment planning, and (2) forward and adjoint

transport and dose computational methods. The motivation of our study will grow to be clearer with an understanding of other optimization processes. The second major section of Chapter 2 will help the understanding of the adjoint ratio, which is used as a greedy criterion. Chapter 3 discusses the significance of the adjoint function of an ROI and the adjoint ratio, which combines the adjoint functions of all ROIs. It also includes methodologies for adjoint data acquisition.

Chapter 4 focuses on the use of the adjoint ratio in the greedy heuristic using a simple case study. The simple case considers optimization of a seed configuration without taking into account the number of needles. This chapter also illustrates how the isodose surface constraint restricts the search space. The greedy heuristic result is compared to the one arrived at by the branch-and-bound method.

Chapter 5 discusses the methodology developed for inclusion of a needle constraint to limit the number of needles in the greedy heuristic. Since this needle insertion process demands high precision and carries the risk of infection, it is desirable to use the lowest number of needles possible. Two types of isodose surface constraints are applied to determine the search space at two different points in the process; one is applied partway through, before the desired number of needles have all been used, and the other is applied after all of the desired number of needles have been used. The branch-and-bound method, against which the greedy heuristic is compared, uses a hard constraint in which the maximum number of needles is designated ahead of time.

Chapter 6 focuses on the automation methodology for the selection of constraint values in the greedy heuristic. The system tests out all possible combinations of constraint values within a given set of ranges for constraint values. For a comparison, the branch-and-bound method adds a parameter in the objective function to minimize the number of needles. Chapter 7 provides a summary and conclusion for this study, and suggests future work.

Chapter 2

Background information

2.1. Optimization methods for prostate implant treatment planning

One of the important aspects of a successful treatment is the planning stage in radiation therapy. The goal of treatment planning in prostate implants is to determine a seed and needle configuration that achieves a desired dose distribution to the target, while sparing the critical structures. This prostate implant problem can be expressed as a mixed-integer programming model. A mixed-integer programming makes use of both integer and real variables. The decision variable in this problem is the placement or non-placement of a source at a seed position, which is defined by the template grid. An integer (binary) variable, 1 or 0, denotes seed placement or non-placement, and a real variable can represent dose to each tissue position.

This chapter will discuss optimization methods that solve the prostate implant problem as a mixed-integer programming model. An optimization process can search a large number of possible seed configurations automatically in a short time. Several optimization methods have

been explored for the prostate implant problem, a few of which include simulated annealing (SA) [52, 55], genetic algorithms (GA) [22, 38, 79], and branch-and-bound (BB) methods [19, 38]. Simulated annealing and genetic algorithms are stochastic methods, whose decisions rely on random selection and probability functions. Branch-and-bound is a deterministic method, which searches feasible solutions with a schematic strategy. The following sub-sections introduce methodologies of these three methods.

2.1.1. Simulated annealing

Simulated annealing (SA) is a stochastic approach for minimizing a cost function, called an objective function. The term ‘simulated annealing’ simulates a process of cooling a system to its ground state, or its minimum potential energy stage. Provided that cooling is sufficiently slow, the simulated annealing process lowers the temperature until the system becomes a frozen state, with minimum temperature. The cost function then reaches the global minimum. If cooling is insufficiently slow, the system is quenched, resulting in some atoms frozen in high-energy states. This status corresponds to an objective function trapped in a local minimum.

The original scheme is that the initial state of a system is chosen at energy, $E(T_o)$, at the initial temperature, T_o . Holding T constant, the system configuration is modified randomly. The change in energy, ΔE , is computed for the modified configuration. If ΔE is negative, the new configuration is accepted and replaces the previous configuration. If ΔE is positive, it is accepted with a probability given by a function $P(\Delta E) = \exp(-\Delta E/T)$; a small positive change is more likely to be accepted at a high temperature than a large positive change at a low temperature. This process is performed iteratively until the change ΔE becomes sufficiently small. As the number of

iteration increases, the temperature decreases. This algorithm was first introduced by Kirkpatrick *et al.* [32] and has been adopted for external beam treatment [70], vagina brachytherapy [63], and prostate implants [52].

The simulated annealing procedure adopted for prostate implants by Pouliot *et al.* [52] requires a predetermined needle configuration and an initial number of seeds. It starts with a random seed configuration restricted to the predetermined needle configuration. Moving at least one seed to another location makes a transition toward the next iteration. Each time a transition is made, the cost function, E , is computed based on the updated dose distribution. Depending on the ΔE value, the current configuration is accepted or rejected. As the number of iteration increases, the temperature, T , decreases and consequently the probability of acceptance becomes lower and lower. Typically, simulated annealing begins lowering the temperature after a large number of iterations. However, Pouliot *et al.* proposed fast-simulated annealing, which reduces the temperature per iteration starting at the beginning of the process. The process repeats until a termination criterion is achieved [52].

It is reported that fast-simulated annealing reaches an adequate solution in approximately 15 minutes and 20,000 iterations [52]. It was reported that this calculation was performed on a work station but no specific configuration details were given. The achieved solution shows that fast-simulated annealing is an efficient tool for prostate implant treatment planning optimization. However, there are a few drawbacks: (1) the needle configuration is predetermined manually, (2) the maximum number of seeds is set in advance, and (3) the process is terminated after a certain number of iterations.

2.1.2. Genetic algorithms

Genetic algorithms, as suggested by their name, are based on natural evolution. Genetic algorithms were developed as an imitation of an ever-changing population of chromosomes. A chromosome consists of genes and tends to adapt itself to its environment. The evolution to the next generation of chromosomes is carried out through reproduction that undergoes crossover and mutation. Parents are selected for reproduction in a stochastic manner that assigns a higher probability for mating to “fitter” parents. Crossover exchanges genes between a selected pair of parent chromosomes with a specified probability. The consequent offspring thereby carry combined genetic information from different parents. Mutation occurs randomly to each gene in a chromosome with some probability. Therefore, the next generations are similar to their parents, but represent blends of parental features. The survival probability is measured by the “fitness” of the chromosome. The fitness function represents the objective function.

Genetic algorithms were first introduced by Holland [28] in 1975. They have been adopted to beam weight optimization for external beam therapy [36] and stereotactic radiosurgery [80]. After Yu *et al.* [79] applied the genetic algorithm to prostate implant treatment planning optimization, it became a common optimization tool for prostate implants [38, 76].

The genetic algorithm implemented for prostate implants by Yu *et al.* [79] starts with a random population of strings, that is, a set of random seed configurations. The size of the population is a predetermined parameter. A string is a series of possible seed positions (elements) with either 0 or 1. The strings in the population are ranked according to a fitness function. The strings undergo evolution into the next generation involving three probability operations: replication, crossover and mutation. Replication of a string occurs with the probability expressed

as the fitness function. Because the fitness function includes terms for dose distribution and the number of needles, there is a greater tendency to replicate strings close to optimality. Crossover takes place at random locations on randomly paired strings with a predetermined probability. Mutation takes place at each element in a string with a predetermined probability as well.

The results of Yu *et al.*'s genetic algorithm are significantly better than manual plans [79]. The computational time is 30 minutes for the largest case on a SUN SPARCstation5 (no other information on the configuration was provided). This result demonstrates that the genetic algorithm applied to prostate implant optimization can achieve acceptable treatment plans in a short time. We cite a few shortcomings in this method: (1) seed-loading pattern along a needle is predetermined and a needle configuration is optimized, (2) probability values for selection, crossover and mutation are determined arbitrarily, and (3) the process is terminated when the objective function does not improve or after a certain number of iterations.

2.1.3. Branch-and-bound methods

Branch-and-bound is a deterministic method that has proven to be the most effective tool for general integer and mixed-integer programming [43]. Thus, it is commonly employed in commercial mixed-integer programming [45, 75]. The term “branch” hints at the partitioning process – a “divide-and-conquer” approach – used to prove optimality of a solution. The feasible set is “divided” (or “branched”) into several subsets, and an analysis is performed separately on each of the sets in order to “conquer” the entire original problem [43]. This partitioning process is limited (in order to prevent, if possible, an exhaustive search) by the process denoted by “bound”, which attempts to eliminate portions of the feasible set from further consideration by determining

that they cannot contain an optimal solution. Branch-and-bound can reach a global optimum because it takes into account all feasible sets. Nevertheless, its slow convergence and data storage requirement can be shortcomings. The reasons for this are that a very large number of branches and subsets may be created and that each subset that can contain an optimal solution should be stored for later consideration [66].

Branch-and-bound solves an optimization problem, first by relaxing the integer conditions to allow continuous real numbers. If the procedure encounters a minimizing problem, a relaxed optimum solution becomes a lower bound. The relaxed optimum solution is branched into subsets (nodes). If a subset results in an infeasible solution, no more branching is needed from that subset, and its upper bound is set to infinite. If processing a relaxed subset results in a feasible integer solution, its value becomes an upper bound, and the subset doesn't branch anymore. Adding the concept of an upper bound enhances the efficiency of computation by (hopefully) eliminating an exhaustive search. If a refined partition results in a relaxed optimum solution whose value is greater than the previous lower bound, a new lower bound is set. An active subset is closed and eliminated from further branching if its relaxed objective function value exceeds the upper bound [66], since it cannot contain an optimal solution. The sequence of lower bounds generated by relaxed subsets is monotonically non-decreasing, and the sequence of upper bounds is monotonically decreasing [43]. The process terminates in the event that the lower and upper bounds are equal. When this event occurs an optimal solution has been determined.

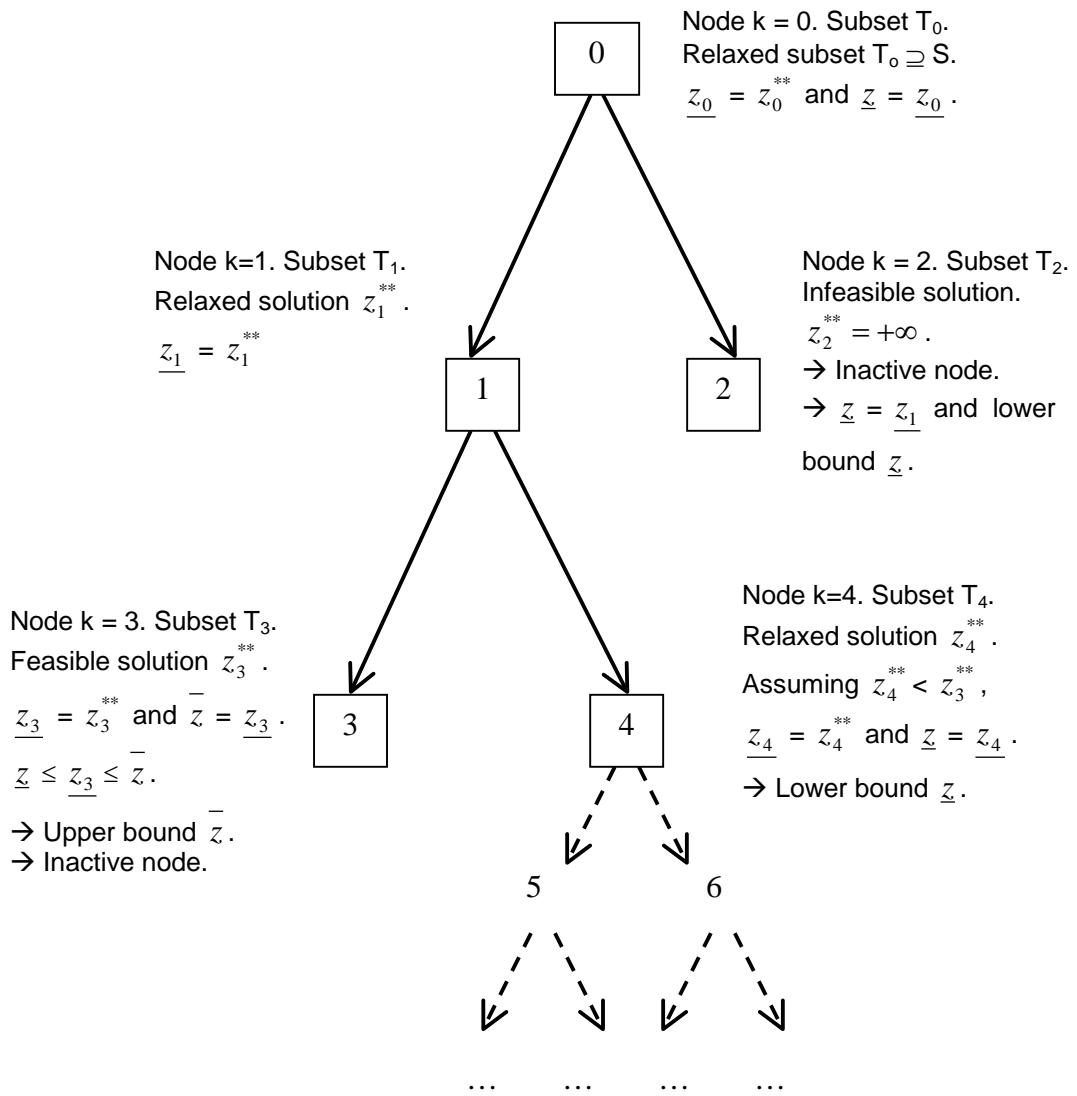
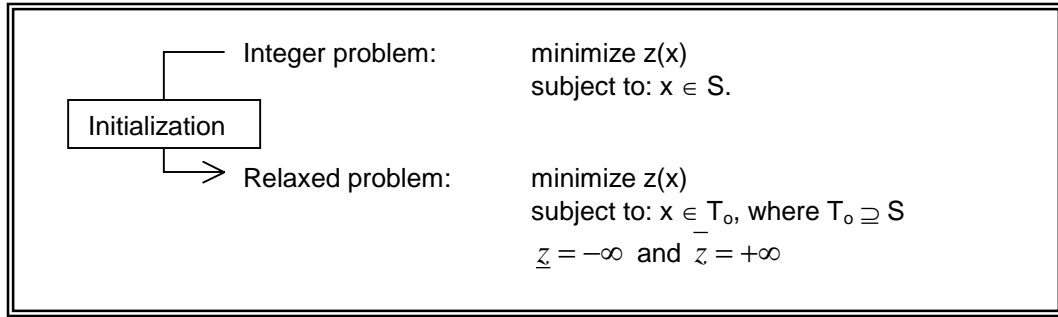


Figure 2.1 Diagram of an instance of branch-and-bound tree [44, 45, 69]

As an instance of branch-and-bound tree shown in figure 2.1, we consider the mixed integer problem whose objective function is *minimize* $z(x)$ where x is a set of integer variables (The exact manner of branching can be different for other cases of branch-and-bound trees) [44]. A general branch-and-bound algorithm initializes with a relaxed problem. The initial lower bound is $\underline{z} = -\infty$ and upper bound is $\bar{z} = +\infty$. As shown in figure 2.1 at node 0, a relaxed solution is computed for an active subset; $T_0 \supseteq S$, where S_k indicates a subset of the original feasible solution at a node k , T_k indicates a subset that contains a relaxed solution at a node k , and the initial node $k = 0$. The active node 0 is analyzed so as to obtain a relaxed optimal solution denoted as z_0^{**} . A lower bound for node 0, \underline{z}_0 , is set to z_0^{**} , and the incumbent lower bound \underline{z} is \underline{z}_0 . The subset T_0 is branched into subsets T_1 and T_2 .

Node 1 is analyzed and obtains a relaxed optimum, z_1^{**} . A lower bound for node 1, \underline{z}_1 , is set to z_1^{**} . Node 2 is analyzed and found to be infeasible. Thus, the optimal value at node 2 is set to $z_2^{**} = +\infty$. The subset T_2 becomes inactive; there will be no more branching from node 2. The lower bound is set to the lower of the optimal values of the two subsets at the same level (node 1 and node 2). Because node 2 has turned to be infeasible, the lower bound, \underline{z} , is set to \underline{z}_1 . \underline{z} is set to \underline{z}_1 only after the analyses of node 1 and node 2 have been made, because they are in the same level.

Going back to node 1, the subset T_1 is branched into subsets T_3 and T_4 . The subset T_3 is analyzed and contains a feasible optimal solution, z_3^{**} . A lower bound for node 3, \underline{z}_3 , is set to z_3^{**} . Node 4 is analyzed and contains a relaxed optimum, z_4^{**} . A lower bound for node 4, \underline{z}_4 , is set to z_4^{**} . Since node 3 contains a feasible solution but node 4 contains a relaxed optimum ($z_4^{**} <$

z_3^{**}), and since \underline{z}_3 is between \underline{z} and \bar{z} ; $\underline{z} \leq \underline{z}_3 \leq \bar{z}$, the incumbent upper bound \bar{z} is set to \underline{z}_3 .

The subset T_3 becomes an inactive set. \underline{z}_4 is greater than or equal to \underline{z} but lower than \bar{z} , thus, the incumbent lower bound \underline{z} is set to \underline{z}_4 . This subset T_4 branches into subset T_5 and T_6 . This process occurs recursively until a feasible optimal solution z^{**} becomes equal to \underline{z} and \bar{z} ; $\underline{z} = z^{**} = \bar{z}$. However, if the value at node 4 were worse than the one at node 3, in another words, if \underline{z}_4 were greater than \underline{z}_3 , then node 4 would be closed and the process is completed. Figure 1.2 explains the branch-and-bound tree in a diagram [43, 44, 66]. This explanation does not include all possible events in branch-and-bound method; yet, it shows the schematic flow of the process.

This branch-and-bound method for a mixed-integer programming model has been applied to prostate implant treatment planning [38, 18, 19]. Lee *et al.* [38] describe a basic model as minimizing total penalties or maximizing total awards. The penalties consist of ROI-weighted summation of dose deviated from soft constraints. The rewards, conversely, include ROI-weighted summation of dose achievement judged by the soft constraints. The number of seeds and the number of needles are not restricted in this model. Different combinations of weightings are tested. A genetic algorithm is also tested on the same model for comparison. Treatment plans from branch-and-bound method are those associated with the best feasible solutions found, which is not necessarily an optimal solution because of solution time limitations. The study concludes that branch-and-bound method yields a better solution with a better computational time, which is about 5 – 15 minutes.

The basic model set by D’Souza [18, 19] involves an objective function minimizing penalties with hard constraints for the urethra and rectum. The penalties consist of ROI-weighted summation of underdose and overdose with respect to soft constraints, the weighted number of

seeds, and the weighted number of needles. These weights are selected by trial-and-error, performed by a user until a satisfactory solution has been achieved. Maximum dose to the urethra and rectum is controlled by the hard constraints in the basic model. This study also investigates dose-volume constraints for urethra [19] and a dose homogeneity constraint for the target [20]. The plans from the branch-and-bound method are superior to the manual plans with respect to dose distribution and computational time. The time required to achieve a feasible solution, not an optimal solution, is about 20 – 40 minutes depending on the geometry. This work was performed on a Sun Ultra2 200 MHz CPU [19]. The model with dose-volume constraints requires an additional 5 – 10 minutes [20].

This branch-and-bound method for a basic mixed-integer programming model is used for comparison with the greedy heuristic method.

2.1.4. Observation

The studies in optimization for prostate implants tend to focus on developing an algorithm, which is supposed to find a seed configuration efficiently. The current algorithms are similar in the sense that they are iterative and many trials are rejected before a viable solution is reached. Simulated annealing and genetic algorithms reject solutions with a probability function, which represents an objective function. Branch-and-bound inactivates subsets that are infeasible or that yield bounds beyond a range. Feasibility is determined by constraints, and bounds are determined by an objective function.

The rejection process or the inactivating process appears to be inefficient. There is no means to estimate in advance, thereby, many trials are not accepted as a solution after they have

proven to be non-improving or infeasible. The purpose of our study is to verify the usefulness of the adjoint concept and its implementation in the optimization process to supplement this weak point of the current methods. The adjoint information will enable an estimation of which seed position is more favorable than others before an actual dose computation has been performed.

2.2. Transport

The Boltzmann transport equation describes the neutral particle transport phenomena. This chapter discusses the forward and adjoint transport methods, followed by the dose computational method, which uses the forward and adjoint flux distributions. Understanding of forward and adjoint transport is fundamental for the appreciation of the adjoint ratio, which plays an important role in our optimization strategy.

2.2.1. Forward transport and dose computation

The linear form of the time-independent Boltzmann transport equation describes the propagation of neutral particles through matter. This equation is expressed as [4, 39]

$$\begin{aligned} \hat{\Omega} \cdot \vec{\nabla} \Phi(\vec{r}, \hat{\Omega}, E) + \mu_t(\vec{r}, E) \Phi(\vec{r}, \hat{\Omega}, E) \\ = \int \int \mu_s(\vec{r}, \hat{\Omega}' \rightarrow \Omega, E' \rightarrow E) \Phi(\vec{r}, \hat{\Omega}', E') d\hat{\Omega}' dE' + Q(\vec{r}, \hat{\Omega}, E), \end{aligned} \quad (2.1)$$

where the phase space coordinates for a particle's position \vec{r} , direction $\hat{\Omega}$, and energy E are independent variables. The photon particle flux $\Phi(\vec{r}, \hat{\Omega}, E)$ describes the photon particles in a phase space element defined by the volume element $d\vec{r}$ about \vec{r} , the energy element dE about

E , and the direction of the particles within the solid angle element $d\hat{\Omega}$ about $\hat{\Omega}$. $Q(\vec{r}, \hat{\Omega}, E)$ is the distribution of source particles within the same phase space element. $\mu_i(\vec{r}, E)$ denotes the space and energy dependent total collision cross-section, and $\mu_s(\vec{r}, \hat{\Omega}' \rightarrow \Omega, E' \rightarrow E)$ is the double differential scattering cross-section, which represents the probability of scattering from an energy E' to an energy within the range dE about E , and from a direction $\hat{\Omega}'$ to a direction within the range $d\hat{\Omega}$ about $\hat{\Omega}$.

The first term on the left-hand side, $\hat{\Omega} \cdot \vec{\nabla} \Phi(\vec{r}, \hat{\Omega}, E)$, represents the change of the particles' angular density at the position \vec{r} due to streaming of the particles, i.e. motion of the particles in a straight outgoing line without any collisions. This term is referred to as the streaming term. The next term corresponds to the particles that undergo collisions in the system. The first term on the right-hand side represents the particles generated by scattering and the last term denotes the source particles introduced in the system. Therefore, this forward transport equation represents particle conservation in the system for it states that the particles leaving or disappearing from a unit volume are equivalent to the particles introduced or generated in a unit volume [4]:

$$\begin{aligned} \text{Net number of particles crossing unit area of the surface per unit time, which bounds a unit volume} &+ \text{Particles entering into collisions in the given volume} \\ &= \text{Particles that emerge from the collisions in the given volume} + \text{Introduction of the source particles in the given volume} \end{aligned}$$

In forward transport, particles start at a source location and are transported forward to a detector. Particles are down-scattered losing energy and deposit their energy to the medium through interaction. Solving the forward transport equation yields the forward flux distribution, Φ , throughout the system. Figure 2.2 illustrates forward transport in simple diagrams for the brachytherapy case (figure 2.2(a)) and the external beam case (figure 2.2(b)) [34]. A source is placed inside of the detector field in the brachytherapy case. The detector field consists of detectors, which represent patient tissue voxels. The forward flux distribution is obtained over all voxels in the detector field as shown in figure 2.2(a). In external beam radiation therapy, a source is placed at a position in the LINAC (linear accelerator) gantry that rotates around a patient. The detector field represents the exposed patient tissue voxels. This is illustrated in figure 2.2(b) [34].

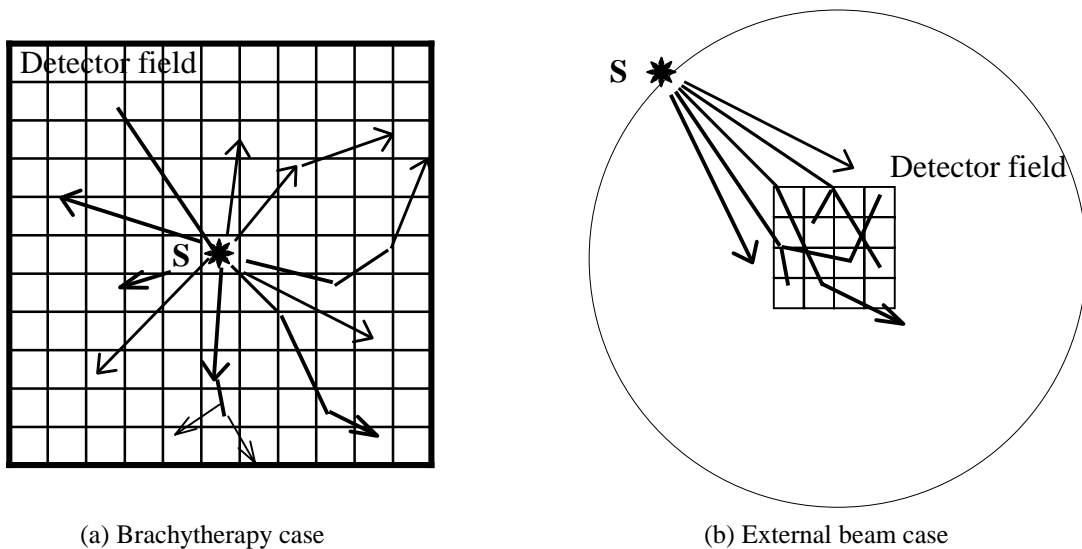


Figure 2.2 Diagram of forward transport. (a) Brachytherapy case: A source is inside of the detector field, which consists of detector voxels. (b) External beam therapy case: A source is placed at the LINAC gantry and the detector voxels are in the patient (Courtesy of Micheal Kowalok). ‘S’ indicates a source.

The detector response can be computed by using the forward flux. The primary quantity of our interest is the dose deposited in the detector, which is the detector response. The detector response, D , is the dose deposited at an arbitrary location \vec{r}_{det} , with volume V_{det} , and a response function μ_{det} . D may be calculated by taking the inner product of the forward flux and the detector response function μ_{det} over space, direction and energy [4, 39]:

$$D = \langle \Phi \cdot \mu_{det} \rangle = \iiint \Phi(\vec{r}_{det}, \hat{\Omega}, E) \mu_{det}(\vec{r}_{det}, \hat{\Omega}, E) dV d\hat{\Omega} dE \quad (2.2)$$

where $\langle \rangle$ signifying integration over all independent variables and

$$\mu_{det}(\vec{r}_{det}, \hat{\Omega}, E) = C \cdot E \cdot \mu_{en} / \rho(\vec{r}_{det}, \hat{\Omega}, E), \quad (2.3)$$

where μ_{en}/ρ is the mass-energy absorption coefficient, and C is a unit-conversion constant.

We define a transport operator L to rewrite the forward equation 2.1 in operator notation as

$$L\Phi = Q, \quad (2.4)$$

where

$$\begin{aligned} L\Phi(\vec{r}, \hat{\Omega}, E) &= \hat{\Omega} \cdot \vec{\nabla} \Phi(\vec{r}, \hat{\Omega}, E) \\ &+ \mu_t(\vec{r}, E) \Phi(\vec{r}, \hat{\Omega}, E) \\ &- \iint \mu_s(\vec{r}, \hat{\Omega}' \rightarrow \Omega, E' \rightarrow E) \Phi(\vec{r}, \hat{\Omega}', E') d\hat{\Omega}' dE'. \end{aligned} \quad (2.5)$$

2.2.2. Adjoint transport and dose computation

The adjoint operator L^+ is defined by the following identity [4].

$$\langle \Phi^+, L\Phi \rangle = \langle \Phi, L^+\Phi^+ \rangle \quad (2.6)$$

where Φ^+ is referred to as the adjoint flux. The two functions Φ and Φ^+ satisfy the appropriate boundary and continuity conditions for the forward flux and adjoint flux, respectively. The forward flux satisfies the boundary condition that $\Phi(\vec{r}, \hat{\Omega}, E) = 0$ for all positions on the convex boundary and for all incoming particle directions, $\hat{n} \cdot \hat{\Omega} < 0$, where \hat{n} is the surface normal vector.

Then the adjoint flux satisfies the boundary condition that $\Phi^+(\vec{r}, \hat{\Omega}, E) = 0$ for all positions on the convex boundary and all outgoing adjoint particle directions, $\hat{n} \cdot \hat{\Omega} > 0$. Moreover, it is assumed that the forward and adjoint fluxes are continuous functions in space. As is defined the forward operator L , and the adjoint operator L^+ can be defined as

$$L^+ \Phi^+ = Q^+ \quad (2.7)$$

where

$$\begin{aligned} L^+ \Phi^+ (\vec{r}, \hat{\Omega}, E) &= -\hat{\Omega} \cdot \vec{\nabla} \Phi^+ (\vec{r}, \hat{\Omega}, E) \\ &\quad + \mu_t(\vec{r}, E) \Phi^+ (\vec{r}, \hat{\Omega}, E) \\ &\quad - \iint \mu_s(\vec{r}, \hat{\Omega}' \leftarrow \Omega, E' \leftarrow E) \Phi^+ (\vec{r}, \hat{\Omega}', E') d\hat{\Omega}' dE', \end{aligned} \quad (2.8)$$

where Q^+ is defined as the adjoint source. The linear form of the time-independent adjoint transport equation can be expressed as

$$\begin{aligned} &- \hat{\Omega} \cdot \vec{\nabla} \Phi^+ (\vec{r}, \hat{\Omega}, E) + \mu_t(\vec{r}, E) \Phi^+ (\vec{r}, \hat{\Omega}, E) \\ &= \iint \mu_s(\vec{r}, \hat{\Omega}' \leftarrow \Omega, E' \leftarrow E) \Phi^+ (\vec{r}, \hat{\Omega}', E') d\hat{\Omega}' dE' + Q^+ (\vec{r}, \hat{\Omega}, E) \end{aligned} \quad (2.9)$$

The differences noted between the equations 2.5 and 2.8 or between the equations 2.1 and 2.9 are (1) the adjoint equation has a minus sign for the streaming term, which signifies a reversal of the directional transfer, and (2) the scattering term has reversed change in angle and energy

notation. These differences illustrate the adjoint equation represents a reversed transport in energy and angle. The adjoint particles are transported backward because they begin at the detector location and gain energy through up scattering as they are transported backward in time toward source locations.

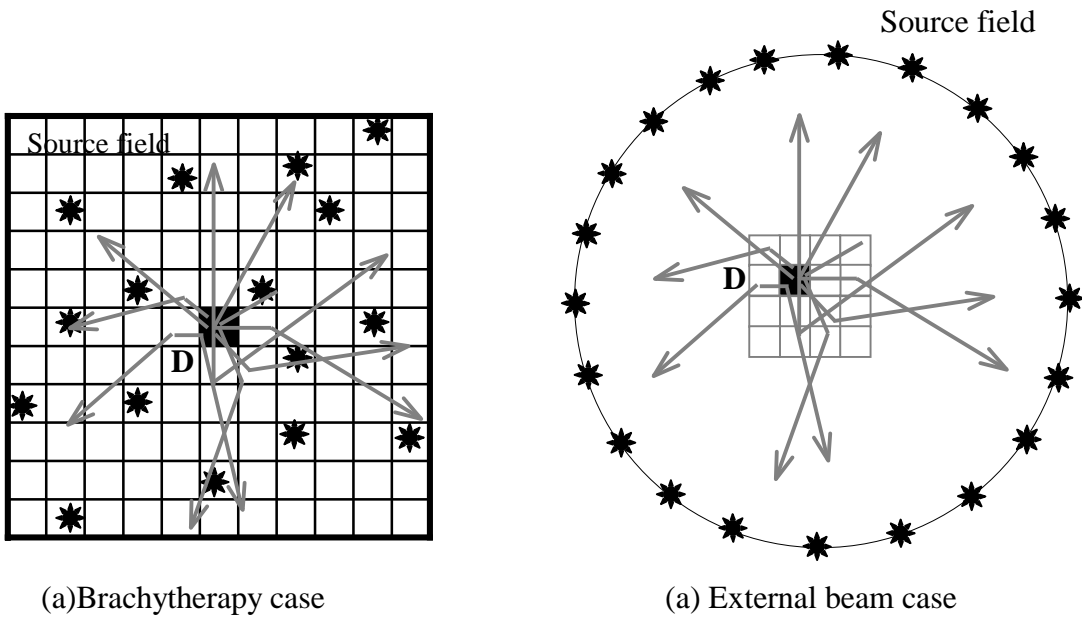


Figure 2.3 Diagram of adjoint transport. (a) Brachytherapy case: A detector is placed at the patient geometry and sources are in the source field, which is equivalent to the detector field for brachytherapy case. (b) External beam therapy case: A detector is placed at the patient geometry and the sources are along the LINAC gantry (Courtesy of Micheal Kowalok). ‘D’ indicates a detector.

In adjoint transport, an adjoint source, which is a detector response function, starts at a detector location and moves backward to a source field interacting within a medium. The adjoint particles up-scatters gaining energy through interaction in the medium. Solving the adjoint transport equation yields the adjoint flux distribution, Φ^+ , throughout the system. Figure 2.3 illustrates adjoint transport in simple diagrams for brachytherapy case (figure 2.3(a)) and external beam case (figure 2.3(b)) [34]. For a detector inside of a patient geometry, the adjoint flux

distribution is obtained over all voxels in the source field, which is in the patient geometry (figure 2.3(a)). A detector is inside the patient and the source field is in the LINAC gantry for the external beam case as shown in figure 2.3(b) [34]. Thus, the adjoint flux distribution is obtained for the source field along the gantry.

Replacing $L\Phi$ with Q (relation equation 2.4) and $L^+\Phi^+$ with Q^+ (relation equation 2.7), the equation 2.6 can be rewritten as

$$\langle \Phi^+ \cdot Q \rangle = \langle \Phi \cdot Q^+ \rangle, \quad (2.10)$$

which can be compared to the equation 2.2. Equation 2.10 defines the detector response function, μ_{det} , as the adjoint source on the right-hand side,

$$\mu_{det}(\vec{r}_{det}, \hat{Q}, E) = Q^+(\vec{r}_{det}, \hat{Q}, E). \quad (2.11)$$

The position, angle, and energy variables of this adjoint source are determined by a detector response function. The equation 2.10 is re-expressed using the detector response function μ_{det} , as

$$\langle \Phi^+ \cdot Q \rangle = \langle \Phi \cdot \mu_{det} \rangle. \quad (2.12)$$

Therefore, the detector response can be obtained by using the adjoint method

$$D^+ = \langle \Phi^+ \cdot Q \rangle, \quad (2.13)$$

where the ‘+’ distinguishes it from the detector response obtained by the forward method.

In summary, forward analysis starts with the source particles at a given source position. The forward method transports source particles forward, and they down-scatter through the medium, yielding the response of a detector placed at an arbitrary location. Conversely, the adjoint analysis starts with the adjoint source, which is the detector response function, at a given detector location. The adjoint method transports the adjoint source backward; it up-scatters, yielding the response of that detector due to a source placed at an arbitrary position. In other words, the adjoint analysis for a detector gives the sensitivity distribution of the detector’s

response to sources at arbitrary positions. This information is the detector's so-called "adjoint function" and has been used for perturbation and optimization studies in areas such as reactor system [62], radiation shielding [67], satellite design [31], and radiation therapy treatment planning [17, 29, 35, 25]. This quantity is also known as an "importance function" because it shows the importance of each source placement to the magnitude of a detector's response [4].

The dosimetric technique for radiation therapy depends on the forward method only. Dosimetric information can be obtained with a known source position. Thus, an optimization process doesn't estimate which source position is favorable until it performs a dosimetric evaluation. However, the adjoint method provides dosimetric information with a known detector position for unknown source positions. Therefore, the adjoint analysis provides an estimate of which position is favorable for an optimization goal without dosimetric evaluation.

Chapter 3

Adjoint ratio

This chapter introduces methods to acquire forward and adjoint datasets. We used the discrete ordinate computer code system (DANTSYS) [12] to demonstrate the forward and adjoint dose computation. The relationship between the doses computed through the forward approach and the adjoint approach was analyzed. We found that the transpose of the forward dose matrix was equivalent to the adjoint dose matrix. After analysis of the relationship between forward and adjoint dose data, we learned that the adjoint dataset could be obtained by operating on the forward dataset. The American Associate Physicists in Medicine (AAPM) Task Group 43 (TG43) [48] dose formalism was used in this study. This chapter discusses these methods to obtain complete datasets as preparation for optimization.

In the previous chapter, it was discussed that the adjoint analysis provides an estimate of which source position is favorable for an optimization goal without dosimetric evaluation. If we were interested in one detector but many possible source positions, the adjoint information would be advantageous. Oppositely, if our interest were in many detectors but one determined source

position, the forward information would be advantageous. However, the radiation therapy problem consists of many detector voxels in the patient geometry and many source positions (voxels) in the template grid for prostate implants or in the gantry for the external beam therapy. In addition, treatment-planning process requires a complete dataset for all possible source positions and for all interested detector voxels in the patient.

In order to take advantage of the adjoint information, each ROI that consists of many detector voxels is considered as one large detector. In this manner, the adjoint information provides average dose to the whole ROI due to placement of a source at an arbitrary position. Now with this whole ROI adjoint information, one is able to estimate which source position is highly effective to the target ROI, and which source position is minimally damaging to the critical structures' ROIs. This chapter discusses the whole ROI adjoint information and introduces the adjoint ratio, which includes adjoint information of all ROIs and enables the ranking of source positions.

3.1. Adjoint data acquisition

The particle transport can be simulated statistically by using the Monte Carlo method, or deterministically by using the Discrete Ordinates Method (DOM) [10, 39]. The Monte Carlo method simulates particle transport numerically based on random selection, and makes use of probability distribution functions. The particle interaction cross-section is interpreted as a probability function. The direction, energy, and location of collisions are determined based on the possibilities sampled by computer generated random numbers. The DOM approaches the transport problem with a set of discretized energy, direction and space variables. The energy,

angular and spatial integrals are approximated by sums over the discrete energy, direction and space. The angular derivatives are approximated by differences in the discrete angles. This section discusses the procedure to generate the dose deposition kernel by the forward and adjoint approaches. The dose deposition kernel will be used in the following optimization study.

3.1.1. DANTSYS: Diffusion Accelerated Neutral particle Transport System code

The Diffusion Accelerated Neutral particle Transport System code (DANTSYS) solves the neutral particle transport equation in the discrete ordinate approach. The Discrete Ordinates Method is a deterministic method to solve the Boltzmann transport equation [39]. The DOM approach subdivides the continuous energy, angle, and spatial variables into discrete bins [37]. The resulting flux quantity is averaged over the discrete bins. The computational time depends mostly on the following four factors: 1) the number of discretized angles, which is known as S_N , 2) the number of discretized energy bins for the cross-section library, 3) the discretized space that determines the geometry resolution, and 4) the order of Legendre polynomials, P_L , also known as the spherical harmonic method, by which the particle fluxes are smoothly represented. The DANTSYS code has been employed for brachytherapy dosimetry study [13, 14, 15]. The studies have concluded that the DOM is capable of achieving accuracy equivalent to Monte Carlo , and that reduction in the number of energy groups provides significant gains in efficiency without affecting accuracy.

In the preliminary study, we simulated a two-dimensional tissue material slab in x-y geometry [77]. The DANTSYS code obtained forward and adjoint fluxes by solving the forward

and adjoint transport equations, respectively. The detector response distribution, which is the dose distribution, was computed with the forward flux distribution, and the sensitivity distribution, which is the sensitivity of dose, is computed with the adjoint flux distribution. The dose computation method for discretized energy, angle, and space is explained in the following paragraphs.

Combining the equation 2.2 and 2.3, the dose-rate to a voxel i from an isotropic source at a voxel j can be expressed as

$$\dot{D}_{ij} = C \cdot \iint \Phi_{ij}(\vec{r}_i, E) E \mu_{en}(\vec{r}_i, E) / \rho(\vec{r}_i) dV dE \quad (3.1)$$

where \dot{D}_{ij} is the dose-rate to the voxel i from a source at j in the unit of $\text{Gy}\cdot\text{hr}^{-1}$, and C is a unit conversion constant. Because the brachytherapy source decays, the detector response represents not dose but dose-rate, and the dose-rate refers the initial dose-rate. $\Phi_{ij}(\vec{r}_i, E)$ is the forward scalar flux (angle-integrated flux) obtained from transporting particles at j . The forward flux has the unit of $\text{particles}\cdot\text{cm}^{-2}\cdot\text{sec}^{-1}$ and the source has the unit of $\text{particles}\cdot\text{cm}^{-3}\cdot\text{sec}^{-1}$. $\mu_{en}(\vec{r}_i, E)$ is the energy absorption coefficient of the detector i as a function of energy in the unit of cm^{-1} . $\rho(\vec{r}_i)$ is the spatial density distribution in the detector voxel in the unit of $\text{kg}\cdot\text{cm}^{-3}$. The discrete ordinate method solves the transport equation by averaging over the discretized space. Therefore, $\Phi_{ij}(\vec{r}_i, E)$, $\mu_{en}(\vec{r}_i, E)$, and $\rho(\vec{r}_i)$ are constant within the detector voxel i whose volume is V_i . Equation 3.1 is simplified as

$$\dot{D}_{ij} = C \cdot \int \Phi_{ij}(E) E \mu_{en}(E) / \rho_i dE. \quad (3.2)$$

The equation 3.2, for the discretized energy, is expressed as

$$\dot{D}_{ij} = C \cdot \sum_g \Phi_{g,ij} \bar{E}_g \bar{\mu}_{en,g} / \rho_i \quad (3.3)$$

where g indicates the energy group, $\Phi_{g,ij}$ is the average forward flux at the voxel i within the energy range g , \bar{E}_g is the average energy of the energy group g , $\bar{\mu}_{en,g}$ is the average energy absorption coefficient in the energy range g , and ρ_i is the average density of voxel i . This equation is simplified as

$$\dot{D}_{ij} = C \cdot \sum_g \Phi_{g,ij} CF_{g,i}, \quad (3.4)$$

where a flux-to-dose-rate conversion factor ($CF_{g,i}$) is defined as

$$CF_{g,i}(E_g, i) = C \cdot E_g \cdot \mu_{en}(E_g, i) / \rho_i \quad (3.5)$$

where $CF_{g,i}$ is the average conversion factor of the detector voxel i for the energy group g . The unit of CF is Gy·hr⁻¹/particles·cm⁻²·sec⁻¹. The CF for water material as a function of energy is shown in figure 3.1. Claiborne and Trubey calculated the gamma-ray flux-to-dose-rate conversion factors for x-rays in the energy range between 0.02 and 16 MeV in experiments performed in a 30-cm thick slab phantom [11]. Later on Wells and Livesay calculated the factors for the energy range 0.1keV to 1 MeV using the tissue kerma factor [72]. The American Nuclear Society (ANS) recommends analytic fits to calculate the conversion factors for x-rays based on the two studies, which reproduce the data to within $\pm 3\%$ accuracy for photons below 0.5 MeV [1].

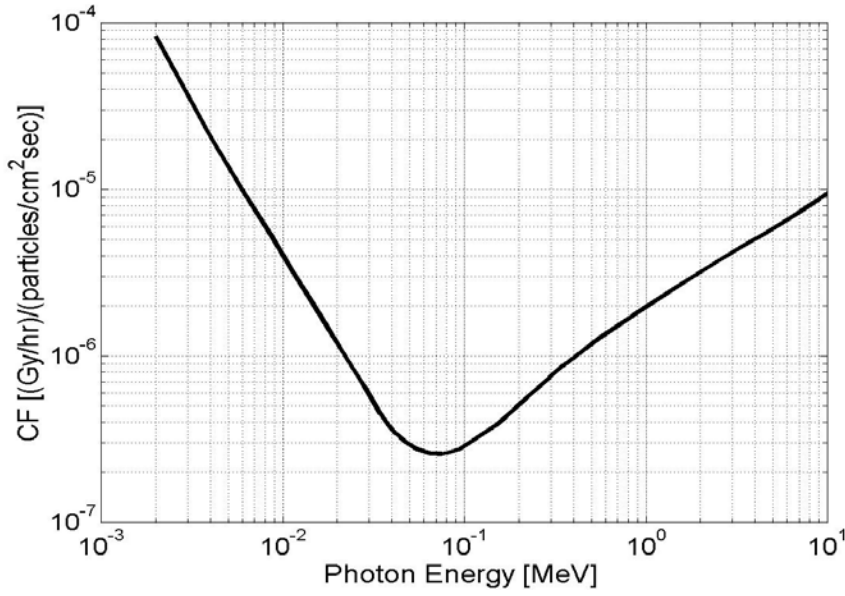


Figure 3.1 Flux-to-dose-rate conversion factor for photons in tissue vs. photon energy

Comparing equations 3.4 to 2.13, one notes that CF is equivalent to Q^+ . Therefore, the adjoint transport starts with CF at a detector voxel i as an adjoint source. The dose-rate is computed from equation 2.13,

$$\dot{D}_{ji}^+ = \iint \Phi_{ji}^+(\vec{r}_j, E) S_j(\vec{r}_j, E) dV dE , \quad (3.6)$$

where \dot{D}_{ji}^+ is the dose-rate to the voxel i from a source at j in the unit of $\text{Gy}\cdot\text{hr}^{-1}$. The ‘+’ indicates it is computed by the adjoint method. $\Phi_{ji}^+(\vec{r}_j, E)$ is the adjoint scalar flux at j (angle-integrated angular flux) obtained from transporting adjoint source at the detector i . The adjoint flux has the unit of $\text{Gy}\cdot\text{hr}^{-1}/\text{particles}\cdot\text{cm}^{-3}\cdot\text{sec}^{-1}$ and the source term $S_j(\vec{r}_j, E)$ has the unit of $\text{particles}\cdot\text{cm}^{-3}\cdot\text{sec}^{-1}$. $\Phi_{ji}^+(\vec{r}_j, E)$ and $S_j(\vec{r}_j, E)$ are constants within the source voxel j whose volume is V_j . This equation is simplified as

$$\dot{D}_{ji}^+ = \int \Phi_{ji}^+(E) S_j(E) dE . \quad (3.7)$$

The equation 3.7, for the discretized energy, is expressed as

$$\dot{D}_{ji}^+ = \sum_g \Phi_{g,ji}^+ \bar{S}_{g,j} \quad (3.8)$$

where $\Phi_{g,ji}^+$ is the average adjoint flux at the voxel j within the energy range g , $\bar{S}_{g,j}$ is the average source particle density in the voxel j for each energy group g .

A sample case was setup to verify the forward and adjoint dose computation methods. The sample case is a 13.9 cm by 13.9 cm tissue plane in 2-D having a 1 mm by 1 mm uniform resolution. It was assumed that the sample source emits photons whose energy range and intensity are between 20 and 30 keV and 0.4 mCi ($=1.48 \times 10^7$ Bq), respectively. The three-group photon cross-section library was extracted from the Fusion Evaluated Nuclear Data Library FENDL-2 175 neutron and 42 gamma-group cross-section library [51]. The three energy groups ranged from 1 to 30 keV where the first group, g_1 , spans 20 to 30 keV, g_2 10 to 20 keV, and g_3 1 to 10 keV. Table 3.1 presents the CF values for each energy group. The S_N was set to 16, which means the computation is performed with 144 discrete directions in DANTSYS (S_N basis model consists of $N(N+2)/2$ discrete directions). The 5th order Legendre polynomial expansion of the differential scattering cross-section (P_5) was used.

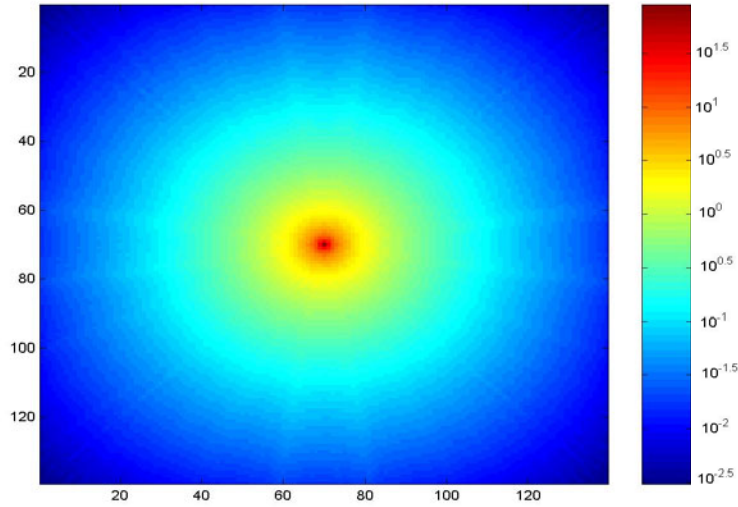
Table 3.1 summarizes the forward source and adjoint source for the discretized energy groups. To generate kernel data, the source is placed at the center voxel in the plane and detectors are distributed over all space for the forward transport computation. For the adjoint transport computation, the detector is placed at the center voxel in the plane and potential source voxels are distributed over all space. In forward transport, the detector response distribution is computed for

all detector voxels. In adjoint transport, the sensitivity distribution of the detector response to a source placement at any position is computed for all possible source voxels.

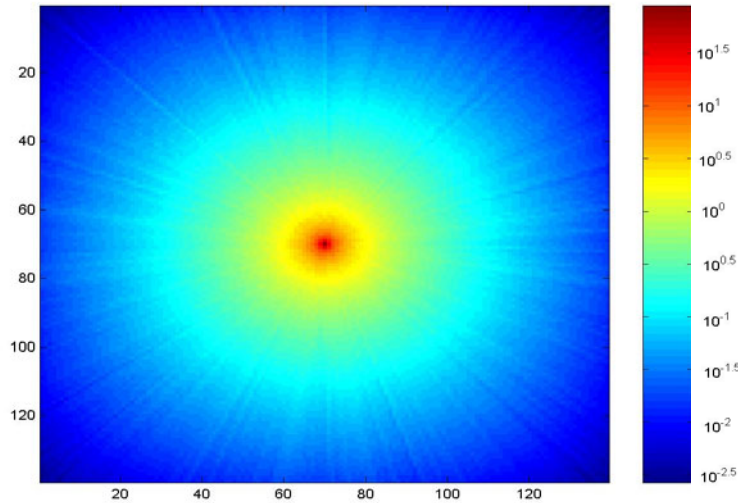
Table 3 .1 Forward and adjoint sources for the discrete energy groups

Energy group	Lower energy (keV)	Upper energy (keV)	Forward source Particles/cm ² sec	Adjoint source $CF=Q^+$ (Gy/hr)/(Particles/cm ² sec)
g1	20	30	1.48×10^9	8.26732×10^{-7}
g2	10	20	0	2.14514×10^{-6}
g3	1	10	0	3.29164×10^{-5}

Figure 3.2 illustrates the resulting forward kernel and adjoint kernel which are forward dose distribution and adjoint sensitivity distribution. Figure 3.2(a) is the forward detector response (dose) distribution. A unit source, 0.4mCi photons in the first group, is placed at the center of the plane. The forward detector response distribution represents the dose response to that source at the center. The dose-rate scale is logarithmic in units of Gy·hr⁻¹.



(a) Forward detector response distribution: logarithmic scale dose-rate distribution [$\text{Gy}\cdot\text{hr}^{-1}$]



(b) Adjoint sensitivity distribution of the detector response: sensitivity of dose-rate to a unit source $[(\text{Gy}\cdot\text{hr}^{-1})/0.4\text{mCi}]$, logarithmic scale.

Figure 3.2 (a) Forward detector response distribution. The dose-rate scale is logarithmic [$\text{Gy}\cdot\text{hr}^{-1}$].
 (b) Adjoint sensitivity distribution of the detector response. The scale is the logarithmic sensitivity of dose-rate per source-unit $[(\text{Gy}\cdot\text{hr}^{-1})/0.4\text{mCi}]$. Horizontal and vertical axes depict the x-y plane spatial extent in [mm].

Figure 3.2(b) is the adjoint sensitivity distribution of a detector placed at the center. The detector response function, that is the flux-to-dose-rate conversion factor, is placed at the detector location. Solving the adjoint transport provides the sensitivity distribution, which tells how much dose is delivered to the detector by placing a unit source at any position throughout the voxels in the plane. Therefore, the unit of the sensitivity distribution is dose-rate per source-unit, that is, $\text{Gy}\cdot\text{hr}^{-1}/0.4\text{mCi}$ for this example case. The adjoint distribution provides dose dataset in the detector's point of view whereas the forward distribution provides dose dataset in the source's point of view.

The distributions illustrated in figure 3.2 are scaled to the initial dose-rate from the source. The total dose from a permanent source is given as

$$D_i = \int_0^\infty \dot{D}_i \exp\left(\frac{-\ln 2^* t}{t_{1/2}}\right) dt \quad (3.9)$$

where D_i is the dose at a position i , t indicates the time in second, and $t_{1/2}$ is the half-life of a source. Solving the integration yields:

$$D_i = \dot{D}_i t_{1/2} / \ln 2. \quad (3.10)$$

3.1.2. Transposing dose matrix

From our experience with 2-D calculations using the DANTSYS code in Chapter 3.1.1, we found that the information an adjoint analysis would yield can be obtained through a forward analysis. The forward dose is equal to the adjoint dose provided that the positions of detectors and sources are consistent in both analyses.

$$D_{ij} = D_{ji}^+ \quad (3.11)$$

This relationship between forward and adjoint means that the adjoint dose is the transpose of the forward dose. Specifically, the entire adjoint dose for a particulate detector tissue voxel can be recovered from the forward calculated dose deposition data for every possible source position.

The recovery proceeds by first organizing the conventional dose deposition data into a matrix denoted as D_{ij} . This D_{ij} is a forward dose matrix, where the rows correspond to tissue voxels, and the columns correspond to seed positions. Hence, D_{ij} represents the dose to voxel i from a unit source located at seed j . In addition reading down an entire column j shows how a unit source at seed position j deposits dose in every voxel i . Alternatively, reading across an entire row i shows how a single voxel i receives dose from a unit source located at each source position j . This row information is actually the adjoint dose for the voxel i because it shows the doses received by voxel i from all possible source placements. Hence, the full adjoint dose matrix for all voxels may be recovered in a single step by taking the transpose of D_{ij} . This is shown in the equations 3.12 and 3.13.

$$D_{ij} = \{D_{ij} / \forall i \in N \text{ and } \forall j \in S\} \text{ and } D_{ji}^+ = \{D_{ji}^+ / \forall i \in N \text{ and } \forall j \in S\}, \quad (3.12)$$

where $N=\{1, 2, \dots, i, \dots, n\}$ indicates detector voxels and $S=\{1, 2, \dots, j, \dots, s\}$ indicates source voxels, and

$$(D_{ij})^T = \begin{pmatrix} D_{11} & \cdots & D_{1j} & \cdots & D_{1s} \\ \ddots & & \ddots & & \ddots \\ D_{i1} & & D_{ij} & & D_{is} \\ \ddots & & \ddots & & \ddots \\ D_{n1} & \cdots & D_{nj} & \cdots & D_{ns} \end{pmatrix}^T = D_{ji}^+ = \begin{pmatrix} D_{11}^+ & \cdots & D_{1i}^+ & \cdots & D_{1n}^+ \\ \ddots & & \ddots & & \ddots \\ D_{j1}^+ & & D_{ji}^+ & & D_{jn}^+ \\ \ddots & & \ddots & & \ddots \\ D_{s1}^+ & \cdots & D_{si}^+ & \cdots & D_{sn}^+ \end{pmatrix}. \quad (3.13)$$

3.1.3. Task Group No. 43 dose calculation

In the preliminary investigation with one 2-D slice of the patient data, we used the DANTSYS [77]. The resultant adjoint data set specified the sensitivity of the average dose, or dose-rate, in the tissue voxel to the placement of a unit-strength source at any seed position as shown in figure 3.2 (b). When we extended this technique to 3-D, however, we found that this code produced large cumbersome data set and proved to be an unwieldy tool for our specific needs. Since we had discovered that the adjoint data can be obtained from forward data set, it was decided to produce the adjoint data set using an alternative means.

The adjoint data set was obtained from the forward dose data computed using the protocol and data provided by the the task group 43 (TG43) of the American Association of Physicists in Medicine (AAPM) [48] for the revised air-kerma strength standard [74].

The dose-rate at a distant r from a source with the point source approximation is expressed as:

$$\dot{D}(r) = S_k \Lambda g(r) \phi_{an}(r) / r^2, \quad (3.14)$$

where $\dot{D}(r)$ is the initial dose rate at a distant r in the unit of $\text{cGy}\cdot\text{hr}^{-1}$, S_k is the air-kerma strength of the source in the unit of U. 1 U is equivalent to $1 \mu\text{Gy}\cdot\text{m}^2\cdot\text{hr}^{-1}$ [73]. Λ is the dose-rate constant of the source in water in the unit of $\text{cGy}\cdot\text{hr}^{-1}\cdot\text{U}^{-1}$. $g(r)$ is the radial dose function at a distance r cm away from the source. $\phi_{an}(r)$ is the anisotropy factor of the source calculated from the measured anisotropy function using point-source approximation. The dose for a permanent seed implant is computed by equation 3.10.

$\phi_{an}(r)$ is shown in table 3.2. A of ^{125}I model 6711 is $0.98 \text{ cGy}\cdot\text{hr}^{-1}\cdot\text{U}^{-1}$ [73], and $g(r)$ is a fit function to a 5th order polynomial:

$$g(r) = a_0 + a_1 r + a_2 r^2 + a_3 r^3 + a_4 r^4 + a_5 r^5 \quad (3.15)$$

where the coefficients of the function for the ^{125}I model 6711 are $a_0 = 1.01376$, $a_1 = 1.22747 \times 10^{-1}$, $a_2 = -1.73025 \times 10^{-1}$, $a_3 = 4.02378 \times 10^{-2}$, $a_4 = -3.85227 \times 10^{-3}$, and $a_5 = 1.34283 \times 10^{-4}$. Values for the distances not provided are obtained by interpolation and extrapolation. The dose over permanent time is computed using the equation 3.10 for 0.508U (0.4mCi) ^{125}I model 6711 whose half-life is 59.6 days. Figure 3.3 illustrates the 1-D dose fall-off. The computational resolution is 1 mm interval from the source position.

Table 3.2 The anisotropy factors of ^{125}I model 6711

Distance r (cm)	1	2	3	4	5	6	7
$\phi_{an}(r)$	0.944	0.936	0.893	0.887	0.884	0.880	0.901

An isotropic point source of Iodine-125 (^{125}I) radioactive seed is used to compute the dose deposition matrix D_{ij} with a voxel resolution of $1 \times 1 \times 5 \text{ mm}^3$. The compute dose is shown in figure 3.3.

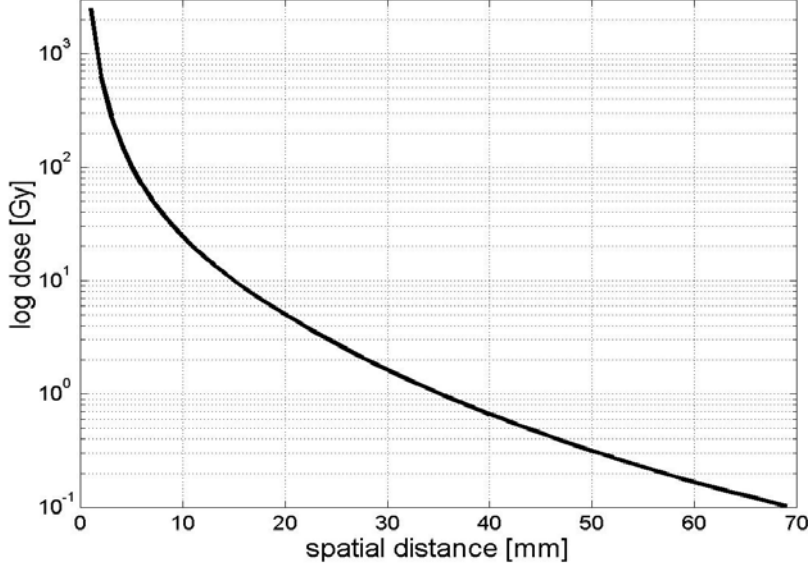


Figure 3.3 Dose [Gy] in logarithmic scale along distance [mm] obtained by TG43 formalism (equation 3.14)

3.2. Adjoint function of a region-of-interest (ROI)

We define the adjoint function of a voxel i as D_{ji}^+ , the dose delivered to the detector voxel i from a source at j . Given the uniform spatial mesh and homogeneous medium, these voxel-based adjoint functions are combined to construct an adjoint function for each tissue ROI. Since the detector is the ROI, which consists of voxels, summing up adjoint functions of all constituent voxels within the ROI and dividing the summation by the number of constituent voxels yield the adjoint function of the ROI, D_{jROI}^+ . D_{jROI}^+ indicates the average dose deposited in the ROI by a unit strength source placed at a particular seed position j . This is shown in the equation 3.16:

$$D_{jROI}^+ = \left(\sum_{i \in ROI} D_{ji}^+ \right) / N_{ROI}, \quad (3.16)$$

where N_{ROI} is the total number of voxels in the ROI.

Figure 3.4 shows the adjoint functions of ROIs of an example patient. The ROI geometry for a single plane of this patient is depicted in the prostate ultrasound image shown in figure 3.4(a). The ROI adjoint functions are shown in image-space in figures 3.4(b) through 3.4(f). Note that although the adjoint functions used in our optimization scheme are fully 3-D, these figures illustrate adjoint functions for only a single slice of the patient geometry. The x-y plane represents the cross-sectional image-space, and the z-axis indicates the average dose value per source-unit at any position in the x-y plane. We define the source-unit, S_u , as 0.4mCi of ^{125}I permanent seed. As an example of how to interpret these functions, consider the urethra adjoint shown in figure 3.4(d). The spatial distribution of this function roughly corresponds with the position of the urethra ROI as it is contoured in figure 3.4(a). Figure 3.4(d) illustrates that the urethra is obviously most sensitive to seed positions that lie within the urethra ROI, and least sensitive to seed positions far from the ROI. From this finding, we can see that we will deliver a larger average dose to an ROI if a source is placed in a seed position where the adjoint function has a large value, than if a source is placed in a seed position for which the ROI adjoint function has a small value. In terms of the optimization goal, a seed position that has a large adjoint function value for the target ROI but a small adjoint function values of the critical structure ROIs is desirable for source placement. This is because it will effectively irradiate the target ROI without severely damaging the critical structures. Thus, the adjoint function of an ROI presents intuitive means to measure the physical significance of source positions.

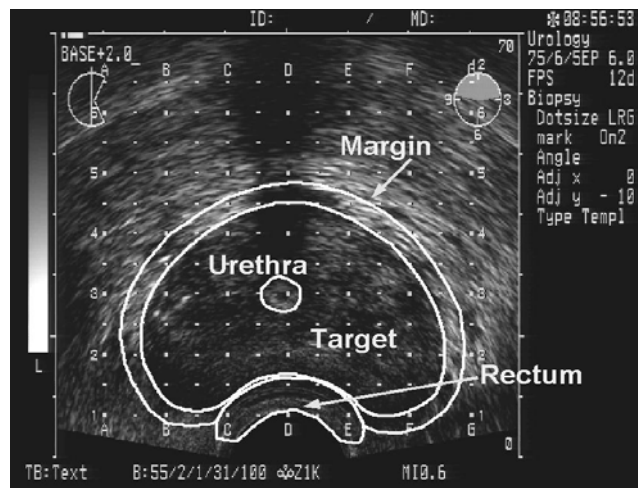


Figure 3.4(a) One slice of prostate transrectal ultrasound image with the ROIs contoured. The ROIs are target ROI, urethra ROI, rectum ROI and margin ROI. The rest surrounding area is the normal tissue ROI.

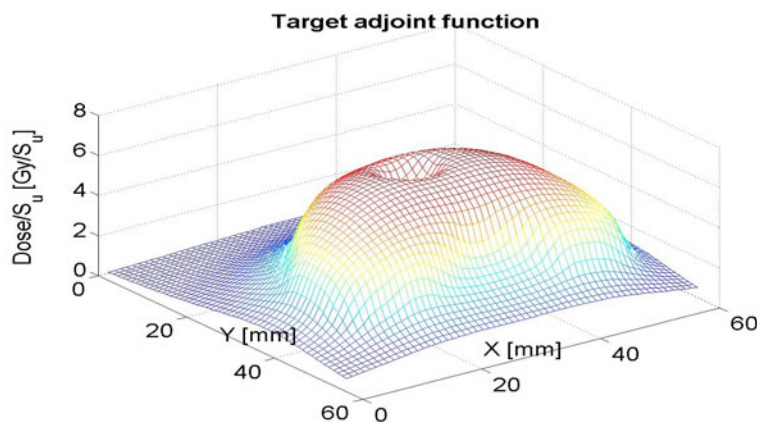


Figure 3.4(b) Adjoint function of the target ROI in image-space. The adjoint function is in $[Gy/S_u]$.

(continue)

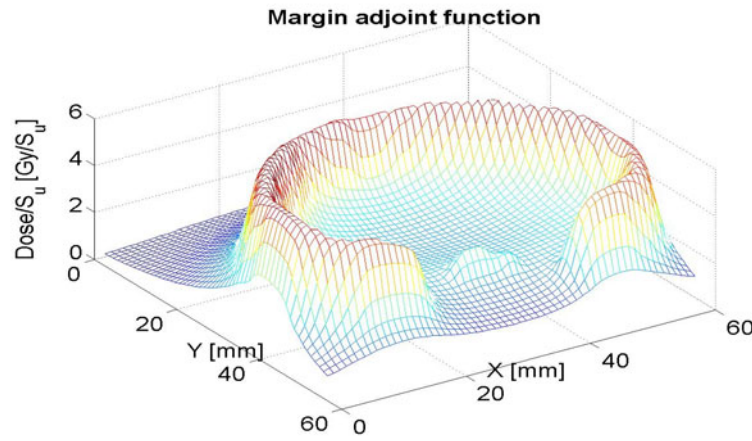


Figure 3.4(c) Adjoint function of the margin ROI in image-space.

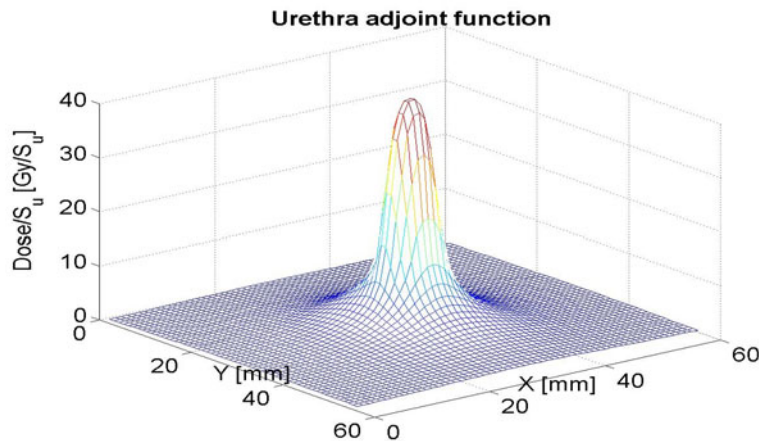


Figure 3.4(d) Adjoint function of the urethra ROI in image-space.

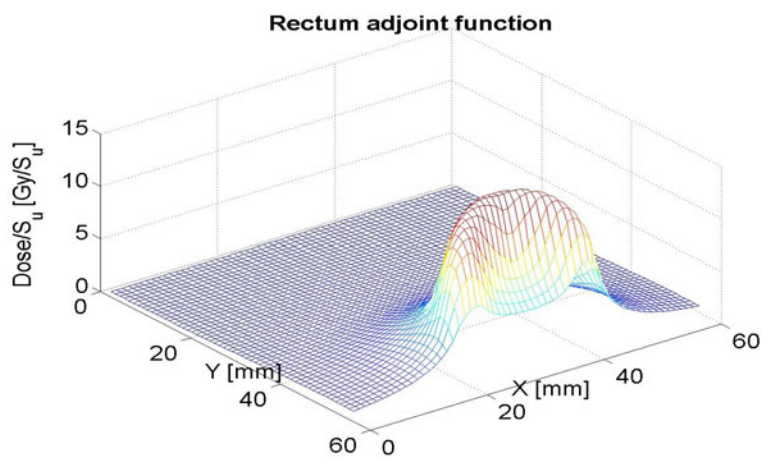


Figure 3.4(e) The adjoint function of the rectum ROI in image-space.

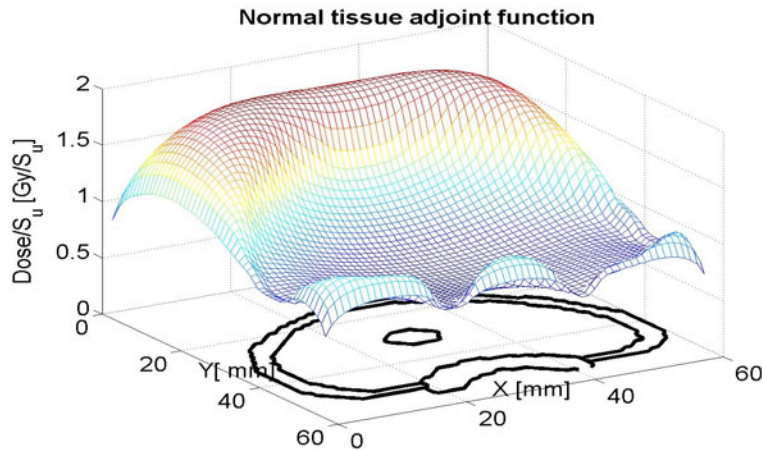


Figure 3.4(f) The adjoint function of the normal tissue ROI in image-space with the contoured ROIs on the image plane.

Figure 3.4 (a) One slice of prostate transrectal ultrasound image with the ROIs contoured. (b) – (f) Adjoint function of each ROI in image-space. Adjoint function is the sensitivity of the dose per source-unit [Gy/S_u] in the ROI from a source at an arbitrary seed position, where the source-unit, S_u, is 0.4mCi ¹²⁵I permanent seed.

Figure 3.4(b) through (f) illustrate the adjoint functions in image-space. However, the template grid within the target region restricts the source positions. The template is a perforated lattice-apparatus, which allows for needle insertion. The insertion points are shown as white dots in figure 3.4(a). They are 5 mm apart from each other in the vertical and horizontal directions. There are a total 50 of possible seed positions in this image. Figure 3.5 maps all of the adjoint functions of figure 3.4 onto a single plot as a function of seed position. The 50 possible seed positions are sequentially ordered along the horizontal axis in figure 3.5.

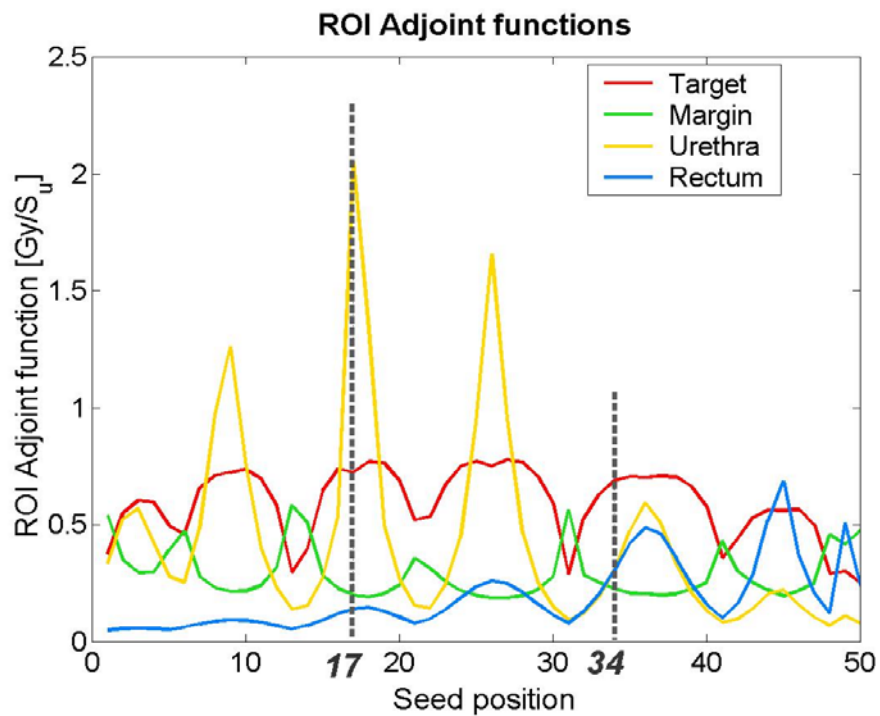


Figure 3.5 Adjoint functions of ROIs at each seed position. The horizontal axis indicates seed positions and the vertical axis in the adjoint function as the dose per source-unit [Gy/S_u]. This value is the average dose deposited to each ROI by a 0.4mCi ¹²⁵I permanent seed as a function of seed position.

Figure 3.5 illustrates the values of the ROI adjoint functions at each seed position in a single view. The red line is the target adjoint function, the green the margin, the yellow the urethra and the blue the rectum. As an example of how to profit from this plot, it is easily seen that a source at seed position 17 will deliver a much larger average dose to the urethra than to the target ROI. On the other hand, a source at position 34 will deliver a high average dose to the target ROI but a low average dose to the urethra and rectum ROIs. These observations are directly relevant to our treatment-planning problem of positioning sources so as to deliver a large dose to the target but small dose to the critical structure ROIs effectively.

3.3. Adjoint ratio

The previous chapter discussed the physical significance of an ROI adjoint function that provided the sensitivity of the average dose deposited in the ROI to a source position. This understanding of the adjoint functions is implemented in the optimization process. To capture such observations with a single metric that will consider all of the adjoint functions simultaneously, we define an “adjoint ratio” for each seed position. The adjoint ratio for a seed position j is a sum of the adjoint values for critical structure ROIs divided by the adjoint value for the target ROI. This ratio, $R(j)$, is computed as:

$$R(j) = w_{urethra} \left(\frac{D_{j \text{ urethra}}^+}{D_{j \text{ target}}^+} \right) + w_{rectum} \left(\frac{D_{j \text{ rectum}}^+}{D_{j \text{ target}}^+} \right) + w_{margin} \left(\frac{D_{j \text{ margin}}^+}{D_{j \text{ target}}^+} \right) \quad (3.17)$$

where the w_{ROI} is a weighting for each critical structure ROI relative to the target.

Figure 3.6 illustrates the adjoint ratio in image-space. The adjoint ratio for each voxel position in image-space is computed using equation 3.17 with equal weightings for ROIs. The seed position that has the minimum adjoint ratio value among all positions is marked ‘o’. As an example of how to comprehend this adjoint ratio distribution, the adjoint ratio values are high near the urethra, rectum, or the periphery of the target, but low around the center lobes of the target. It is observed that the seed positions with low adjoint ratio values are profitable positions for they would deliver high dose to the target. On the other hand, the seed positions with high adjoint ratio values are detrimental to the critical structures.

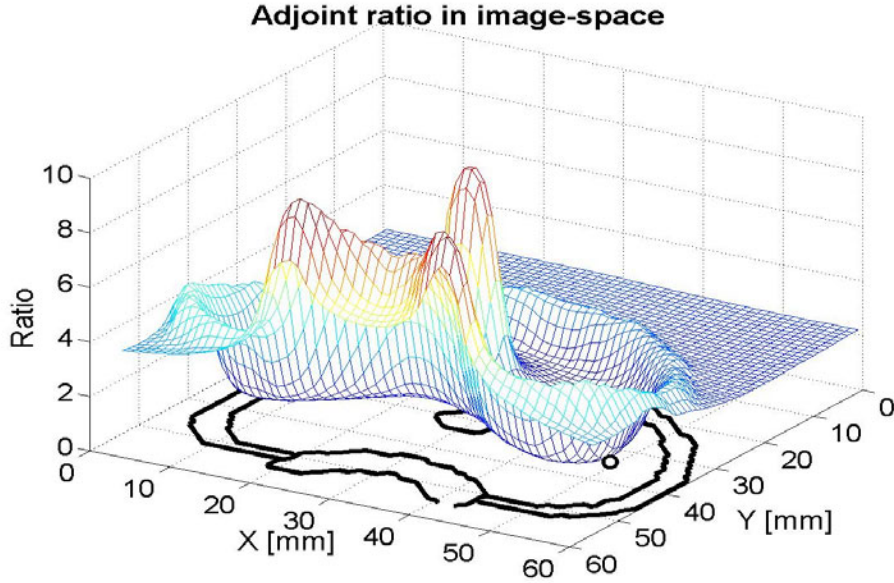


Figure 3.6 Adjoint ratio in image-space. The adjoint ratio is obtained using equation 3.17 with all weightings set to unity. The seed position that has the minimum adjoint ratio is marked ‘o’ in this image-space.

Figure 3.7 maps the seed positions in image-space and the adjoint ratios of figure 3.6 onto a sequentially aligned seed position plot as a function of corresponding seed position. There are a total 50 possible seed positions within the target ROI. Among these 50, the position marked ‘o’ has the minimum adjoint ratio, that is, this seed position will simultaneously deliver the largest dose to the target while sparing the critical structure the most. In figure 3.7, it is readily apparent that position 30 is the best seed position for meeting out treatment plan goal because it delivers the largest dose possible to the target ROI while simultaneously delivering a small average dose to the critical structure ROIs. Hence, the distribution of $R(j)$ provides a means of ranking seed positions in terms of treatment plan objectives prior to any actual optimization process. In addition, the adjoint ratio illustrates how the ROI adjoint functions can effectively guide a seed placement strategy.

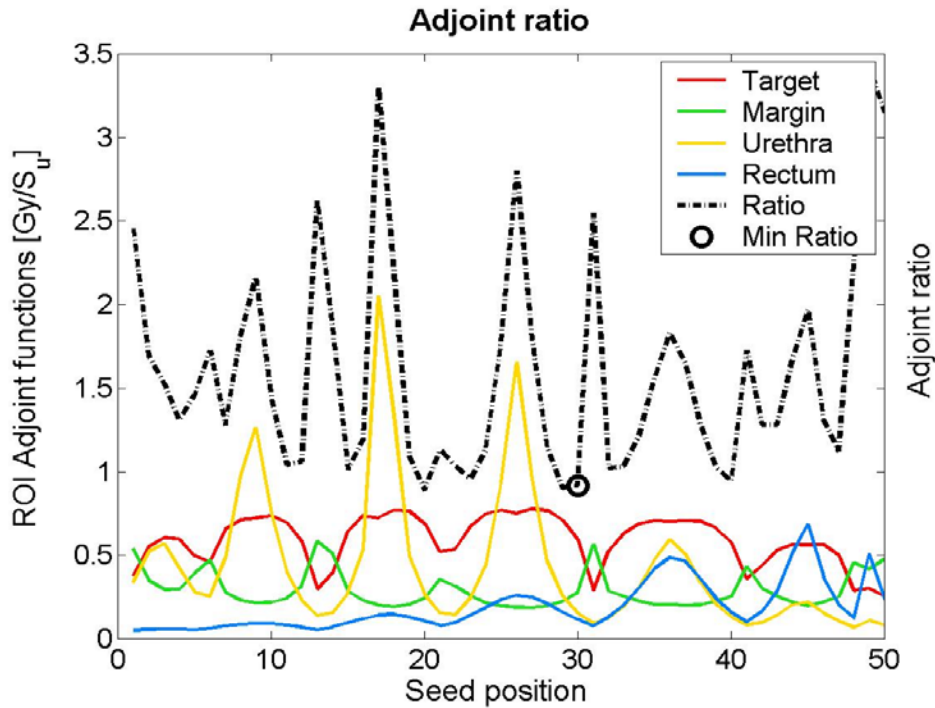


Figure 3.7 Adjoint ratio, $R(j)$, and ROI adjoint functions at each seed position. The horizontal axis indicates seed positions, the left vertical axis indicates the adjoint function as the dose per source-unit [Gy/S_u], and the right vertical axis indicates the unitless adjoint ratio.

3.4. Discussion

This chapter reviewed the forward and adjoint dose computation methods for discretized energy, angle, and space bins. Consequently the adjoint method yields the same dose quantity as the forward method. However, the adjoint analysis endows the source positions with sensitivity of the dose deposited in a detector. The adjoint dose distribution of a detector represents sensitivity distribution of dose per source-unit. The adjoint function of an ROI is defined as the sensitivity of the average dose deposited in the ROI to a unit source placed at any seed position.

We introduced the adjoint ratio that combines the adjoint functions of all ROIs as a function of seed position. Seed positions can be ranked according to their adjoint ratio values. This adjoint ratio is *a priori* knowledge that will be exploited in an optimization process.

This adjoint information has been discussed in external beam therapy for determination of beam orientation [25], and improvement of the initial guess [17, 29, 35]. In addition, Difilippo suggested that the adjoint ratio of the target ROI adjoint function to the normal tissue ROI adjoint function can be used as the cost function for the treatment planning optimization [17]. However, the adjoint information has not been employed for the brachytherapy area [78], and the adjoint ratio has not been used in an actual optimization study for radiation treatment plan. We will implement this adjoint ratio into the brachytherapy treatment planning optimization to determine an optimal seed configuration.

Chapter 4

Greedy heuristic for a seed-configuration

4.1. Introduction

This chapter reports on a new optimization algorithm for prostate implant treatment planning. This optimization method is based on the adjoint function for each tissue ROI and on a greedy heuristic. The adjoint function of a tissue ROI is defined as the average dose deposited in the ROI by a unit-strength source placed at any seed position. Therefore, the adjoint function describes the sensitivity of the average dose deposited in the ROI to changes in seed position. For each seed position, we compute an adjoint ratio that is the sum of the adjoint values for critical structure ROIs divided by the adjoint value for the target ROI as explained in Chapter 3.2. Inspection of these ratios enables a quick determination of which seed positions do the best job of irradiating the target ROI while sparing critical structure ROIs [17]. The greedy heuristic performs this inspection and designs the implant by consistently choosing the most favorable seed positions.

This method is fundamentally different from other optimization methods for prostate implant treatment planning, such as simulated annealing [52, 55], genetic algorithms [22, 38, 79], and the branch-and-bound method [19, 38]. The reason comes from the physical significance of the ROI adjoint functions, which provide *a priori* knowledge about seed positions to guide the optimization process. The other optimization methods do not rely on a physical basis for considering potential seed positions until they compute dose to evaluate the seed positions. Many such trials and evaluations are necessary before an acceptable seed configuration is made. The greedy heuristic generates a complete seed configuration with a recipe that exploits the physical information available from the ROI adjoint functions without trials or evaluations.

This chapter discusses the preliminary endeavor to develop the greedy heuristic, which makes use of the adjoint ratio [78]. How the adjoint ratio guides seed-selection process and how an isodose surface constraint restricts the search space are highlighted in this chapter. The resulting treatment plan obtained by the greedy heuristic is compared to the treatment plan obtained by the branch-and-bound method.

4.2. Methods and Materials

4.2.1. Greedy heuristic

The optimization strategy in this work is a greedy heuristic. Heuristic or approximate optimization methods are designed to find good solutions for a specific problem quickly. Methods of this kind are valuable although they might not guarantee optimality. Computational experience with algorithms that guarantee an optimal solution has not been completely encouraging because most

real problems are too large to be solved exactly [24]. The greedy heuristic attempts to construct an optimal solution step-by-step. At each step, it makes a decision that appears to be the best under some criterion at the time. The criterion used to make the greedy decision at each step is called the greedy criterion [59]. Since the decision made in each step is not revised in subsequent steps, the greedy criterion must be formulated so that each decision assures the feasibility of the overall solution.

Greedy heuristic strategies are well known for 0/1 problems such as the vertex-covering problem, the knapsack problem, etc [59, 66]. In the instance of the vertex-covering problem, the goal is to find a set of vertexes to cover most edges. A greedy method invariably continues choosing a vertex set in order of the most edges covered by the vertex [66]. In the knapsack problem, the goal is to pack as many items in the sack as possible [59]. The greedy heuristic considers the items in order of decreasing capacity. Thereby, items with small capacity are packed before those with large capacity.

A general idea of a simple greedy heuristic for a minimizing problem is expressed as [51]:

Initialization. $Q^0 = \emptyset, t = 1$.

Step t. Let j^t minimize $\min_{j \in N \setminus Q^{t-1}} z(Q^{t-1} \cup \{ j \})$ with ties broken arbitrarily.

If $z(Q^{t-1} \cup \{ j^t \}) \geq z(Q^{t-1})$, stop. Q^{t-1} is a greedy solution.

If $z(Q^{t-1} \cup \{ j^t \}) < z(Q^{t-1})$, set $Q^t = Q^{t-1} \cup \{ j^t \}$.

If $Q^t = N$, stop. N is a greedy solution.

Otherwise, $t \leftarrow t + 1$. (4.1)

The heuristic starts with the initialization of the empty solution set, Q^0 , and the 1st step, $t=1$. An element j^t at the t^{th} step is chosen such that the solution set including j^t , $Q^{t-1} \cup j^t$, minimizes the greedy criterion z . If the greedy criterion at the current step t yields greater value than the one at the previous step $t - 1$, the previous solution set, Q^{t-1} , becomes the greedy solution. If the greedy criterion at the current step has a smaller value than the previous step, the element j^t is added onto the solution set Q^{t-1} resulting in Q^t . If the solution set consists of all possible elements N , the process stops and the current solution becomes a greedy solution. Otherwise, the process repeats this procedure for the next step. Given a solution set Q^t , the next decision made, j^t , is one that gives the greatest immediate decrease in the greedy criterion value, provided that such a decision is valid. Moreover, once a decision j^t is made, it is included in the solution set Q^t and kept throughout the algorithm. Thereby, the greedy heuristic achieves a final solution quickly.

One noticeable feature in the greedy heuristic is that an element, j , is included in a solution, Q , and there is not modification following in a subsequent step. Another noticeable feature is that an element, j , is selected only if it satisfies the greedy criterion, z .

We revise this general greedy heuristic idea for the specific application of prostate implant treatment planning. An element represents a seed position, and a solution represents a seed configuration, which consists of seed positions. A seed position will be selected only if it satisfies our greedy criterion, and once a seed position is added to a seed configuration, it will not be taken back.

In this work, the goal of an optimization is to design a seed configuration that delivers a desired dose distribution to the target ROI, avoiding the critical structure ROIs. We propose a greedy heuristic for this problem to enhance the efficiency in computational time, preserving the quality of a seed configuration. The greedy criterion for selecting a seed position at each step is

based on the adjoint ratio, which is pre-computed for each seed position. The adjoint ratio has been defined in Chapter 3. The adjoint functions of all ROIs are combined in the adjoint ratio as a function of seed position. Since the target adjoint function is in the denominator and the critical structures' adjoint functions are in the numerator, the smaller the adjoint ratio the higher the dose to the target yet the lower the dose to the critical structures. In this manner, the adjoint ratio estimates which seed position within the search space would perform the best job at each step for achieving the goal. A selected seed position is added to a seed configuration at each step until a termination criterion is achieved.

The greedy heuristic for prostate implants in this study is illustrated with details in the following pseudo-code:

Initialization.

Empty seed configuration; $Q^0 = \emptyset$,

all seed positions within the target \in search space; $\forall j \in X^0$, where $j \in \text{target}$,

1st step; $m=1$

Step m.

Search space X^m satisfies $D_{XQ^{m-1}}^{m-1} \leq C_{iso}^m$

If $X^m = \emptyset$, reset C_{iso}^m , and starts from initialization.

Otherwise, select j^m minimizing $R(j)$, where $j^m \in X^m$

$$Q^m = Q^{m-1} \cup j^m \text{ and } D_{iQ^m}^m = D_{iQ^{m-1}}^{m-1} + D_{ij^m}, \forall i \in \text{target}.$$

If target coverage $\geq C_{coverage}$, stop. Q^m is a greedy solution.

Otherwise, $m = m + 1$. (4.2)

The heuristic initializes a seed configuration, Q , to an empty set, and the search space, X , to the whole target ROI. The search space consists of all possible seed positions that have not yet been selected yet within the target ROI at the beginning. The greedy heuristic searches a seed position j that yields the minimum $R(j)$ among all possible seed positions in the search space X . The selected seed position j is included in the seed configuration, Q , and the dose distribution, D , is computed. If the resulting dose distribution accomplishes the target coverage greater than $C_{coverage}$, the process terminates and the current seed configuration is a greedy solution. If not, it moves onto the next step. In the case of an empty search space, a user should reset C_{iso}^m and starts from the initialization. Table 4.1 lists all parameters used in the pseudo-code and their definitions.

Table 4.1 Definitions of parameters in the pseudo-code 4.2

Parameters	Details
m	The order of step.
i	Tissue voxel in ROIs.
j	Seed position within the target ROI limited by the template grid.
j^m	Selected seed position at the m^{th} step.
Q	Seed configuration that consists of selected seed positions.
Q^0	Initial seed configuration, which is empty.
Q^m	Seed configuration at the m^{th} step.
X	Search space
X^0	Initial search space. An area within the target ROI.
X^m	Search space at the m^{th} step. An area enclosed by the isodose surface C_{iso}^m within the target ROI
$R(j)$	Adjoint ratio as a function of seed position. Greedy criterion.
D_{ij^m}	Dose to a tissue voxel i due to a seed at j^m .
$D_{iQ^m}^m$	Dose to a tissue voxel i due to seeds in the seed configuration Q^m at the m^{th} step.
$D_{XQ^{m-1}}^{m-1}$	Dose to a tissue voxel i within the search space X due to seeds in the seed configuration Q^{m-1} at the $(m - 1)^{\text{th}}$ step.
C_{iso}^m	Isodose surface constraint at the m^{th} step. The superscript ‘m’ indicate the step order.
$C_{coverage}$	Target coverage constraint.

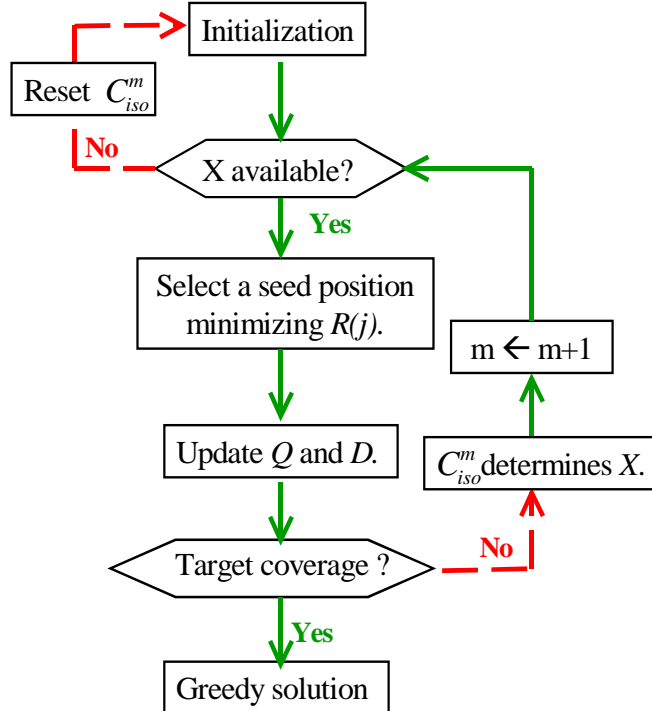


Figure 4.1 Flowchart of the greedy heuristic.

This optimization process is briefly visualized in the flowchart shown in figure 4.1. Starting with initialization, if the search space, X , is ‘available’, a seed position that gives minimum adjoint ratio value is selected. If X is ‘not available’, a user should reset the isodose surface constraint, C_{iso}^m . Q and D are updated. If the target coverage satisfies a termination criterion, Q becomes a greedy solution. Otherwise, the C_{iso}^m value is updated to newly determine X for the next step. The process continues adding a seed position onto the seed configuration until a termination criterion is reached. Note that when there is at least one possible seed position that has not been selected yet, the search space is considered ‘available’. When there is no possible seed position within the search space, the search space is considered ‘not available’.

4.2.2. Isodose surface constraint

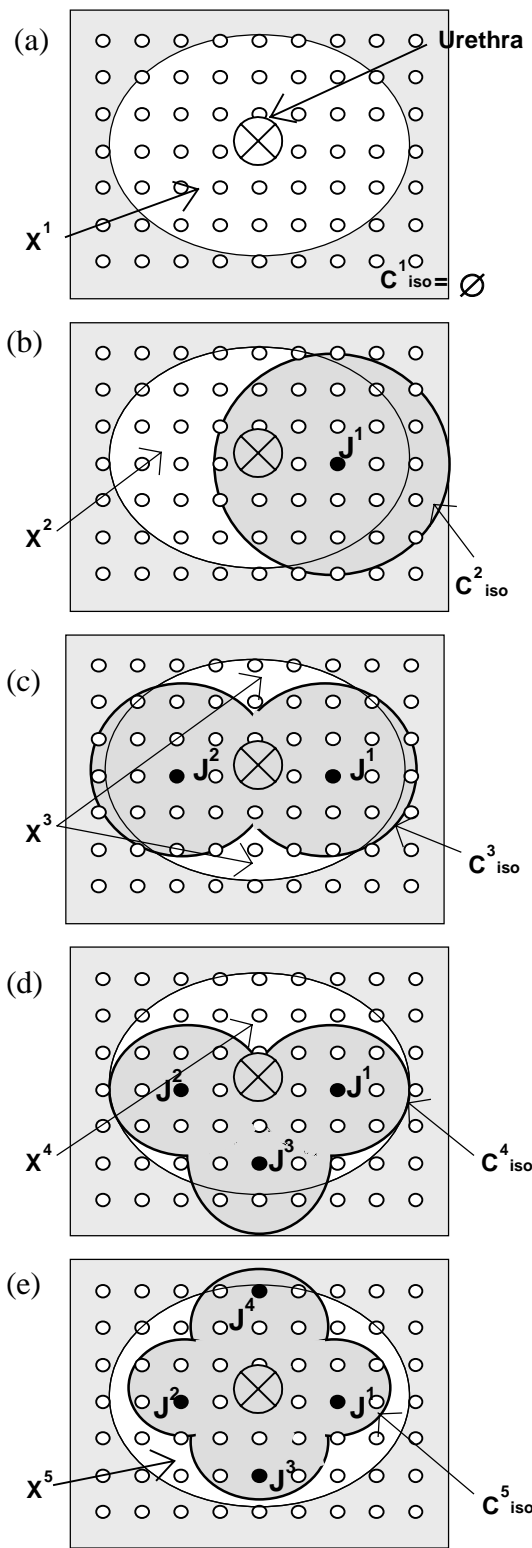


Figure 4.2 Placement of first four sources in the greedy heuristic. See text.

An isodose surface constrain, C_{iso}^m , restricts the search space, X . Figure 4.2 illustrates the relationship between the search space and an isodose surface constraint in a simple step-by-step diagram. The small white circles represent the possible seed positions in the template grid, the small black circles represent the selected seed positions, the large white oval structure represents the target ROI, and the cross-marked circle at the center represents the urethra ROI. The search space is in white color; hence the seed positions in the gray area are excluded from the search space.

The initial search space, X^I , includes all possible seed positions inside of the target, as shown as white in figure 4.2(a). In the 1st step, the greedy heuristic searches X^I for a seed position, which has a minimum adjoint ratio value. The seed configuration now consists of a single seed, which is denoted as j^I and is colored black in figure 4.2(b). Based on this seed configuration, the dose to every target voxel is computed, and an isodose surface is drawn to restrict

the search space to X^2 . The isosurface is defined by the value of the isodose surface constraint C_{iso}^2 , which will be explained in later paragraphs. As shown in figure 4.2(b), the white search space X^2 includes possible seed positions within the target but outside of the isodose surface. In the 2nd step, the seed configuration is expanded by placing a seed at the position j^2 that has the minimum ratio value among all available seed positions in X^2 . With this configuration, the dose to every voxel in the target is updated, and an isodose surface is drawn to restrict the search space to X^3 . These updated quantities are shown in figure 4.2(c). Figure 4.2(d) and 4.2(e) show that additional seeds are added in the next steps in a similar fashion. This process continues until the target coverage (the volume of the target enclosed by the prescribed dose) reaches a termination criterion. The next section 4.2.3 discusses the termination criterion.

Figure 4.3 illustrates the feature of figure 4.2 in the contoured 3-D prostate image. Figure 4.3(a) is the initial step. Figure 4.3(b), (c), and (d) are the 2nd, 3rd, and 4th step respectively. Figure 4.3(e) is the 20th step, and figure 4.3(d) is the 57th step. The prostate is in red and the rectum is in yellow. The dark hole at the center of the prostate is the urethra. The blue is the isodose surface. The volume enclosed by the blue surface represents high-dose region; the dose higher than C_{iso}^m . The search space X is within the prostate, the red area, but excluding the volume enclosed by the isodose surface, the blue area. The isodose surface constraint prevents a consecutive seed from being placed next to the previous seed. It is observable that the available search space decreases as the order of the step increases.

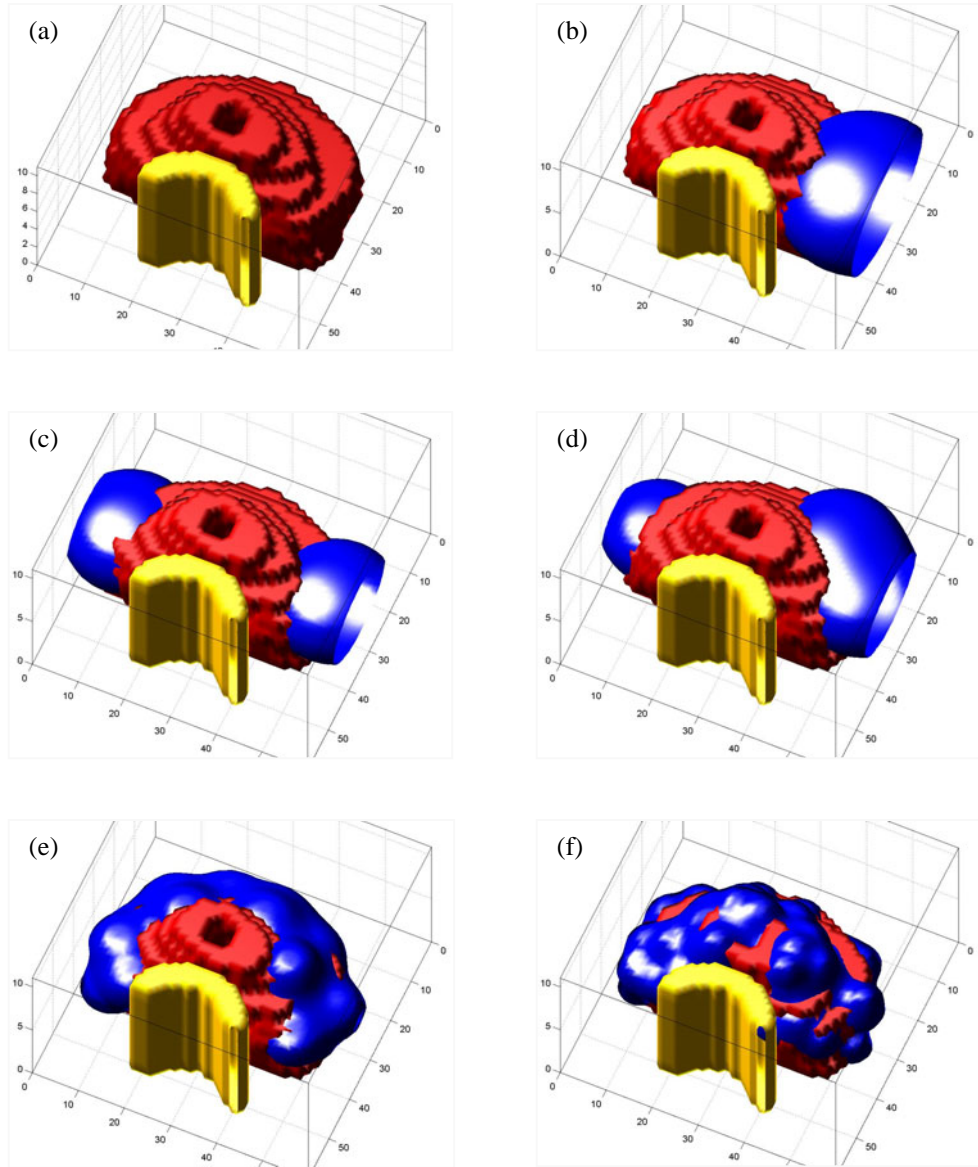


Figure 4.3 Isodose surface constraint at each step – (a) 1st, (b) 2nd, (c) 3rd, (d) 4th, (e) 20th and (f) 57th step. 3-D prostate image; red is target (prostate), dark hole at the center is urethra, yellow is rectum, and blue surface is the isodose surface. The search space X is inside of the red area but excludes the volume enclosed by the blue surface.

The isodose surface specified by the isodose surface constraint, C_{iso}^m , determines the tissue volume within the target to be excluded from the search space. This constraint is a dynamic value that increases in proportion to the number of seeds in the seed configuration. Its purpose is to restrict the search to seed positions where the dose is less than the constraint value. Note that as C_{iso}^m increases, the volume enclosed by the isodose surface decreases. We adjust C_{iso}^m with the expression:

$$C_{iso}^m = \alpha \times (m - 1), \quad (4.3)$$

where α is a user set value, which will be explained in the next paragraph. m is the current number of seeds, that is the same as the step order.

We tested the greedy heuristic on an example patient. In this example, α is set to 1.77 % of the prescribed dose D_p . The value 1.77 % was chosen for α based on an investigation of the ability of a single seed to deliver the prescribed dose to the entire target volume. This ability depends on the target volume and the strength of a seed. Therefore, it is a patient-dependant value. It also varies with seed position within the target. For instance, the average dose to the target is high for a seed placed at the center of the target, but is low for a seed placed on the periphery because a considerable amount of dose is wasted on the volume outside of the target. We found that the minimum average dose delivered to the example target by a single source was 1.48% of D_p . This minimum case occurs for a source placed at the least efficient seed position. In this regard, an initial value for α was set to 1.48% of D_p . However, even though the α value should be set small enough to prevent seed clustering, it must also be set high enough to allow the search space to contain seed positions. To enable this flexibility, we tested increasing values of α , starting from 1.48 % of D_p , and found that 1.77 % was the minimum value that enabled the greedy

heuristic to successfully construct a seed configuration. A successful configuration is characterized as having the target coverage greater than $C_{coverage}$.

4.2.3. Termination criterion

Theoretically, an optimization process should terminate when it reaches an optimal solution. However, a stochastic method usually gets trapped on a local optimum. A deterministic method, such as branch-and-bound, can eventually find a global optimum, although it would take several days in the case of 3-D prostate implants. Most optimization processes for radiation therapy terminate when they reach a certain number of iterations with a feasible solution, or when the convergence occurs within a small range.

In a general greedy heuristic, the process terminates when adding an element doesn't improve a greedy criterion, or when all elements have been selected. In this study, the greedy heuristic for prostate implants repeatedly selects a seed position and adds it onto the seed configuration. When a termination criterion is reached, the process stops and the current seed configuration becomes a greedy solution. The termination criterion used in this study is that the target coverage should be greater than the $C_{coverage}$, which is 98% of the target volume. Therefore, a successful configuration will produce a target coverage, which is always greater than 98% of the target volume. This termination criterion guarantees sufficient target coverage as well as assures the final destination of the process.

4.2.4. Branch-and-bound for a basic mixed-integer programming model

The branch-and-bound method for a basic mixed-integer programming model is used for comparison with the greedy heuristic method. An optimization problem, which consists of continuous and integer variables, is called mixed-integer programming (MIP). In the problem of prostate implants, the decision variable is an integer value 1 or 0 that represents placement or non-placement of a seed. The dose at each tissue voxel is expressed in a real continuous value. Thus, a mixed-integer programming model can represent an optimization problem of a seed configuration for prostate implants. Lee *et al.* [38] and D’Souza *et al.* [19] used a branch-and-bound method to solve a mixed-integer programming model for prostate implants. The branch-and-bound approach is employed in most commercial codes for integer and mixed-integer programs [45, 75], and is well known for being an effective optimization tool [43].

We built a basic mixed-integer programming model similar to those of Lee *et al.* [38] and D’Souza *et al.* [19] and use branch-and-bound to solve the model. The model involves minimizing total penalties. The dose deviations from constraints summed over all voxels in all ROIs contribute to the penalties. This basic model is stated as follows:

$$\begin{aligned}
& \text{minimize} && \sum_{ROI} \sum_{i \in ROI} (w_{ROI} \cdot z_i) \\
& \text{subject to} && \left\{ \begin{array}{l} D_i + z_i \geq L_{ROI}, \\ D_i - z_i \leq U_{ROI}, \text{ and} \\ D_{i \in target} \geq minD_{target}, \end{array} \right. \\
& && \text{where } z_i \geq 0, D_i = \sum_j x_j \cdot D_{ij}, x_j \in \{0, 1\}, \text{ and} \\
& && ROI \in \{\text{target, margin, urethra, and rectum}\}
\end{aligned} \tag{4.4}$$

where z_i is the penalty at each tissue voxel i . If the computed dose to a voxel i is lower than a lower dose constraint, the underdose amount contributes to the penalty. If the computed dose to a voxel i is greater than an upper dose constraint, the overdose amount contributes to the penalty. The binary variable x_j indicates a seed placement, 1, or non-placement, 0, at a seed position j . w_{ROI} is a weighting for the ROI. D_{ij} is computed using the equations 3.14 and 3.10. L_{ROI} and U_{ROI} represent lower and upper dose constraints, which are soft constraint incorporated in the objective function. These soft constraints can be violated but the violation will increase the objective function. Depending on the desired dose level, those values are determined. $minD_{target}$ is a hard-constraint imposed over the targetROI; the minimum dose to a voxel in the target will be greater than this value. Because the hard-constraint is not incorporated in the objective function, a feasible solution will always satisfy the hard constraint.

Table 4.2 lists values of all constraints and parameters used in the basic model. The prescribed dose, D_p , is 145Gy to the target. The dose to the target greater than a certain level is a high dose, which causes the dose distribution to be inhomogeneous. In order to prevent this high dose region in the target, the upper dose constraint for the target is set to 150% of D_p . The margin

ROI is a buffer zone, which mitigates dose distribution between the target and the normal surrounding tissue; the dose distribution should conform the prescribed dose to the target without severely damaging the normal surrounding tissue. Hence, the range of dose to the margin is set to $\pm 20\%$ of D_p . Since it is desired to achieve as low dose as possible in the urethra or rectum, the lower dose constraints are set to zero. The hard constraint $\min D_{target}$ is set to 90% of D_p .

Table 4.2 Constraints and weightings for the basic model

	Target	Margin	Urethra	Rectum
w_{ROI}	1	1	1	1
L_{ROI}	$1.0 \times D_p$	$0.8 \times D_p$	$0.0 \times D_p$	$0.0 \times D_p$
U_{ROI}	$1.5 \times D_p$	$1.2 \times D_p$	$1.25 \times D_p$	$0.8 \times D_p$
$\min D_{target}$	$0.9 \times D_p$	NA	NA	NA

4.2.5. Optimization environments

The ultrasound images of the prostate are taken and transferred to an image file. The image file is read, and the ROIs are manually contoured slice-by-slice in MATLAB [41]. This information of the contoured ROIs is saved as a matrix form, which MATLAB can reload. The greedy heuristic is coded in MATLAB, in which a solution can be analyzed. The basic mixed-integer programming model is coded in the General Algebraic Modeling System (GAMS) [7], which has been used in the field of radiation therapy optimization. GAMS is a modeling system that involves a language compiler, which interfaces with CPLEX solvers. CPLEX solvers are

designed to solve linear programming models or mixed-integer programming models. The branch-and-bound method is used in the CPLEX mixed-integer programming solver. The matrixes of the contoured ROIs are rearranged to a format that is accessible to GAMS. A solution generated by GAMS is processed via the MATLAB-GAMS interfacing software [23] into a format accessible to MATLAB, in which the solution is analyzed.

4.3. Results and discussion

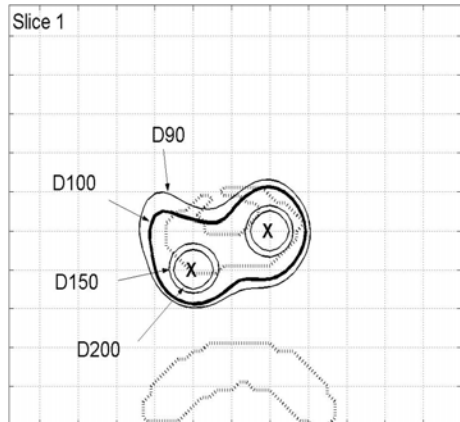
The images of a prostate are taken by TRUS in 5 mm intervals, and each 2-D image slice is processed to 1 mm x 1 mm resolution in a 60 x 55 mm² area. The target volume of this prostate is 33.06 cc. A voxel thickness corresponds to the image slice thickness. Thus the voxel resolution is 1 mm x 1 mm x 5 mm. The contoured target ROI is the planning target volume (PTV) [30], over which the prescribed dose is imposed. The prescribed dose, D_p , is set to 145 Gy. The margin area is introduced around the target ROI in order to conform the dose to the target simultaneously sparing the surrounding normal tissue. In this manner, the surrounding normal tissue, which consists of the many more voxels than any other ROI, does not need to be considered separately.

We performed all computations with a Compaq Alpha 667 MHz computer. The greedy heuristic generated a treatment plan in 1.07 CPU seconds while the branch-and-bound method achieved a feasible solution within 3167CPU seconds. Note that the branch-and-bound's feasible solution is one that satisfied all constraints, but was not necessarily an optimal solution. The number of seeds used in the branch-and-bound method was 58 and the greedy heuristic used 59

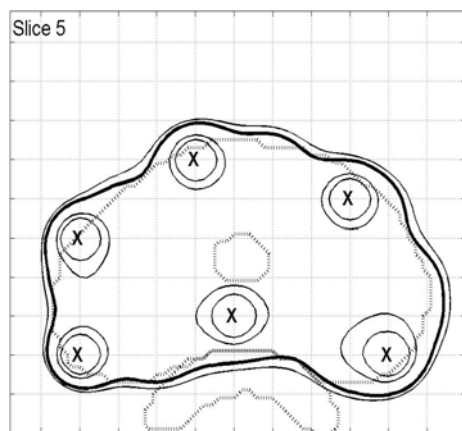
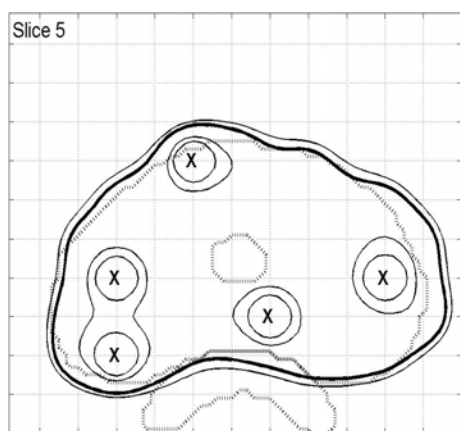
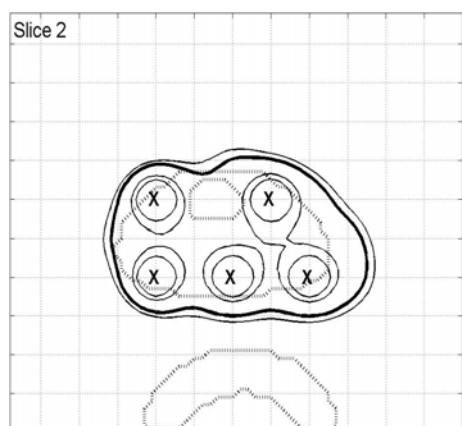
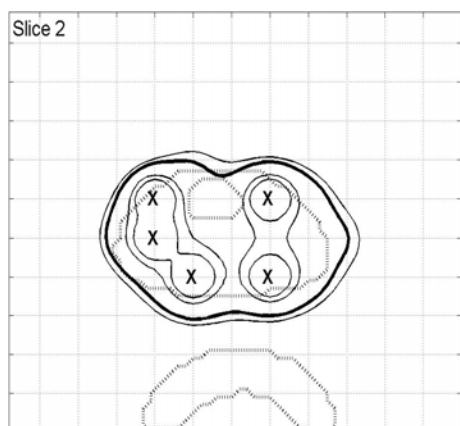
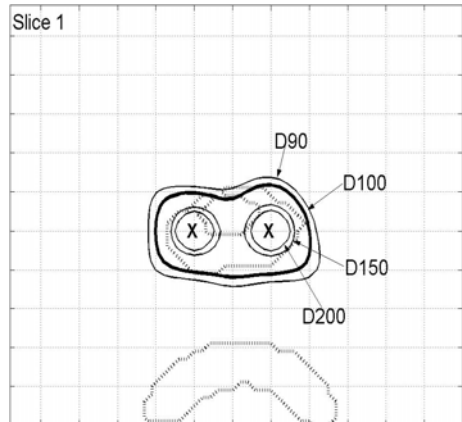
seeds, but keep in mind that this initial investigation on the use of the adjoint concept did not include a constraint to limit the number of needles.

The isodose curves and seed configurations are shown in figure 4.4. The first two, middle two and last two slices are shown. The left column is for the greedy heuristic and the right for the branch-and-bound method. The grid of possible seed positions is indicated with the 5 mm spacing lattice. The 200%, 150%, 100% (thicker line) and 90% of D_p are plotted and the ROIs are in dotted lines. A seed position is marked ‘X’. Although the seed configurations are different in detail, the D_p well covers the target volume in both cases except a few small parts. In slice 1 of the greedy heuristic result, a noticeable cold spot appears on the upper periphery where the urethra is close. Looking at slice 1 of the branch-and-bound method, we can see that the target is well covered by the D_p line. However, it is evident that the 200% isodose line covers a small part of the urethra. A feature can be compensated because one feature is satisfied. The question, whether a cold spot in the target or a hot spot in the urethra is better, will remain for a physician’s judgment.

Greedy heuristic



Branch-and-bound



(Continue)

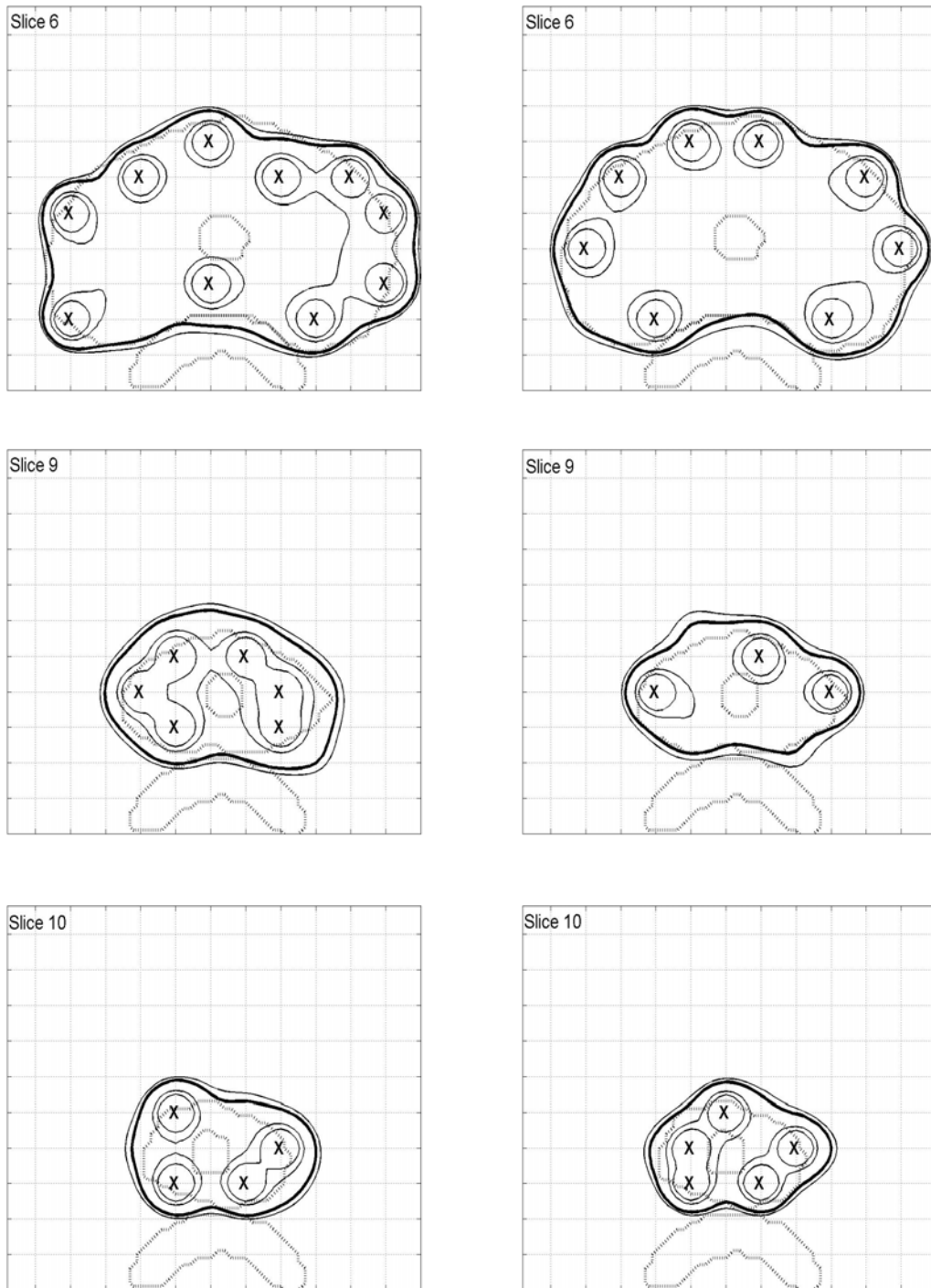


Figure 4.4 Isodose plots with the seed configurations of the greedy heuristic (left column) and the branch-and-bound method (right column). 200%, 150%, 100% (thicker line) and 90% of the prescribed dose isodose lines (solid lines) are shown with the ROIs (dotted lines). The seed placements are marked in 'X'. The first two, middle two, and last two slices are shown.

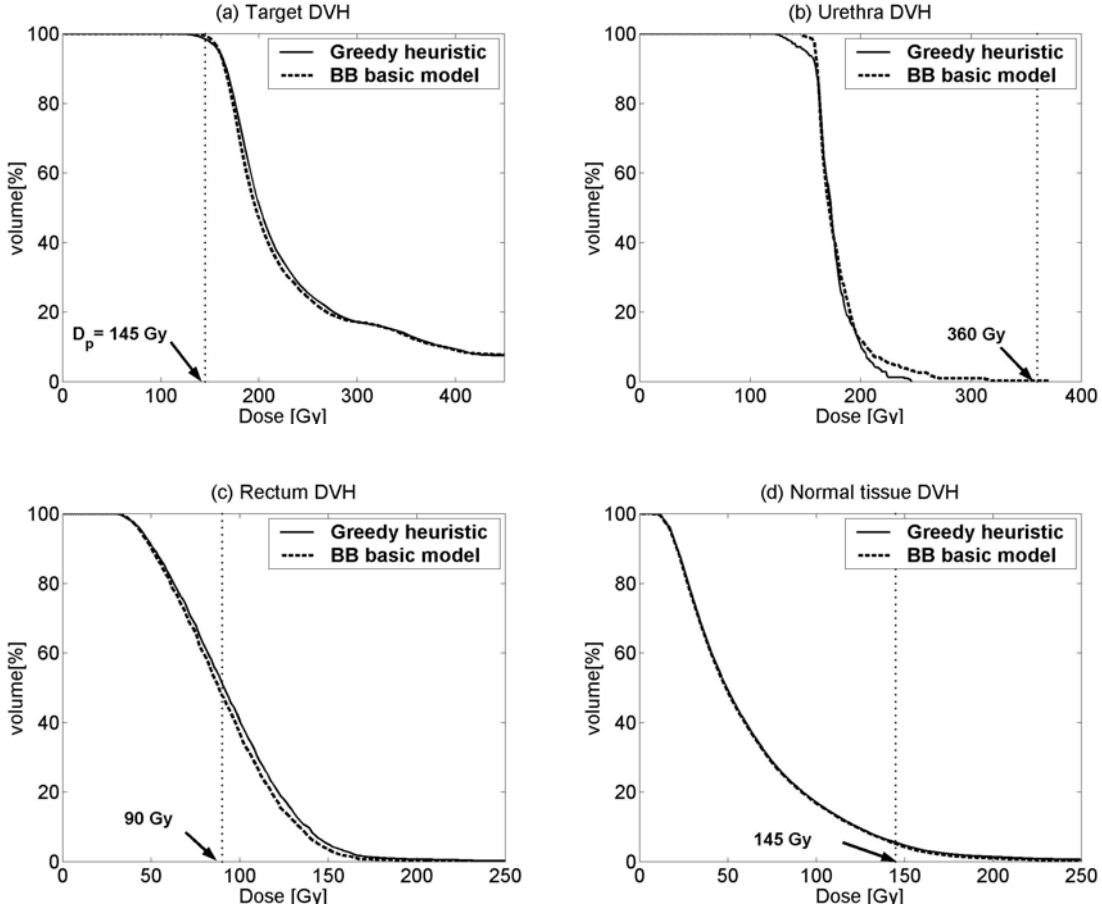


Figure 4.5 The dose-volume histogram (DVH) comparison between the greedy heuristic (solid line) and the branch-and-bound method (dashed line) for (a) target, (b) urethra, (c) rectum, and (d) normal surrounding tissue. The vertical dotted line in (a) indicates the prescribed dose 145Gy. 360Gy dose line is indicated for the urethra (b), and 90Gy for the rectum (c).

The dose-volume histogram (DVH) provides a quantitative evaluation of the treatment plan. The treatment plans obtained by the greedy heuristic and branch-and-bound are compared in DVHs shown in figure 4.5. Figure 4.5(a) is the target DVH, where the solid line and the dotted line indicate the greedy heuristic and the branch-and-bound method respectively. A couple of small differences in the target DVHs are that the DVH curve of the greedy heuristic is slightly higher in the middle range of the high dose region and a little lower at the shoulder region. For

instance, the dose deposited to 50% of the target volume, D₅₀, is 204 Gy for the greedy result but 199 Gy for the branch-and-bound result. The target coverage is 98.09 % in the greedy heuristic that is about 0.5% lower than 98.56% of the target coverage in the brach-and-bound result. Looking at the shoulder part of the target DVH in the greedy result carefully, we notice that a small fraction of the target volume is underdosed. The minimum dose in the greedy result is 124 Gy whereas it is 139 Gy for the branch-and-bound case. However, the TG64 report points out that underdosage from the D_p to the minimum dose can exceed 20%, and recommends the target coverage as a consistent indicator of implant quality [81].

The urethra DVHs, (figure 4.5(b)), show that the greedy heuristic performs a better job of sparing the urethra than the branch-and-bound method. This can be seen from the following observations: the branch-and-bound DVH has a long tail exceeding 360 Gy; the D₁₀ (dose to 10% of the urethra volume) for the greedy heuristic is about 6 Gy less than the D₁₀ for the branch-and-bound result; the D₉₀ (dose to 90% of the urethra volume) for the greedy heuristic is about 2 Gy less than the D₉₀ for the branch-and-bound result. The dotted vertical line in the plot designates the percent volume of the urethra receiving a dose greater than 360 Gy, which is indicated as U360. A maximum urethral dose above this value has been correlated with grade 2 – 3 urinary morbidity [16, 40, 69]. The greedy heuristic has zero percent of the urethra volume receiving 360 Gy whereas the branch-and-bound method has 0.32% of U360.

The rectum DVHs, (figure 4.5(c)), are very similar, but the DVH curve of the greedy heuristic is slightly higher in the high dose region. For instance, the D₁₀ for the greedy result is about 4 Gy higher and the D₉₀ is about 1 Gy higher than those for the branch-and-bound result. Thus, overall, the rectum receives a higher integrated dose in the greedy treatment plan. The dotted vertical line in the plot designates the percent volume of the rectum receiving a dose

greater than 90 Gy, which is indicated as R90. Dose to the rectum greater than this amount is correlated with rectal wall bleeding or ulceration [40, 69]. The difference in the R90 values for the greedy heuristic and the branch-and-bound method is about 4% with the greedy result having a higher value. The branch-and-bound method spares the rectum to a slightly greater degree.

The normal tissue DVHs, (figure 4.5(d)), nearly overlap, indicating that the plans have similar effects on the normal surrounding healthy tissue.

Table 4.3 Comparison of the greedy heuristic and the branch-and-bound method with the evaluation parameters.

		Greedy heuristic	Branch-and-bound
Target	V100 (%)	98.09	98.56
	V150 (%)	35.24	32.38
	DNR	0.36	0.33
	CN	0.75	0.79
	D90 (Gy)	167.28	169.05
Urethra	U360 (%)	0.00	0.32
	% volume $\geq U_{urethra}$ *	27.71	29.94
Rectum	R90 (%)	51.04	47.47
	% volume $\geq U_{rectum}$ ^	24.61	21.04
# of seeds		59	58
Time (CPU sec)		1.07	3167

* The percent volume of the urethra, which is enclosed by the $U_{urethra}$ dose. $U_{urethra}$ is set to 125% of D_p in the branch-and-bound method.

^ The percent volume of the rectum, which is enclosed by the U_{rectum} dose. U_{rectum} is set to 80% of D_p in the branch-and-bound method.

Table 4.3 summarizes a number of evaluation parameters that assess the quality of treatment plans. V100 is a measure of the target coverage [42]; it is the percent volume of the target ROI that is enclosed by at least 100% of the D_p . The V100 is 98.09% for the greedy heuristic, and 98.56% for the branch-and-bound method. The branch-and-bound method has a better target coverage. V150 is defined in a manner similar to V100, but assesses the volume of high dose regions [61]. V150 for the greedy heuristic is about 3% larger than the one for the branch-and-bound method.

D90 is defined as the dose covering 90% of the target volume. Stock *et al.* [64, 65] suggested that an adequate ^{125}I implant should deliver a dose of 140 – 160 Gy as measured by D90. Both results achieve the D90 greater than 160 Gy, but the branch-and-bound method has 2 Gy larger D90 than the greedy heuristic.

To measure the dose uniformity within the target, we used the Dose Non-uniformity Ratio (DNR) [60, 61] as following:

$$DNR = \frac{V_{150}}{V_{100}}. \quad (4.5)$$

A low DNR value means that a small fraction of the target volume is covered by a high dose, and that the dose distribution is relatively homogeneous. Uniform dose distribution through the target is desirable because uniformly distributed tumor cells throughout the target can be sterilized. Moreover, high doses within the target in excess of the desired dose level are considered to increase the risk of complication instead of being a benefit to therapy. Therefore, a lower value for DNR is favorable. The DNR, because it is the ratio of V150 to V100, ranges from 0 to 1. However, it is impossible to avoid a high dose around a seed; hence, DNR cannot be 0. Because the dose distribution around a seed spreads throughout the surrounding space, the DNR value cannot be 1. The DNR is 0.36 for the greedy plan, and 0.33 for the branch-and-bound plan,

indicating that the branch-and-bound method achieved a moderately greater degree of dose homogeneity.

The conformation number (CN) is used to assess how well the desired dose distribution conforms to the target ROI and away from health tissues. It is defined as:

$$CN = \frac{V_{target,D_p}}{V_{target}} \times \frac{V_{target,D_p}}{V_{D_p}}, \quad (4.6)$$

where V_{target} is the target volume, V_{D_p} is the volume of all tissues (including normal tissue) enclosed by the D_p that is equivalent to V100, and V_{target,D_p} is the volume of the target enclosed by the D_p [56]. The CN as found for prostate implants using ^{125}I permanent seeds averages about 0.72 [56, 81]. The CN of the greedy heuristic is 0.75 and 0.79 for the branch-and-bound method. Both methods achieved excellent target dose conformality. Yet, the branch-and-bound plan is better on this evaluation.

In the urethra evaluation, as mentioned above, U360 is the volume of the urethra enclosed by 360 Gy [16, 40, 69]. The evaluation by U360 indicates the greedy heuristic performed a better job in sparing the urethra. The percent urethra volume that receives dose greater than the upper dose constraint (% volume $\geq U_{urethra}$) represents the urethra volume with excessive urethral dose. This excessive dose contributes to the penalty in the basic MIP model for the branch-and-bound method. The greedy heuristic has 27.71% and the branch-and-bound method has 29.94%. The greedy heuristic has better urethral sparing.

For the rectum, as mentioned above, R90 is the volume of the rectum enclosed by 90 Gy [40, 69] in which the branch-and-bound performed a better job. The percent rectum volume that receives dose greater than the upper dose constraint (% volume $\geq U_{rectum}$) represents the rectum volume with excessive rectal dose. This excessive dose contributes to the penalty in the basic

MIP model for the branch-and-bound method. The greedy heuristic has 24.61% of rectum volume receiving the upper dose constraint given to the basic MIP model, and the branch-and-bound method has 21.04%. The branch-and-bound method has a better rectal sparing.

As reported earlier, the total number of seeds used is 59 for the greedy plan, and 58 for the branch-and-bound plan. One additional seed in the greedy plan contributes to the slightly higher dose in the target and the rectum.

Both methods have similar evaluation parameter values, with one method performing slightly better than the other in one category but weaker in another. Neither treatment plan can be considered superior to the other; both achieve clinically acceptable treatment plans. However, the greedy heuristic clearly out performs the branch-and-bound method in one category: the computational time consumed to arrive at a treatment plan. The greedy heuristic based on ROI adjoint functions took 1.07 CPU seconds to construct the seed configuration, while the branch-and-bound method required a minimum of about 3167 CPU seconds for a feasible solution. This difference in time expense is directly related to the fact that, unlike the branch-and-bound method, the greedy heuristic does not compute numerous trial solutions to evaluate many feasible configurations to search for the optimal solution. Previous seed selections are not modified in subsequent steps. Once a seed position is selected, it remains part of the solution space. Hence, the greedy heuristic can generate a complete solution quickly with a recipe that exploits the physical information available from the adjoint ratio.

4.4. Conclusion

We developed an efficient treatment-planning algorithm for prostate implants that is based on ROI adjoint functions implemented in a greedy heuristic. The adjoint function of a tissue ROI provides the average dose deposited in the ROI by a unit-strength source placed at any source position. The adjoint ratio combines the information from all adjoint functions into a single metric that ranks source positions in terms of their ability to deliver dose to the target while sparing critical structure ROIs. This ratio is the weighted sum of adjoint functions of critical structures divided by the adjoint function of the target. These ratio values are computed once prior to the optimization process and provide an estimate based on a physical significance for the selection of source positions. The greedy heuristic performs seed selections based on the value of the adjoint ratio for each seed position.

The treatment plan obtained with the greedy heuristic was compared with one obtained from the branch-and-bound method that solves a basic MIP model. Both methods achieved good treatment plans that satisfied the constraints for dose coverage and sparing of critical structures. However, in the terms of computation time, the greedy heuristic took 1.07 seconds while the branch-and-bound method required more than 3000 seconds. This is an improvement of a factor of more than 2500 in time expenses. We conclude that the adjoint functions and the greedy heuristic establish an efficient framework for further development of a treatment planning system.

This chapter discusses a preliminary endeavor into the use of adjoint functions in the greedy heuristic. The chapter mainly focuses on the understanding of an isodose surface constraint, which determines the search space. The resulting plans obtained by the greedy heuristic prove that the adjoint functions can be successfully applied for the optimization of

treatment planning. Moreover, the greedy heuristic using the adjoint concept performs an excellent job in saving computational time expense. The following chapters will incorporate a constraint on the number of needles (Chapter 5) and an automation of the determination and operation of isodose surface constraints (Chapter 6).

Chapter 5

Greedy heuristic for seed and needle configuration

5.1. Introduction

As previously discussed, the adjoint function of an ROI provides an intuitive means for the placement of a seed towards our optimization goal. The greedy heuristic searches a seed position based on the greedy criterion, which is the adjoint ratio. It constructs a seed configuration by selecting a seed position, which has a minimum adjoint ratio value at each step within the search space. The presentation in the previous chapter did not include an important aspect of prostate implant treatment planning, which is the number of needles.

A seed-loaded needle is inserted through the patient's perineum, and this needle insertion can induce trauma to the prostate gland and infection of the surrounding area. Also, it has been reported that needle placement uncertainty is about 5 mm longitudinally and 3 mm in transverse directions [55]. This needle displacement uncertainty directly affects displacement of seeds. Because of these two reasons, the least number of needles is desirable in prostate implants. The

results in the previous chapter used about 40 needles when a constraint on the number of needles was not included in the both models. In actual clinical treatment, prostate implants with ^{125}I seeds generally make use of less than 30 needles, depending on the target volume.

A projection of a seed configuration onto a cross-section of the prostate will represent a needle configuration; therefore, a seed configuration is two-dimensionally limited by a needle configuration. Treatment planning has to determine a seed configuration satisfying desired dose distribution as discussed in previous chapters, in addition, using a minimum number of needles as possible.

There have been some studies to develop an optimal needle pattern for prostate implants. However, most methods use either a semi-automatic process or a nomogram-style procedure based on trial-and-error experiences. Narayana *et al.* [47] investigated four needle patterns: nomogram loading, differential loading, peripheral loading, and spiked loading. It was concluded that peripheral loading with sources placed at 1-cm spacing along the needle proved to be the most effective. Butler *et al.* [8] proposed a kind of spacing strategy to modify some needle patterns, which were determined not by an optimization process but by a trail-and-error process. For instance, the suggested ‘modified uniform loading’ consists of the placement of needles and seeds on the uniform grid, followed by modification, which adds needles and seeds on the periphery and removes seeds in central needles. These adding and removing processes are performed manually until a satisfactory seed- and needle- configuration is achieved.

Thompson *et al.* [68] compared possible needle configurations, which had been established by adding or removing needles by trial-and-error process until a satisfactory pattern was achieved. Once a needle configuration was determined, a genetic algorithm optimized the seed configuration. Roy *et al.* [56] reported CT-based optimization planning, in which a needle

configuration was selected prior to the optimization process; seed loading patterns along the selected needles were determined in the optimization process. This method is semi-automatic, in that the selection of needle patterns is based on clinical judgment. The optimization strategy studied by Pouliot *et al.* [52] was similar in that a needle configuration was determined before the simulated annealing process. Yu *et al.* [81] determined a seed-loading pattern prior to the optimization of a needle configuration. The fitness function modeled by Yu *et al.* included a parameter representing the number of needles. Unlike other optimization studies, D’Souza [18] implemented a soft constraint to minimize the number of needles in his objective function.

Because of data size and computational time consideration, several of the above studies implemented semi-automatic optimization process. D’Souza whose model involves a complete automatic optimization process, investigated iteratively interacting 2-D slices to reduce the data size and computational time. As mentioned in Chapter 1, there are about 300 – 500 possible seed positions, which will involve $10^{60} – 10^{100}$ potential seed configurations for 50 – 100 seeds. Adding a needle variable will introduce 50 – 80 possible needle positions, which involve approximately $10^{25} – 10^{80}$ possible needle configurations assuming 20 needles are in use. Therefore, computational time and size almost double. If a needle configuration is predetermined, possible seed positions are constrained to the needles and computational time will be reduced. If a seed-loading pattern is predetermined, an optimization process is required to solve a needle configuration only, and then computational time will be reduced as well.

In this chapter, we include the consideration of a needle constraint in the greedy heuristic without a semi-automatic process. Two types of isodose surface constraints are introduced to restrict the search space. One constraint controls the search space until a desired number of needles are used, and works just like the one discussed in Chapter 4.2.2. The other isodose

surface constraint becomes active after a desired number of needles has been used and is applied until the termination criterion is reached. It restricts the search space along the selected needles so that a newly selected seed never requires another needle. The treatment plans solved by the greedy heuristic are compared to those by the branch-and-bound method solving a basic mixed-integer programming (MIP) model. The basic MIP model includes a hard constraint to limit the number of needles. This model is similar to D’Souza’s model in a sense that it performs a complete optimization process, but different because D’Souiza’s model included a needle constraint as a soft constraint, which is incorporated into the objective function. In addition, our model does not include any time or data reduction strategy such as iteratively interacting 2-D slices by D’souza [18] and computation for coarse resolution by Lee *et al.* [38].

5.2. Methods and Materials

5.2.1. Greedy heuristic

The following is a short recap and summary of the previous discussions and conclusions. The purpose of this study is to develop an efficient brachytherapy treatment-planning algorithm based on a greedy heuristic, which exploits the physical significance available from the ROI adjoint functions. The adjoint ratio combines the adjoint functions of all ROIs and provides an intuitive means of ranking seed positions. The greedy heuristic searches the search space for a highly ranked seed position at each step and constructs a complete seed configuration by selecting seed positions one-by-one. A highly ranked seed position is a seed position that has a minimum adjoint ratio value because it will deliver a high dose to the target, and simultaneously low doses to the

critical structures. In Chapter 4, C_{iso1}^m determined the search space, and is proportional to the number of currently selected seeds.

In this chapter, we introduce a new variable to represent needles and use two isodose surface constraints. A seed position within the search space, determined by one constraint, is continuously selected at each step until the preset number of needles is reached. Thereafter, the other isodose surface constraint, together with the needle configuration, restricts the search space for further selections of seed positions.

This greedy heuristic process for prostate implant treatment planning with the needle constraint is illustrated with details in the following pseudo-code:

Initialization.

Empty seed configuration; $Q^0 = \emptyset$,

empty needle configuration; $N^0 = \emptyset$,

all seed positions within the target \in search space; $\forall j \in X^0$, where $j \in \text{target}$,

and 1st step; $m=1$

Step m.

If the current number of needles $< C_{needle}$,

search space X^m satisfies $D_{XQ^{m-1}}^{m-1} \leq C_{iso1}^m$.

Otherwise, (if the current number of needles $= C_{needle}$),

search space X^m is restricted to within N and satisfies $D_{XQ^{m-1}}^{m-1} \leq C_{iso2}^m$.

If $X^m = \emptyset$, reset one of C_{iso1}^m , C_{iso2}^m , or C_{needle} , and starts from initialization.

Otherwise, select j^m minimizing $R(j)$, where $j^m \in X^m$

$$Q^m = Q^{m-1} \cup j^m, N^m = N^{m-1} \cup j^m, \text{ and } D_{iQ^m}^m = D_{iQ^{m-1}}^{m-1} + D_{ij^m}, \forall i \in \text{target}.$$

If target coverage $\geq C_{coverage}$, stop. Q^m is a greedy solution.

Otherwise, $m \leftarrow m + 1$. (5.1)

The heuristic initializes a seed configuration, Q , to an empty set, a needle configuration, N , to an empty set and the search space, X , to the whole target ROI. At the beginning of the search, the search space consists of all possible seed positions that have not yet been selected within the target ROI. The greedy heuristic searches X for a seed position, j , that has the minimum $R(j)$ among all possible seed positions in the search space. The selected seed position, j , is included in the seed configuration, Q , and a needle to carry this seed is included in the needle configuration, N , and the dose distribution, D , is computed. If the j is in a needle that has been added in a previous step, N does not get updated. If the resulting dose distribution accomplishes the target coverage greater than $C_{coverage}$, the process terminates and the current seed configuration is a greedy solution. Otherwise, it moves onto the next step. In the case of an empty search space, a user should reset C_{isol}^m , C_{iso2} , or C_{needle} , and start from the initialization. Table 5.1 lists new parameters used in this chapter and their definitions. Definitions of other parameters were listed in table 4.1.

Table 5.1 Definition of parameters in the pseudo-code 5.1

Parameters	Details
N	Needle configuration that consists of needles to load selected seed positions.
N^0	Initial needle configuration, which is empty.
N^m	Needle configuration at the m^{th} step.
X^m	Search space at the m^{th} step. An area enclosed by the isodose surface C_{iso1}^m within the target ROI, or by C_{iso2} along needles in N .
C_{iso1}^m	Isodose surface constraint 1 at the m^{th} step. The superscript ‘ m ’ indicate the step order.
C_{iso2}	Isodose surface constraint 2.
C_{needle}	Needle constraint. It is a user-defined desired number of needles.

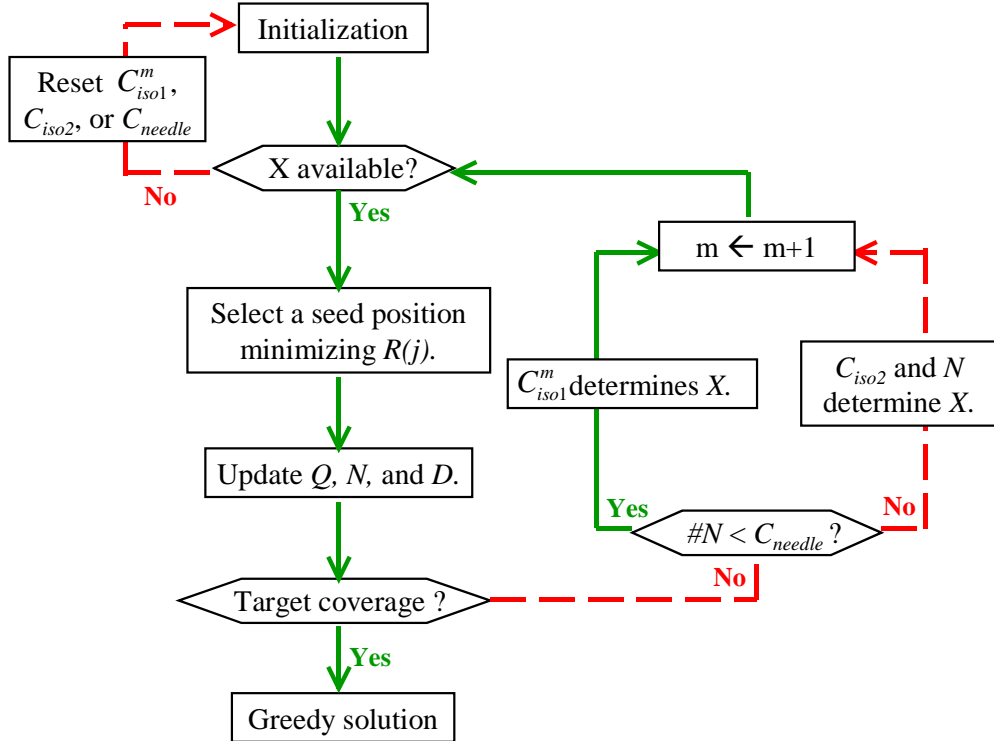


Figure 5.1 Flowchart of greedy heuristic for the optimization of a seed and needle configuration

This optimization process is simplified in the flowchart shown in figure 5-1. Starting with initialization, if the search space, X , is “available”, a seed position, j , that has a minimum adjoint ratio value, $R(j)$, is selected. If X is “not available”, a user should reset one of C_{iso1}^m , C_{iso2} and C_{needle} . C_{iso1}^m and C_{iso2} are two different types of isodose surface constrains, which are used in different situations (see Chapter 5.2.2). When there is at least one possible seed position that has not been selected yet, the search space is “available”. When there is no possible seed position within the search space, the search space is “not available”.

After a selection is made, Q , N and D are updated. If the target coverage reaches its termination criterion, $C_{coverage}$ (see Chapter 4.2.3), Q becomes a greedy solution. Otherwise, the

current number of needles, $\#N$, is compared to C_{needle} . If $\#N$ is less than C_{needle} , C_{iso1}^m determines X . If $\#N$ is not less than, in other words, if it is equal to, C_{needle} , C_{iso2} and N determine X . $\#N$ cannot exceed this C_{needle} value. This process continues adding a seed position onto the seed configuration until the termination criterion is reached.

5.2.2. Selection of constraints

Isodose surface constraint 1: C_{iso1}^m

The isodose surface constraint, C_{iso1}^m , determines the search space, X . It works like the isodose surface constraint C_{iso}^m discussed in Chapter 4.2.2. However, C_{iso1}^m is valid from the first step in the process until the number of needles reaches C_{needle} . It has the superscript ‘ m ’ because its value changes proportionally as the step order. C_{iso1}^m is expressed as equation 4.3.

In the first step ($m=1$), the search space includes all possible seed positions in the target, and the greedy heuristic selects a seed position that has a minimum adjoint ratio. The first selected seed is added onto the empty seed configuration and requires a needle, which is added onto the empty needle configuration. The search space is restricted again within the target but this time excluding a region enclosed by C_{iso1}^2 . This excluded region receives a dose greater than C_{iso1}^2 . In the second step ($m=2$), another selected seed is added onto the seed configuration. If the second selected seed position requires a new needle, a needle is added onto the needle configuration; if the second seed position shares the same needle with the first seed, the needle configuration doesn’t get updated. This process repeats until the number of needles in the needle

configuration reaches C_{needle} . Hence, C_{iso1}^m is applied to regulate the spacing of the needle arrangement by controlling the search space for seeds.

As discussed in Chapter 4.2.2, as C_{iso1}^m decreases, the volume enclosed by this isodose surface increases. The resulting search space will include a fewer number of possible seed positions. As long as there is a possible seed position in the search space, the smallest possible value for C_{iso1}^m is desirable in order to attain better homogeneous dose distribution within the target. In Chapter 4.2.2, the C_{iso}^m value was selected based on the minimum average dose delivered to the entire target by a single seed, which was 1.48% of the prescribed dose, D_p , for the example patient. The C_{iso}^m value was set to 1.77% of the prescribed dose, D_p following examinations of increasing α values from 1.48% (see Chapter 4.2.2). The reason we didn't decrease α was that 1.48% was so small that the search space ran out of possible seed positions before the termination of the process. However, for the work covered in this chapter, C_{iso1}^m is active only until C_{needle} is reached, and seeds used up to this point will be fewer than the number of seeds required for the entire process. Because C_{iso1}^m can be set smaller than what it was in Chapter 4, we examine decreasing α values from 1.48% in this chapter. Table 5.2 lists the C_{iso1}^m values used for this study.

Isodose surface constraint 2: C_{iso2}

The isodose surface constraint, C_{iso2} , determines the search space, X . It works similar to C_{iso1}^m as discussed in figure 4.2, but has different features. C_{iso2} is used after the preset number of needles is reached. The search space is restricted within the target simultaneously to the needle

configuration determined in the previous steps. Now the search space includes possible seed positions only along the selected needles, excluding the area enclosed by C_{iso2} . The area enclosed by C_{iso2} refers to the area where the dose deposition is higher than C_{iso2} .

After a complete needle configuration is reached, C_{iso2} and the needle configuration control the search space. A seed position is still selected based on the greedy criterion, which is the adjoint ratio. Since the needle pattern has been determined already, the following process focuses on a seed loading pattern along the needles. Along the selected needles, a seed position, around which insufficient dose has been delivered and has a minimum adjoint ratio value, would be favorable for a seed placement. The dose value to judge, how much is insufficient and how much is sufficient, is applied to C_{iso2} .

We initially guessed a C_{iso2} value as being 100% of D_p . Seed positions around which the dose deposition is less than D_p are included in the search space, if they appear along the selected needles. Some periphery voxels of the target might not be close to any of the needles, and these voxels will not receive sufficient dose (D_p), even if other voxels around the needles receive sufficient dose (D_p). Therefore, the C_{iso2} value should be higher than 100% of D_p to cover the target sufficiently. We examined increasing values for C_{iso2} until a satisfactory solution was achieved. Table 5.2 lists the C_{iso2} values used for this study.

Needle constraint: C_{needle}

C_{needle} represents the desired number of needles. The greedy heuristic adds a seed position that requires a new needle at each step. This seed position is selected within the search space restricted by C_{iso1}^m . As a new needle is introduced, the number of needles in the needle

configuration increases. Note that it is possible that the seed position appears along a needle that has been selected in a previous step. When the number of needles reaches C_{needle} , the search space is no longer restricted by C_{iso1}^m ; now C_{iso2} and the needle configuration determine the search space.

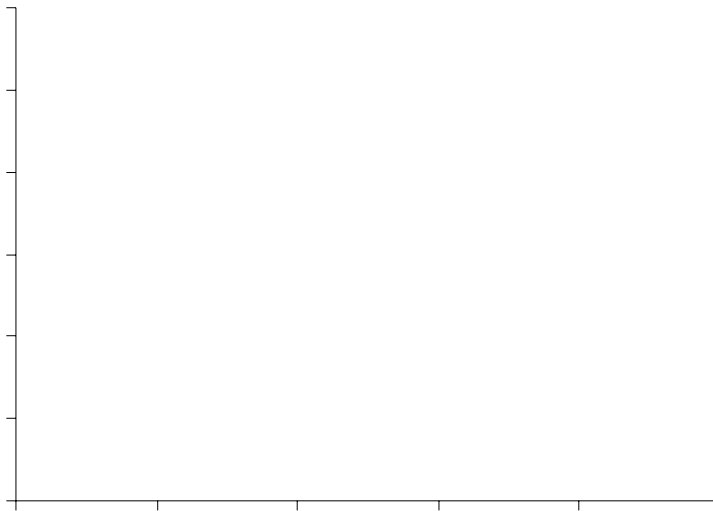


Figure 5.2 A plot of the number of needles used in 48 treatment plans versus the target volume. $y = 0.24x + 11.33$ is a fit function to the data. (Courtesy of Heath Odau in UWCCC)

A user should preset a C_{needle} value based on clinical experience. The data of 49 patients who received prostate ^{125}I permanent seed implant treatment in last two years (2001 – 2002) in the department of human oncology at the University of Wisconsin Comprehensive Cancer Center (UWCCC) were analyzed. The relationship between the target volume and the number of needles used in each treatment plan was plotted in figure 5.2, and a fit function was drawn. These plans

were given 150 Gy for the prescribed dose and used 0.43 mCi of permanent ^{125}I seeds. This function fit shown in equation 5.2, was used to estimate the number of needles for the example patient in this study. Table 5.2 lists the C_{needle} values used for this study.

$$y = 0.24 * x + 11.33, \quad (5.2)$$

where x is the target volume in cc and y is the number of needles.

Termination criterion: $C_{coverage}$

The greedy heuristic terminates its process when the termination criterion is reached. The termination criterion is, as explained in Chapter 4.2.3, that the target coverage should be greater than $C_{coverage}$, which is preset by a user. This study, this value is initially set to 98%. Table 5.2 lists $C_{coverage}$ values used for this study.

5.2.3. Branch-and-bound including a hard constraint for the number of needles

The basic mixed-integer programming model for prostate implants was introduced in Chapter 4.2.4. We add a hard constraint of the number of needles used. The constraint is expressed as:

$$\sum_n N_n \leq U_{needle}$$

If $\forall x_j = 0$ for $j \in n$, $N_n = 0$.

If $\exists x_j = 1$ for $j \in n$, $N_n = 1$. (5.3)

where n indicates a needle position and N_n represents a needle placement/non-placement (1/0) at n . If all seed placements are zero in n , in other words, if there is no seed placed along n , the

needle variable N_n becomes zero. If any seed placement is one along n , N_n becomes one. The upper needle constraint, U_{needle} , is a user-set value, which is based on clinical judgment. We estimate a U_{needle} value using the fit function in figure 5.2.

5.3. Results and discussion

The same patient geometry (33.06cc) as described in chapter 4 is used for this study. Table 5.2 lists all constraint values including U_{needle} used in this study. We test the greedy heuristic in three cases with different numbers of needles. Branch-and-bound is used for comparison, and is tested with the same needle constraint value. Other constraint values are selected based on trial and error until a satisfactory solution is achieved. For Case I, we tested 98% for $C_{coverage}$ and found that the result showed undesirable homogeneous dose distribution. Thus, the $C_{coverage}$ value for Case I was set to 95%.

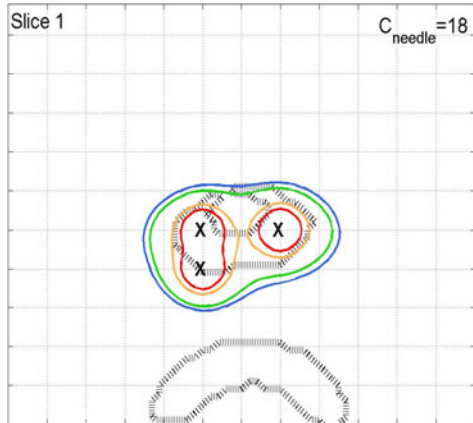
Table 5.2 Constraint values

	Greedy heuristic				Basic model
	C_{needle}	α (for C_{iso1}^m)	C_{iso2}	$C_{coverage}$	U_{needle}
Case I	18	1.2% of D_p	112% of D_p	95%	18
Case II	20	1.3% of D_p	108% of D_p	98%	20
Case III	22	1.3% of D_p	105% of D_p	98%	22

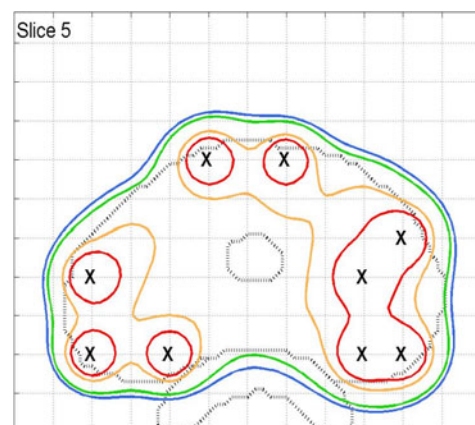
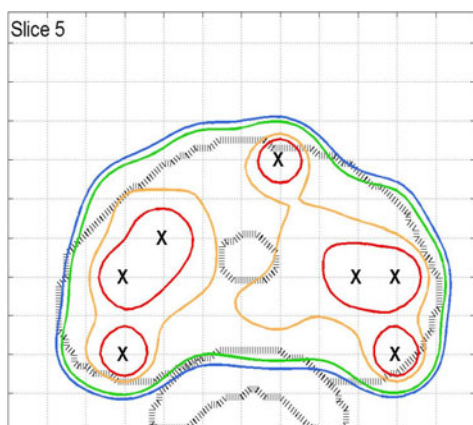
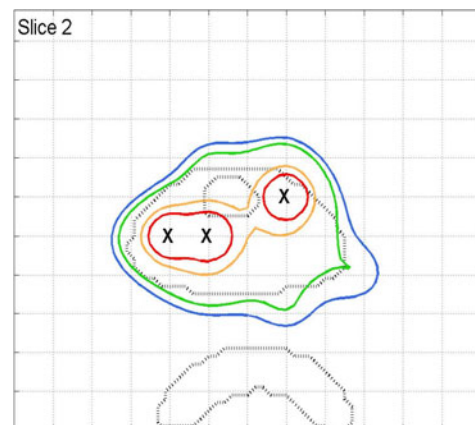
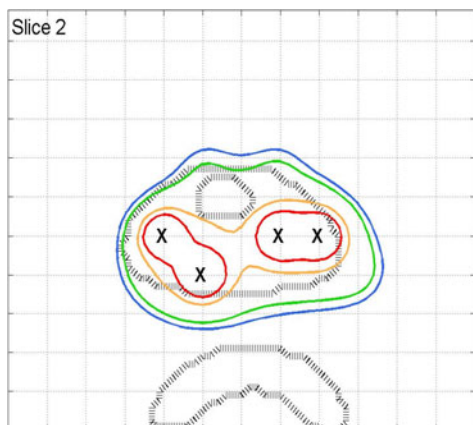
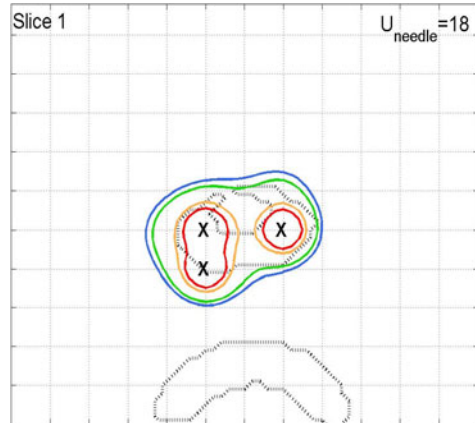
The isodose curves and seed configurations of the greedy heuristic and the branch-and-bound method are compared in figure 5.3. The first two slices (slice 1 and 2), middle two (slice 5

and 6) and last two (slice 9 and 10) are shown with seed placements marked ‘X’. The 200%, 150%, 100% and 90% of D_p are plotted in red, yellow, green and blue respectively. ROIs are in dotted lines. The grid of possible seed positions is indicated with the 5 mm lattice spacing. This figure is for Case I, which has the number of needles limited to 18. Because the termination criterion for the greedy heuristic was set to 95% of the target coverage, some areas not enclosed by the prescribed dose line appear here and there. The target dose seems more conformal in the branch-and-bound method, but the urethra and the rectum are spared better in the greedy heuristic. The quantitative comparison is shown in figure 5.4 and the numerical evaluation is in table 5.3.

Greedy heuristic



Branch-and-bound



(Continue)

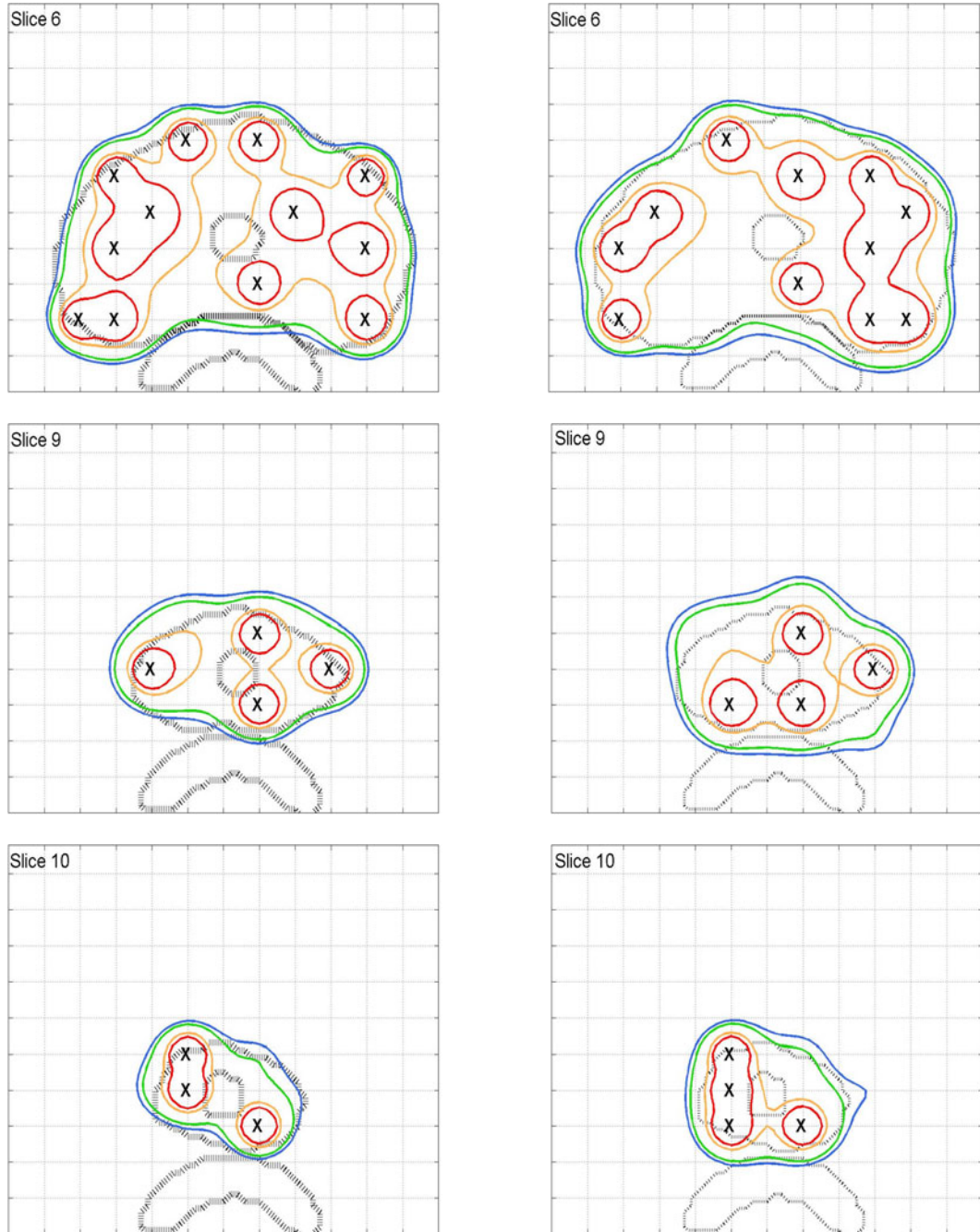


Figure 5.3 Isodose plots with the seed configurations of the greedy heuristic (left column) and the branch-and-bound method (right column) for Case I ($C_{needle}=18$ and $U_{needle}=18$). 200% (red), 150% (yellow), 100% (green) and 90% (blue) of the prescribed dose isodose lines are shown with the ROIs (dotted lines). The seed placements are marked in 'X'. The first two, middle two, and last two slices are shown.

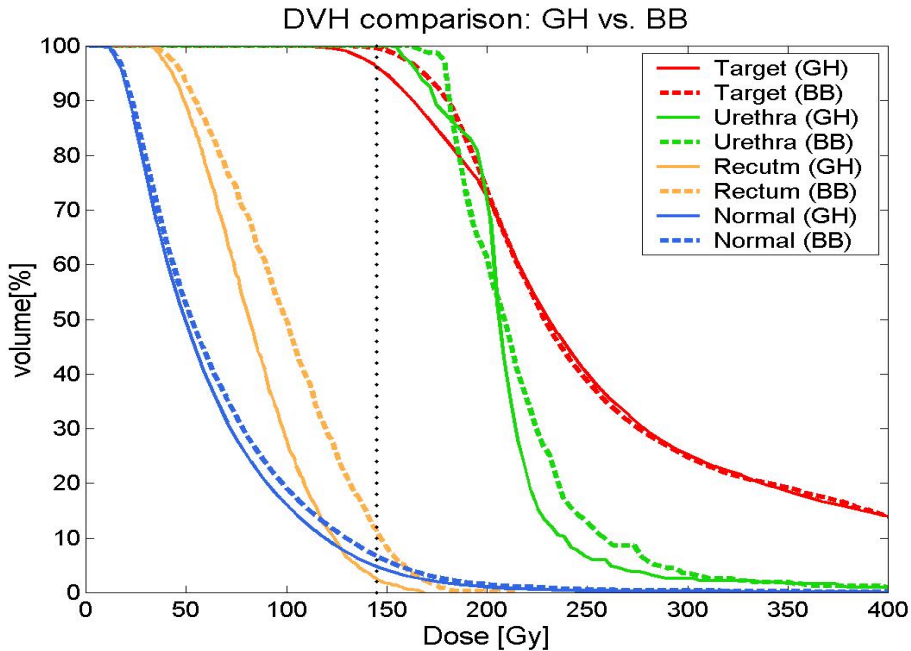


Figure 5.4 Dose-volume histogram (DVH) comparison between the greedy heuristic (GH) and the branch-and-bound method (BB) for Case I. Cneedle=18 and Uneedle=18. The dotted horizontal line is the line for the prescribed dose, which is 145 Gy.

The treatment plans for Case I are compared in the dose-volume histograms shown in figure 5.4. The solid lines are for the greedy heuristic, and dashed lines for the branch-and-bound. The target is in red, urethra in green, rectum in yellow, and normal surround tissue in blue. Because $C_{coverage}$ in the greedy heuristic for Case I was set to 95% of the target coverage, the shoulder part of the target DVH in the greedy heuristic result shows about 5% gap between the DVH curve and the ceiling. The urethra (green) DVHs intersect one another twice; once around 170 Gy, and once around 200 Gy. The shoulder part of the urethra DVH by the greedy heuristic is lower than the one by branch-and-bound; this means a large portion of the urethra receives smaller dose (< 170 Gy) in the greedy heuristic plan than in the branch-and-bound plan. Looking at the high dose region (> 200 Gy), we can note that the larger volume of the urethra receives a higher dose for the branch-and-bound plan than the plan by the greedy heuristic. The rectum receives

larger dose in the plan by branch-and-bound than the one by the greedy heuristic. Normal tissue DVHs are just slightly different; the greedy heuristic spares the normal tissue slightly more.

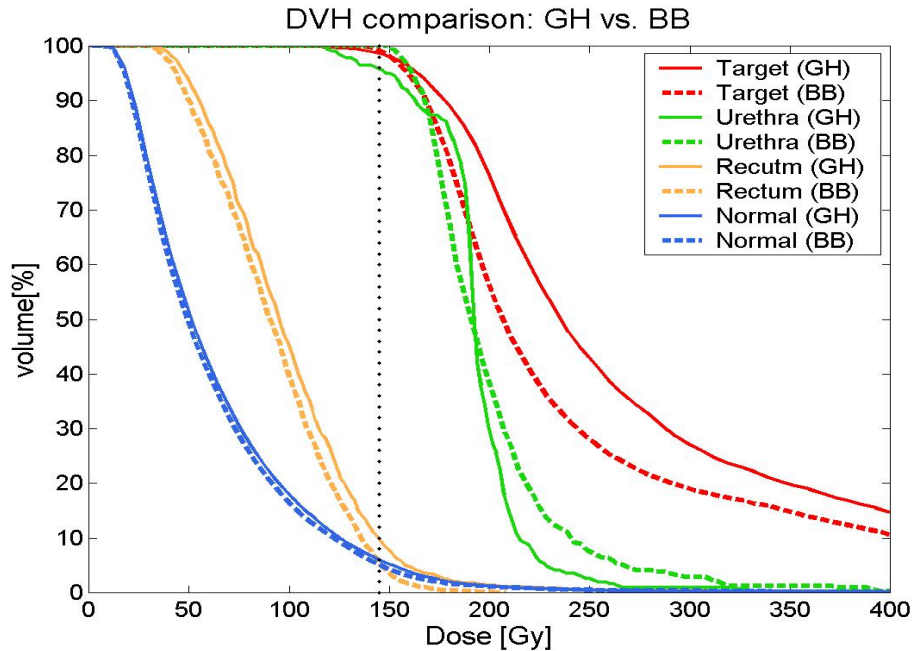


Figure 5.5 Dose-volume histogram (DVH) comparison between the greedy heuristic (GH) and the branch-and-bound method (BB) for Case II. Cneedle=20 and Uneedle=20. The dotted horizontal line is the line for the prescribed dose, which is 145 Gy.

Figure 5.5 compares the DVHs for the greedy heuristic and the branch-and-bound method for Case II, which used 20 needles. The shoulder parts in the target DVHs show that the branch-and-bound line is over the greedy heuristic line, which means the branch-and-bound result conforms better to the target than the greedy heuristic result. The body part of the target DVH by branch-and-bound drops off more rapidly than the one for the greedy heuristic. This swift drop-off represents a more homogeneous dose distribution within the target. The urethra DVHs have the same tendency as in Case I (figure 5.4). The shoulder parts of the urethra DVHs show that the

large volume in the greedy heuristic receives smaller dose (< 170 Gy) than in branch-and-bound. The tail parts of the urethra DVHs in the high dose region (> 200 Gy) show that a larger volume receives high dose in branch-and-bound than in the greedy heuristic. Branch-and-bound performs a slightly better job of sparing the rectum than the greedy heuristic. The normal tissue DVHs almost overlap.

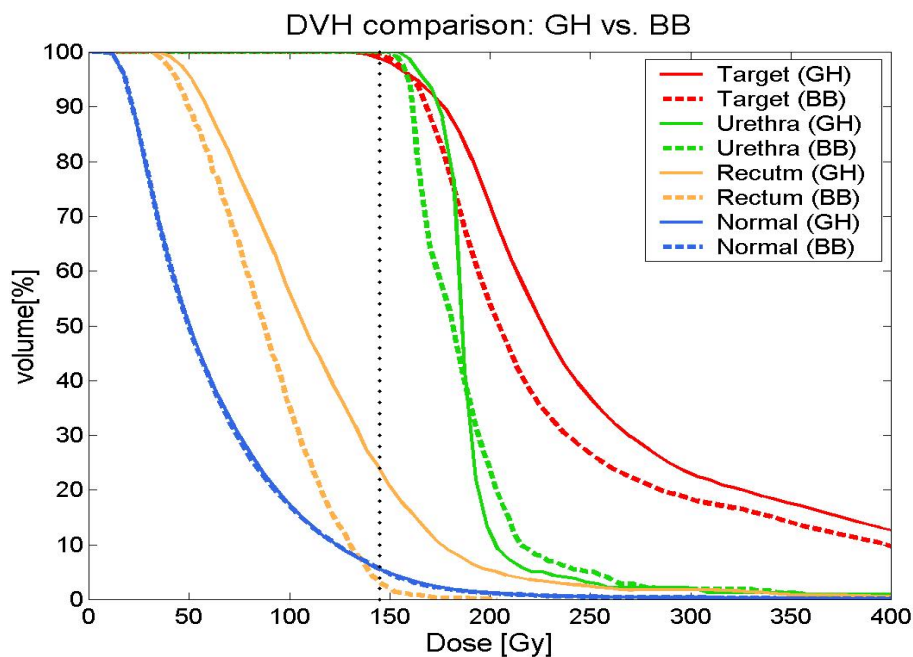


Figure 5.6 Dose-volume histogram (DVH) comparison between the greedy heuristic (GH) and the branch-and-bound method (BB) for Case III. Cneedle=22 and Uneedle=22. The dotted horizontal line is the line for the prescribed dose, which is 145 Gy.

Figure 5.6 compares the DVHs by the greedy heuristic and branch-and-bound of Case III, which use 22 needles. The shoulder parts in the target DVHs show that the branch-and-bound line is over the greedy heuristic line, which means the branch-and-bound result covers the target

slightly better than the greedy heuristic. The body part of the target DVH by branch-and-bound drops off more rapidly than the one by the greedy heuristic. This swift drop-off represents a more homogeneous dose distribution within the target. The urethra DVHs intersect one another around the 170 Gy region. The shoulder part of the urethra DVHs show that the large volume receives smaller dose (< 170 Gy) in the branch-and-bound than in the greedy heuristic. The tail part shows that a larger volume receives higher dose (> 170 Gy) in the greedy heuristic than in the branch-and-bound method. As more needles are used, the urethra receives a lower dose. The branch-and-bound performs a better job of sparing the rectum than the greedy heuristic. The normal tissue DVHs almost overlap.

The comparisons for the three cases of results are listed in table 5.3 with numerical parameters that assess the quality of treatment plans. As we set the termination criterion to 95% of the target coverage for Case I in the greedy heuristic, the V100 (percent volume of the target enclosed by 100% of the prescribed dose line) [42] is 95.15%, which is the lowest among other V100s. Other V100s are greater than 98%. V150 (percent volume of the target enclosed by 150% of the prescribed dose) [61] indicates a high dose volume. The V150 of branch-and-bound is smaller than the one of the greedy heuristic except for Case I, where they are only 0.14% different. D90 is higher for all cases in both methods than the range (140 – 160 Gy) suggested by Stock *et al.* [64, 65].

The dose non-uniformity ratio (DNR) [60, 61] was lower in branch-and-bound than for the greedy heuristic in Chapter 4 without a needle constraint. The studies with the needle constraint also show a better dose uniformity in the branch-and-bound method than in the greedy heuristic. Especially, the greedy heuristic for Case II has a high DNR, which could be noticed in the large gap between two target DVHs in figure 5.5. The greedy heuristic of Case III also has high DNR.

Overall, the branch-and-bound performs a better job in uniformly distributing dose in the target than the greedy heuristic.

Table 5.3 Comparison of the greedy heuristic (GH) and the branch-and-bound (BB) method with the evaluation parameters.

		Target						
		V100 (%)	V150 (%)	D90 (Gy)	DNR	CN		
Case I	GH	95.15	55.46	163.32	0.58	0.76		
	BB	99.23	55.60	181.92	0.56	0.74		
Case II	GH	98.52	60.33	179.59	0.61	0.73		
	BB	98.61	39.29	172.97	0.40	0.77		
Case III	GH	98.29	51.88	177.67	0.53	0.75		
	BB	99.36	39.10	169.88	0.39	0.75		
		Urethra	Rectum		# of seeds	# of needles	Time	
		U360 (%)	% Volume $\geq U_{\text{urethra}}$	R90 (%)	% Volume $\geq U_{\text{rectum}}$		(CPU sec)	
Case I	GH	1.59	86.62	38.38	14.03	60	18	1.78
	BB	1.27	87.26	59.29	32.21	64	18	8163
Case II	GH	0.32	82.80	54.35	28.83	63	20	1.64
	BB	1.27	60.19	49.48	23.12	59	20	7210
Case III	GH	0.96	7675	63.18	39.68	62	22	1.60
	BB	0.64	47.13	45.52	19.48	59	22	8172

The conformation numbers (CN) [56, 81] are over 0.72 for all cases, and branch-and-bound and the greedy heuristic are competitive in CNs. As explained in Chapter 4, the higher CN the better conformal dose within the target. For Case I, the greedy heuristic has a higher CN value, but for Case II, the branch-and-bound method has a higher CN. They have the same CN values for Case III.

U_{360} (the urethral volume enclosed by 360 Gy) [16, 40, 69] is very low for all cases. The percent urethra volume that receives dose greater than the upper dose constraint (% volume $\geq U_{urethra}$) is the smallest for branch-and-bound of Case III. Even this smallest value is much higher than the one in chapter 4. As the number of needles is limited, the urethral dose increases. In Case I, the greedy heuristic has a smaller urethral volume, which receives dose greater than the $U_{urethra}$ value, than branch-and-bound. In Case II and III, branch-and-bound has smaller values than the greedy heuristic. Overall by this evaluation, branch-and-bound performs a better job in sparing the urethra than the greedy heuristic. However, we saw that the opposite for the DVHs (figure 5.4. 5.5. and 5.6). $U_{urethra}$ is about 180Gy over which the crossovers appear in the DVHs. The DVHs of branch-and-bound look better in the dose range around 180Gy.

R_{90} measures the rectal volume enclosed by the 90Gy isodose line [40, 69]. For Case I, the greedy heuristic has a smaller R_{90} than branch-and-bound, but for Case II and Case III, the branch-and-bound has a smaller R_{90} than the greedy heuristic. The percent rectum volume that receives dose greater than the upper dose constraint (% volume $\geq U_{rectum}$) is smaller for the greedy heuristic than branch-and-bound for Case I. This value is higher for the greedy heuristic than the branch-and-bound for Case II and Case III.

The greedy heuristic uses 4 less seeds in Case I, 4 more seeds in Case II, and 3 more seeds in Case III than branch-and-bound, respectively. In Case I, the target coverage is set to 95%,

which is lower than other cases, thus a smaller number of seeds is required. In Case II and Case III, the greater number of seeds results in larger high dose region within the target, thus the DNR for the greedy heuristic is higher than branch-and-bound.

Overall in most categories, the branch-and-bound results appear to be superior except in the urethra DVH evaluation. Especially, a branch-and-bound result shows high quality evaluations in the dose distribution in the target, such as the target coverage (V100), and the dose uniformity (DNR). However, the dose distribution in the target by the greedy heuristic seems acceptable as a treatment plan. Moreover, the computational time spent by the greedy heuristic is less than 2 CPU seconds whereas the time required to achieve a feasible solution by branch-and-bound is about 8000 CPU seconds, which is over two hours. The greedy heuristic including the needle constraint criterion is about 4000 times more efficient in time expense than the branch-and-bound method.

5.4. Conclusion

The greedy heuristic search strategy used in this chapter is similar to Chapter 4. The greedy heuristic searches the search space for a seed position based on the adjoint ratio, and constructs a seed configuration adding seed positions one-by-one. Additionally, this chapter introduces the needle constraint and focuses on its implementation. Two types of isodose surface constraints were used to determine the search space in different situations: C_{iso1}^m and C_{iso2} . As seed positions are selected one-by-one within the search space restricted by C_{iso1}^m , the number of needles increases as well. When it reaches to the preset needle constraint value, C_{iso2} and the selected

needles limit the search space so that no more new needles are used even if a seed position is continuously selected.

We tested three cases with the needle constraint values of 18, 20 and 22. These needle constraint values were chosen based on the relationship between the target volume and the number of needles used in the treatment plans at UWCCC. All other constraints were chosen after many trials. The C_{isol}^m was based on the minimum average dose delivered by a unit-source to the entire target, and the C_{iso2} was based on the desired dose level that is the prescribed dose. For comparison, the branch-and-bound method was used with the hard constraint to limit the number of needles.

The numerical evaluations measuring the quality of the treatment plans show that the branch-and-bound method performed a better job in more categories. However, the urethra DVHs demonstrate that the greedy heuristic performs a better job in sparing the urethra than the branch-and-bound method. A major feature we should point out is the computational time, since the purpose of this study is to develop an efficient optimization algorithm. The computational time required for the branch-and-bound method using the needle constraint is more than twice as long as the one without the needle constraint. The computation took more than two hours. On the other hand, the greedy heuristic took only about 2 seconds, which is considerably shorter. Even with the needle constraint, the required time is close to the time spent in Chapter 4 because this additional constraint does not involve extra computation. The greedy heuristic performs the same computation whether with or without the needle constraint. The only different procedure is that the search space is restricted along the needles. Therefore, the time required in the greedy heuristic with the needle constraint is still very short.

In this study, we tested different combinations of constraint values until a satisfying solution was achieved. Although one successful process took about 2 seconds, it was not guaranteed to find a good combination of constraint values quickly. The next chapter will discuss a methodology to automate the search of finding a successful combination of constraint values for the greedy heuristic. Because one trial in the greedy heuristic takes a couple of seconds, it is expected that many consecutive trials with different combinations of constraint values could be evaluated in a reasonable time.

Chapter 6

Greedy heuristic with an automatic selection of the constraint values

6.1. Introduction

In Chapter 5, we implemented a needle constraint to limit the number of needles. An isodose surface constraint determined the search space depending on the situation. We tested combinations of all constraint values by trial-and-error until a satisfactory solution was achieved. Three different combinations of the constraint values were applied to the greedy heuristic and compared to the branch-and-bound results. Although we estimated an approximate range of each constraint value, a best combination for all constraint values was unknown unless it had been examined. The selection of constraint values by trial-and-error poses a challenge, as it can be a labor intensive and tedious task.

For a case where constraints are related to the dose distribution such as our basic mixed-integer programming model, those constraint values are based on the desired dose level for each

ROI. In our greedy heuristic model the isodose constraints are not directly related to the desired dose level, thus it is not easy to guess a good combination. Moreover, if an isodose surface constraint value is low so that a large area is excluded from the search space, there can be no possible seed position for a next step. Each time this instance occurs, a user should reset the isodose surface constraint value.

As shown in the previous chapters, the greedy heuristic based on the adjoint ratio takes only a couple of seconds to find a seed configuration. Hundreds of trials would take less than 10 minutes. Unlike the trial-and-error selection process for the constraint values used in Chapter 5, in this chapter we implement an automatic scanning of constraint values in the greedy heuristic. A combination of all constraint values is selected automatically within preset ranges, and the greedy heuristic constructs a seed configuration. This process continues until a successful seed configuration is constructed with the least possible number of needles.

6.2. Methods and Materials

6.2.1. Greedy heuristic

This chapter extends the presentation from Chapter 5. The greedy heuristic, as discussed in Chapter 4 and Chapter 5, searches the search space for a seed position, which has a minimum adjoint ratio. The search space is determined by an isodose surface constraint, which is proportional to the number of current seeds. As seed positions are added to the seed configuration one-by-one, the number of needles increases. When the number of needles reaches a desired

number of needles, a different isodose surface constraint and the needle configuration restrict the search space. The greedy heuristic keeps adding seeds until the termination criterion is reached.

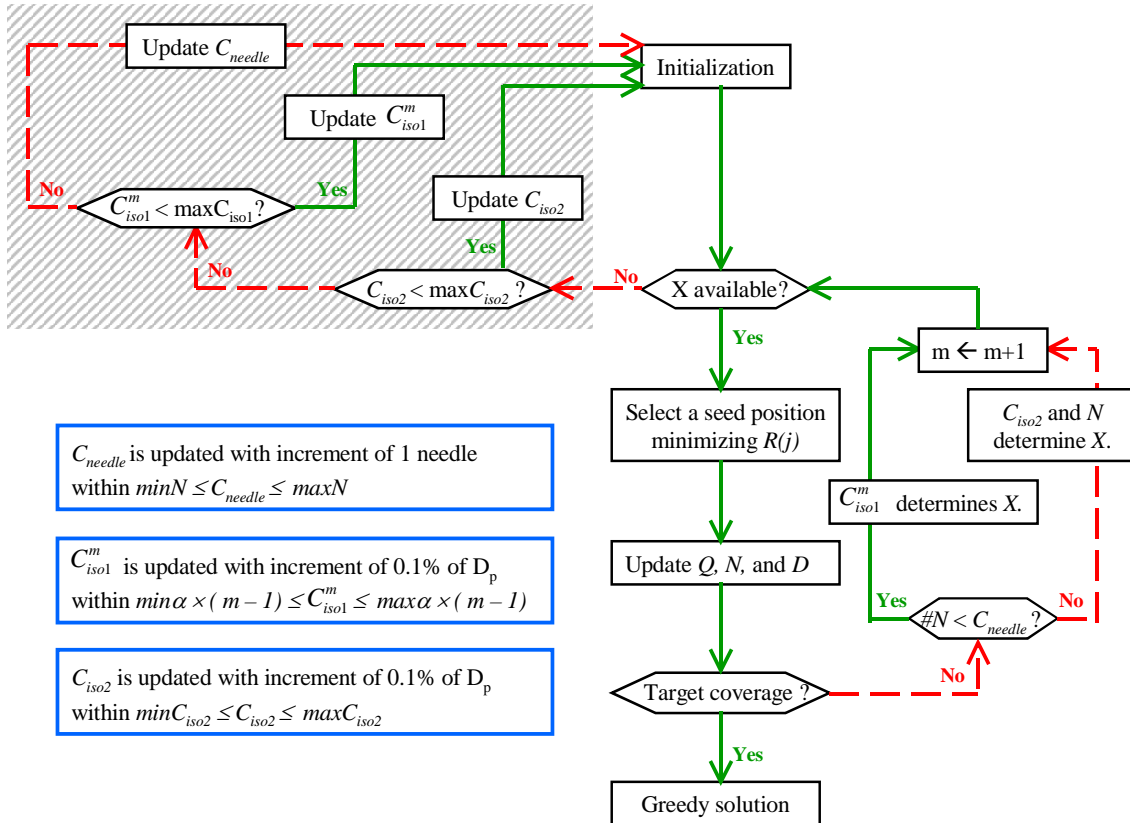


Figure 6.1 Flowchart of greedy heuristic

The process described in Chapter 5 required a user to manually set the constraint values prior to the optimization process. As explained in the flowchart 5.1 and the pseudo-code 5.1, a user has to reset one constraint value if there is no seed position available in the search space before a successful seed configuration has been made. We found, through trial-and-error

experience, a good combination of all constraint values that achieved a satisfactory treatment plan. However this manual trial-and-error process is tedious and labor intensive. We know an approximate range for each constraint based on its characteristic, and we know that one trial of the greedy heuristic takes about a second. Hence a procedure is developed to automate the scanning process of many trials with possible combinations of constraint values.

Figure 6.1 shows the flowchart of the automatic process for the selection of the constraint values in the greedy heuristic. This automatic process is indicated in the gray box, which highlights changes to the process of Chapter 5. The greedy heuristic starts with the initialization of a seed configuration, Q , a needle configuration, N , the dose distribution, D , the search space, X , the step order, m , and the initial values of C_{needle} , C_{iso1}^m and C_{iso2} . The initial seed configuration is set to empty; $Q = \emptyset$, and the initial needle configuration is also set to empty; $N = \emptyset$. Therefore, the initial dose distribution is zero; $D = 0$. At the first step ($m = 1$), the initial values of the constraints are $C_{needle} = \min N$, $C_{iso1}^m = \min \alpha \times (m - 1)$, and $C_{iso2} = \min C_{iso2}$. These initial values are the lower bounds of the constraint ranges. How to determine the ranges will be discussed with the characteristics of constraints in an upcoming section.

The search space includes all possible seed positions within the target at the first step. If the search space is “available”, that is if there are possible seed positions in the search space, the greedy heuristic selects a seed position that has a minimum adjoint ratio. This selected seed position is added onto the seed configuration. It also contributes to the needle configuration if an additional needle is required. The dose distribution is computed with this seed configuration. If the target coverage with the resulting dose distribution satisfies the termination criterion, the current seed- and needle- configuration becomes a greedy solution. Otherwise, it checks the current number of needles in use, $\#N$. If $\#N$ is smaller than C_{needle} , C_{iso1}^m determines the search

space. Otherwise, if $\#N$ is equal to C_{needle} , C_{iso2} and the current needle configuration determine the search space. Then the step number increases. This process continues adding seed positions onto the seed configuration one-by-one until the termination criterion is met or until the search space doesn't include any possible seed position.

If the search space is “not available”, in other words if the search space includes no possible seed position, the C_{iso2} value is updated first. However, if C_{iso2} has reached its upper bound, $maxC_{iso2}$, but if C_{iso1}^m has not reached its upper bound, then, C_{iso1}^m value is update. Each time C_{iso1}^m is updated, C_{iso2} is re-initialized to its lower bound, $minC_{iso2}$. When the C_{iso1}^m value reaches its upper bound, $max\alpha \times (m - 1)$, C_{needle} is updated and C_{iso1}^m is re-initialized to its lower bound, $min\alpha \times (m - 1)$. Each time C_{needle} is updated, C_{iso1}^m is re-initialized to its lower bound. If both C_{iso1}^m and C_{iso2} have reached their upper bounds, the C_{needle} value is updated, and C_{iso1}^m and C_{iso2} are re-initialized to their lower bounds. Following this procedure, the greedy heuristic terminates when a successful seed configuration is reached. Therefore, the number of needles will be as low as possible, and C_{iso1}^m and C_{iso2} will be smallest possible.

6.2.2. Selection of ranges for constraints

Isodose surface constraint 1: C_{iso1}^m

Isodose surface constraint 1, C_{iso1}^m , determines the search space from the first step till the number of needles used reaches C_{needle} . C_{iso1}^m is updated when the search space doesn't have a possible seed position for the next step. It starts from $min\alpha \times (m - 1)$ and is updated with an increment of

0.1% of D_p . An upper bound of the C_{iso1}^m range is set so that the process does not enter into an infinite loop. The upper bound of the C_{iso1}^m range is expressed as $\max\alpha \times (m - 1)$, where $\max\alpha$ is set to the minimum average dose delivered to the entire target volume by a unit source. This $\max\alpha$ varies with the target volume, which is patient-dependant.

Note that a smaller C_{iso1}^m value is preferable in order to prevent seeds and needles from being selected too close to one another. However, the C_{iso1}^m value should be large enough to allow possible seed positions in the search space. C_{iso1}^m is updated starting from the lowest value. Once a successful seed configuration is obtained, the procedure terminates. The smallest value that can provide a successful seed configuration will be the best value for C_{iso1}^m .

Isodose surface constraint 2: C_{iso2}

Isodose surface constraint 2, C_{iso2} , determines the search space after the number of needles used reaches C_{needle} until the termination of the process. Seed positions within the target along the selected needles, but excluding the area enclosed by C_{iso2} , are included in the search space. C_{iso2} is updated when the search space does not have a possible seed position for the next selection and when the termination criterion has not yet been achieved. It starts from $\min C_{iso2}$ and is updated with an increment of 0.1% of D_p up to $\max C_{iso2}$.

The idea behind of C_{iso2} is simple. Now that the search space is restricted to the needle configuration, a seed position that is located in a low dose area along the needles should be selected. An area enclosed by C_{iso2} is excluded from the search space because this area receives a high dose. The dose level to judge a low dose or a high dose is applied to C_{iso2} , which is based on D_p . In order to cover the target sufficiently, C_{iso2} should be set high. Conversely, in order to

prevent seeds from being selected too close to one another, C_{iso2} should be set low. The range for C_{iso2} is shown in table 6-1.

C_{iso2} is updated starting from the lowest value with the increment of 0.1% of D_p . Once a successful seed configuration is accomplished the process is terminated. A successful seed configuration refers to the one that has achieved the termination criterion. The smallest value that can provide a successful seed configuration will be the best value for C_{iso2} .

Needle constraint: C_{needle}

As the greedy heuristic adds seed positions onto the seed configuration one-by-one during the initial seed selection process, the number of needles in the needle configuration increases. During this process, C_{iso1}^m determines the search space. When the number of needles reaches C_{needle} , the needle configuration and C_{iso2} determine the search space. The greedy heuristic contributes to add seed positions to the seed configuration. However, the number of needles and the needle configuration are not changed.

As in Chapter 5, we estimate the desired number of needles according to the function fit (equation 5.2) obtained by the patient data. C_{needle} starts from the lower bound in the range, $\min C_{needle}$, which is set to two less needles than the function fit value. When there are no more seed positions available in the search space, C_{iso1}^m or C_{iso2} is updated and re-initialized. If C_{iso1}^m and C_{iso2} reach their upper bounds in their ranges, C_{needle} is updated with an increment of one needle. We expect that the greedy heuristic will construct a successful seed configuration before C_{needle} reaches its maximum value, $\max C_{needle}$, which is set unrealistically high. Table 6.1 lists ranges for the constraint values. C_{iso1}^m , C_{iso2} and C_{needle} .

Table 6.1 Ranges for the constraint values

	Lower bound	Upper bound	Increment [♦]
C_{iso1}^m	$0.1\% \times D_p \times (m - 1)$	(Minimum average dose to the entire target by a single source) [♣] $\times (m - 1)$	$0.1\% \times D_p$
C_{iso2}	$100\% \times D_p$	$108\% \times D_p$	$0.1\% \times D_p$
C_{needle}	$(0.24 \times V_{target} + 11.33)^{\ddagger} - 2$	30	1 needle

^{*} The fit function of the plot for the relationship between the target volume (V_{target}) and the number of needles used.

[♣] This is computed for each patient because it depends on the target volume.

[♦] Increment with which a constraint value is updated in the process.

Termination criterion: $C_{coverage}$

The greedy heuristic terminates when the termination criterion is satisfied. The termination criterion for this study is, as in Chapter 4.2.3, that the target coverage should be greater than $C_{coverage}$. We set $C_{coverage}$ to 98% of the target volume. Therefore, a seed configuration that results in the target coverage greater than 98% of the target volume will be taken for a successful solution.

6.2.3. Branch-and-bound including a constraint of the number of needles in the objective function

The basic mixed-integer programming model for prostate implants was introduced in Chapter 4.2.4. We add a parameter for the number of needles in the objective function expressed as;

$$\begin{aligned} \text{minimize } & \sum_{ROI} \sum_{i \in ROI} (w_{ROI} \cdot z_i) + w_{needle} \sum_n N_n \\ \text{subject to } & N_n \in \{0, 1\} \end{aligned} \quad (6.1)$$

where n indicates a needle position and the binary variable N_n represents a needle placement/non-placement (1/0) at n . The w_{needle} is a needle weighting parameter, which should be a user-set value. Several values have been examined for w_{needle} by trial-and-error. The most satisfying result was achieved when w_{needle} was set to 10. A hard constraint was imposed over the number of needles so that the number of needles never exceeded the hard constraint value in the basic MIP model in Chapter 5. This model, however, includes the needle constraint in the objective function, which is called a soft constraint. The soft constraint controls the number of needles incorporated in the objective function. As w_{needle} increases, the resulting number of needles decreases. A user should make a decision for w_{needle} value after several trials. At the beginning, we used 1 for w_{needle} , and the result showed a large number of needles. We tested increasing w_{needle} values up to 20. It was found that increasing w_{needle} from 10 to 15 reduced the number of needles by one or two, but sacrificed the dose distribution in critical structures. We decided to fix the value of w_{needle} to 10.

As mentioned in Chapter 5, introducing a set of needle variables involves an increasing number of equations and variables in the computation. For the example patient used in Chapter 4 and Chapter 5, the discrete variables representing seed placements or needle placements became 10 times larger and the number of equations to be solved became almost doubled due to the introduction of the needle variable. As a result, the branch-and-bound method in Chapter 4 without a needle variable required about 3000 CPU seconds, whereas in Chapter 5 it required about 8000 CPU seconds to obtain a feasible solution.

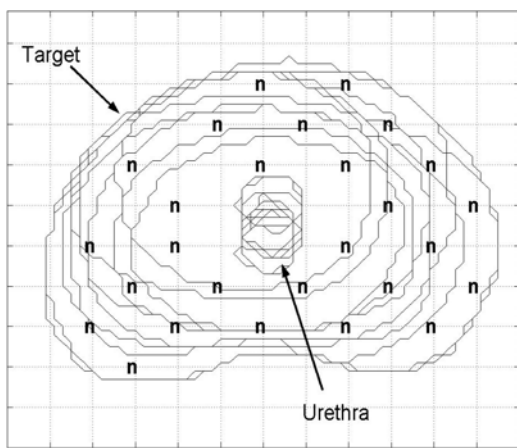


Figure 6.2 The predetermined needle configuration for patient J. The prostate images consist of 11 slices, which are projected on to one plane. The target and urethra are contoured and the needle positions are marked ‘n’.

We tested 10 patients among which two patients (patient I and patient J) had relatively large target volumes. The GAMS system in our current computer system did not complete the computation for these two patients due to memory size. For these two patient cases, we manually determined a needle configuration [68]. The optimization process determined a seed-loading pattern using the preset needle configuration. As suggested by other studies in

arrangement of needles [8, 47, 68], we tried to form peripheral loading with spacing greater than 0.5 cm. However, the needle configurations for patient I and J appear more like uniform loading due to the small target cross-sections in the base and apex slices. We used the same number of needles obtained by the greedy heuristic. Figure 6.2 shows the needle configuration for patient J.

All other constraint values were set as shown in table 4.2. The hard constraint over the target, $\min D_{target}$, was set to 90% of the prescribed dose except for the patients with large target

volume sizes (patient I and patient J). Probably because of the predetermined needle configurations in patient I and patient J, 90% of the prescribed dose for $\min D_{target}$ resulted in unsatisfying homogeneous dose distribution. For those two patients, $\min D_{target}$ was set to 80% of the prescribed dose.

6.3. Results and discussion

As discussed in Chapter 4.2.5, the greedy heuristic was processed in the MATLAB environment. GAMS with CPLEX solver was used for the branch-and-bound method solving the basic MIP model. All computations were performed with a Compaq Alpha 667 MHz computer. We performed the greedy heuristic and the branch-and-bound method on 10 prostate implant patients. All conditions were the same as in the previous chapters.

Table 6.2 lists the constraint values, which produce a successful seed configuration in the greedy heuristic. The three constraint values for each patient are the smallest possible values to achieve the termination criterion. The smallest target volume is 25.49 cc and the largest target volume is 52.68 cc in this study.

There is a rough tendency that the C_{needle} value is large for a large target, and the C_{iso1}^m value is small for a large target. C_{iso1}^m determines the search space for seed selections, which determine a needle configuration. Thus, C_{iso1}^m contributes to the establishment of the needle configuration. C_{iso1}^m indirectly and C_{needle} directly control the number of needles, which is related to the target volume. It is shown that C_{needle} increases and C_{iso1}^m decreases with the target volume. However, the C_{iso2} value doesn't have a tendency related to the target volume.

The C_{iso2} value for each patient does not show a correlation with the target volume or the number of needles used. However, the resulting dose distribution is influenced mostly by C_{iso2} . The C_{iso2} values for patients B, C and G are lower than for other patients. Looking at figure 6.3, the target DVH lines of the greedy heuristic falloff more rapidly for patient B, C and G than for other patients.

Table 6.2 Automatically selected constraint values, which produce a seed configuration successfully in the greedy heuristic for 10 patients.

Patient	V_{target} [cc]	C_{needle}	$C_{iso1}^m [\times D_p \times (m - 1) \text{ Gy}]$	$C_{iso2} [\times D_p \text{ Gy}]$
A	33.06	20	1.3%	108.0%
B	30.42	19	1.6%	103.4%
C	25.49	17	1.7%	102.0%
D	29.92	23	1.7%	105.0%
E	34.25	23	1.4%	107.4%
F	36.89	20	1.4%	107.8%
G	31.47	20	1.4%	101.8%
H	36.79	21	1.4%	105.9%
I*	40.33	22	1.1%	107.2%
J*	52.68	27	1.0%	105.9%

* In the equation 4.4, the hard constraint ($D_{i \in target} \geq minD_{target}$) to restrict the minimum dose to the target in the branch-and-bound method was set to 80% of the prescribed dose ($minD_{target} = 80\% \text{ of } D_p$) for patient I and patient J.

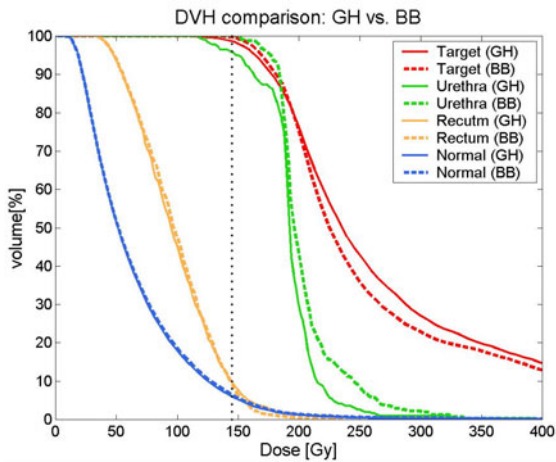


Figure 6.3(a) Patient A

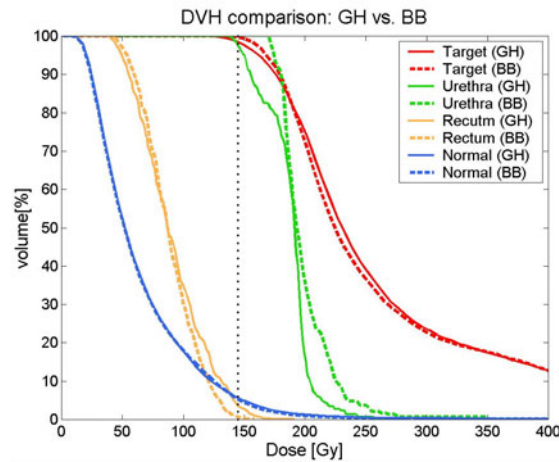


Figure 6.3(b) Patient B

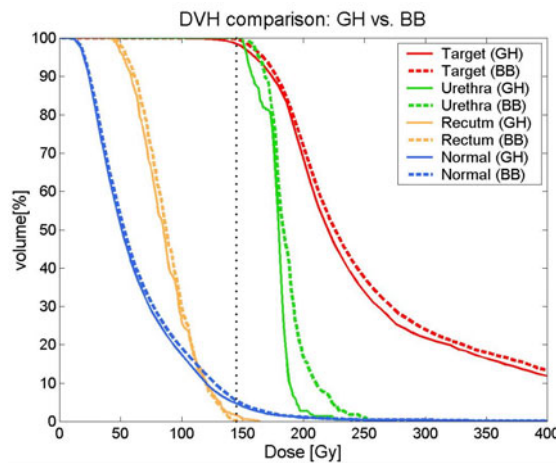


Figure 6.3(c) Patient C

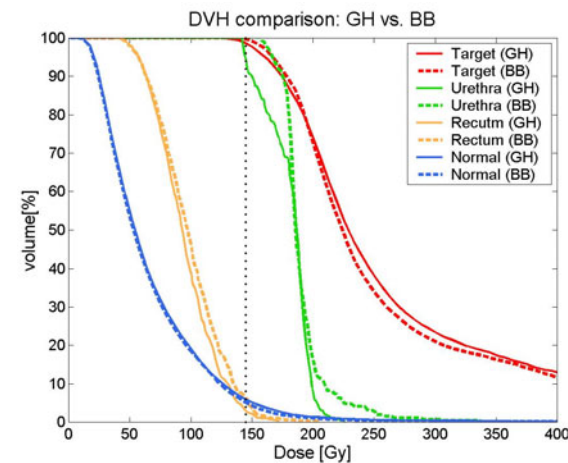


Figure 6.3(d) Patient D

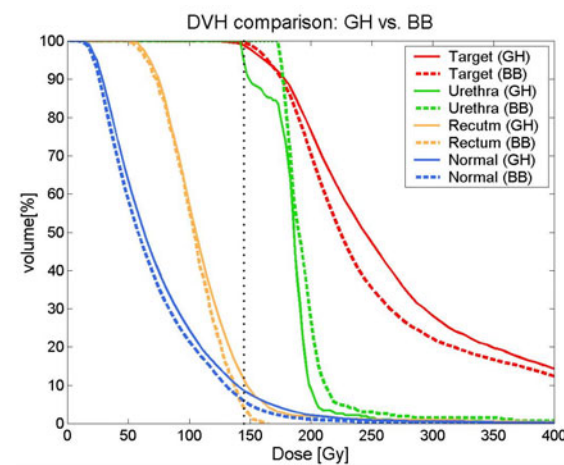


Figure 6.3(e) Patient E

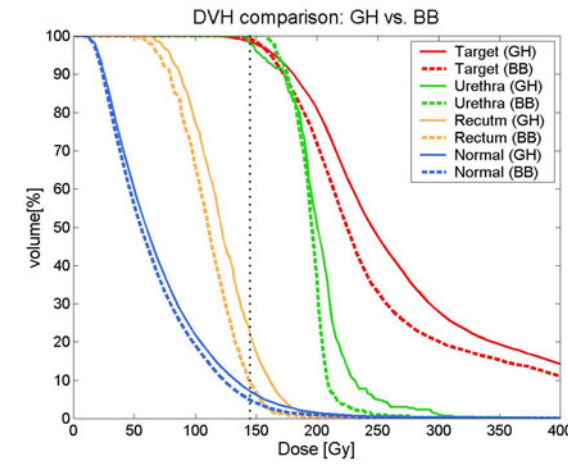


Figure 6.3(f) Patient F

(continued)

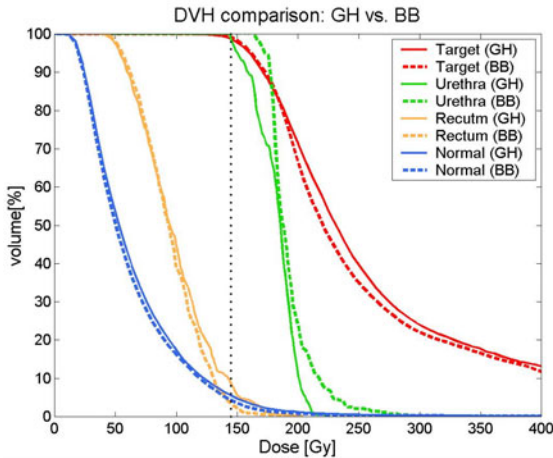


Figure 6.3(g) Patient G

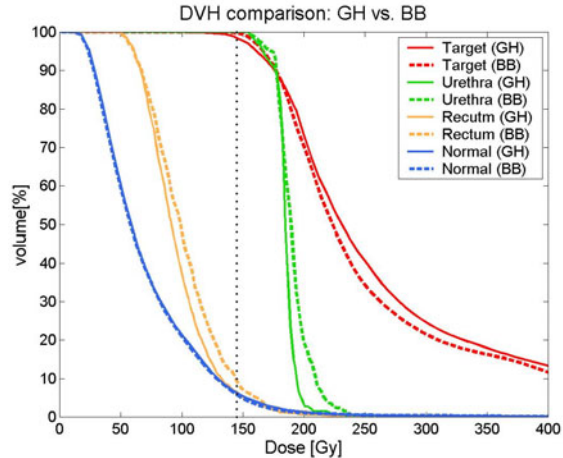


Figure 6.3(h) Patient H

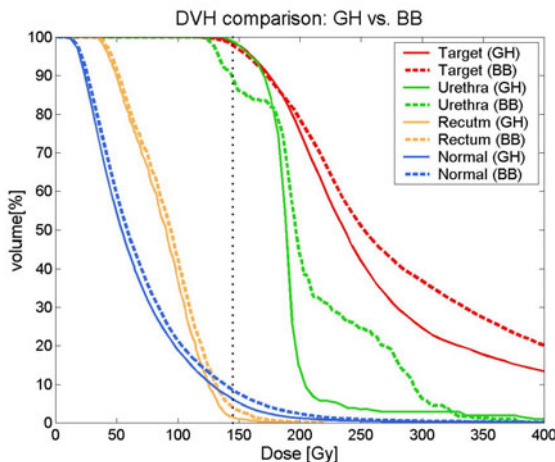


Figure 6.3(i) Patient I

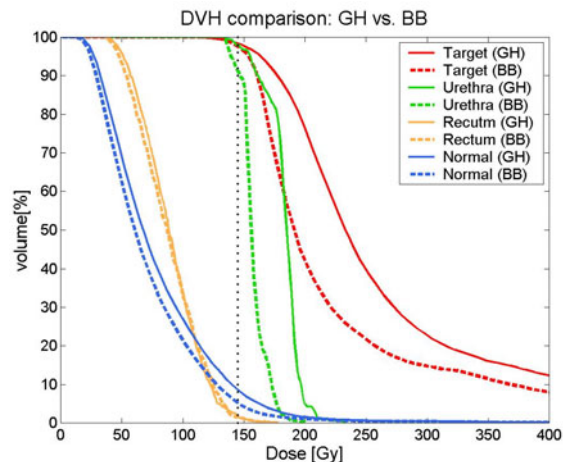


Figure 6.3(j) Patient J

Figure 6.3 A comparison of dose-volume histograms (DVH) between the greedy heuristic (GH) in solid lines and the branch-and-bound method (BB) in dashed lines. Figures (a) to (j) correspond to Patient A to J. Red lines are for the target DVHs, green lines for the urethra DVHs, yellow lines for the rectum DVHs and blue lines for the normal surrounding tissue. (larger figures are attached in Appendix A)

The shoulder parts of the target DVHs (red) by the greedy heuristic in patients A to H show that a small area in the target is underdosed. The target DVH lines of the greedy heuristic are slightly lower around the shoulder part than those of the branch-and-bound method. However, the target DVH lines of the greedy heuristic around the middle part (dose range between 200 - 350 Gy) are higher than those of the branch-and-bound method. This lower target DVH lines of the branch-and-bound method around the dose range 200 and 350 Gy indicate improved dose homogeneity within the target. The exception to this was patient I. The target DVH by the branch-and-bound method in patient I does not show a good homogeneous dose distribution. This may be because the predetermined needle configuration was not fine enough. When we tested the basic model for patient I with 90% of D_p for the $\min D_{target}$ value, the target DVH showed a worse dose homogeneity. Thus, we set $\min D_{target}$ to 80% of D_p . For the same reason in patient J, we set $\min D_{target}$ to 80% of D_p . The target DVH by the branch-and-bound method for patient J with 80% of D_p of $\min D_{target}$ shows a good homogeneous dose distribution.

The urethra DVHs (green) for most patients prove that the greedy heuristic tends to spare the urethra to a better degree. The shoulder parts of DVHs where the large percentage of the urethra volume and the dose around 150Gy cross show that the urethra receives less dose by the greedy heuristic than by the branch-and-bound method. This feature occurs for all patients except patient I and patient J. The end parts of DVHs where the 40% of the urethra volume and the dose greater than 200 Gy cross show that the urethra has a lower degree of overdose by the greedy heuristic than by the branch-and-bound method for most patients. This feature occurs in the opposite way in patient F and patient J. The urethra DVH of patient I has an irregular shape, which may be a result of using the predetermined needle configuration.

The rectum DVHs (yellow) by the greedy heuristic and by the branch-and-bound method are quite similar. The end parts of the rectum DVHs in patients D and I by the greedy heuristic are lower than those by the branch-and-bound method; the greedy heuristic performed a better job in sparing the rectum in patients D and I. This occurs in the opposite way in patients B, E and G where the branch-and-bound method performed a better job in sparing the rectum. The branch-and-bound method has a overall lower rectum DVH line in patient F, and the greedy heuristic has a overall lower rectum DVH line in patient H.

The DVH lines for the normal surrounding tissue almost overlap for all patients.

Table 6.3 presents a comparison of various evaluation parameters as computed by the greedy heuristic (GH) and the branch-and-bound (BB) method.

Table 6.3 Comparison of various evaluation parameters as computed by the greedy heuristic (GH) and the branch-and-bound (BB) method for patients A to J.

		A	B	C	D	E
Target						
V _{target} (cc)		33.06	30.42	25.49	29.92	34.35
V100 (%)	GH	98.23	98.09	98.06	98.23	98.32
	BB	99.62	99.19	99.74	99.50	98.88
V150 (%)	GH	60.33	57.94	51.06	57.46	61.97
	BB	56.17	53.24	53.32	51.31	53.17
D90 (Gy)	GH	179.59	176.13	179.97	175.42	182.62
	BB	185.68	182.56	183.04	179.06	182.26
DNR	GH	0.61	0.59	0.52	0.58	0.63
	BB	0.56	0.54	0.53	0.52	0.54
CN	GH	0.73	0.70	0.59	0.65	0.62
	BB	0.73	0.79	0.77	0.79	0.81
Urethra						
U360 (%)	GH	0.32	0.00	0.00	0.00	0.37
	BB	0.32	0.00	0.00	0.00	1.12
%Volume $\geq U_{\text{urethra}}$ *	GH	82.80	73.06	34.55	62.22	63.94
	BB	92.40	84.18	51.82	73.33	72.86
Rectum						
R90	GH	54.35	46.95	38.81	54.93	70.56
	BB	58.05	43.38	45.30	58.21	70.44
%Volume $\geq U_{\text{rectum}}$ *	GH	28.83	20.57	12.29	20.39	32.48
	BB	30.26	13.34	13.26	25.48	31.19
# of seeds	GH	63	57	48	56	65
	BB	63	57	50	55	61
# of needles	GH	20	19	17	23	23
	BB	22	20	18	19	19
Time (CPU second)	GH	54	38	18	59	46
	BB	8166	8094	8055	8084	8108

(table 6.3 continued)		F	G	H	I*	J*
Target						
V _{target} (cc)		36.89	31.47	36.47	40.33	52.68
V100 (%)	GH	98.13	98.20	98.04	98.04	98.08
	BB	98.55	98.59	99.39	97.64	97.23
V150 (%)	GH	67.54	57.79	57.99	58.56	60.42
	BB	54.97	48.09	52.23	66.30	30.35
D90 (Gy)	GH	186.38	174.31	180.12	177.01	180.78
	BB	175.02	173.84	182.47	173.56	165.27
DNR	GH	0.69	0.59	0.59	0.60	0.62
	BB	0.56	0.49	0.53	0.68	0.31
CN	GH	0.68	0.70	0.70	0.85	0.83
	BB	0.82	0.81	0.81	0.70	0.81
Urethra						
U360 (%)	GH	0.34	0.00	0.00	1.91	0.00
	BB	0.00	0.00	0.00	0.96	0.00
% Volume ≥ U _{urethra} *	GH	82.65	61.81	74.11	74.84	62.25
	BB	82.65	71.18	75.89	78.66	2.00
Rectum						
R90 (%)	GH	86.44	54.66	51.52	50.39	47.96
	BB	76.63	54.15	58.28	53.96	44.88
% Volume ≥ U _{rectum} *	GH	57.82	25.79	19.29	17.66	14.60
	BB	40.10	22.42	28.48	22.14	16.68
# of seeds	GH	68	58	65	79	85
	BB	63	56	64	76	75
# of needles	GH	20	20	21	22	27
	BB	20	17	23	22	27
Time (CPU second)	GH	30	52	36	54	87
	BB	8129	8099	8137	2289	7143

* The percent volume of the urethra, which is enclosed by the U_{urethra} dose. U_{urethra} is set to 125% of D_p in the branch-and-bound method.

* The percent volume of the rectum, which is enclosed by the U_{rectum} dose. U_{rectum} is set to 80% of D_p in the branch-and-bound method.

* The hard constraint for the minimum dose to the target ($\min D_{\text{target}}$) for patients I and J is set 80% of D_p in the branch-and-bound method. It is set to 90% of D_p for other patients.

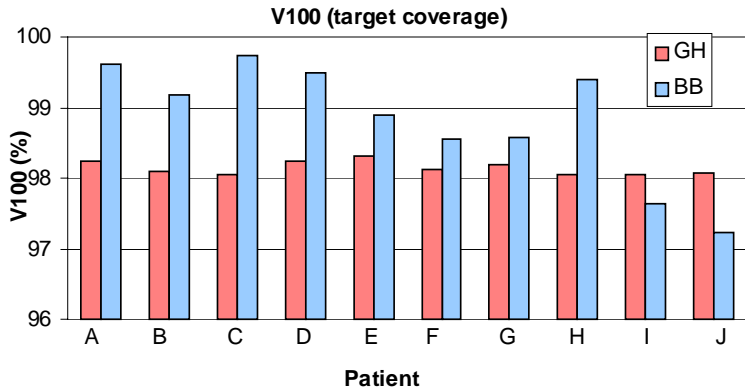


Figure 6.4 V100 (target coverage) comparison between the greedy heuristic (red) and the branch-and-bound method (blue)

The V100 is the volume of the target enclosed by 100% of the prescribed dose, which measures the target coverage [42]. The greedy heuristic has the target coverage slightly greater than 98% due to the termination criterion ($C_{\text{coverage}} = 98\%$). The branch-and-bound method has higher target coverage than the greedy heuristic in 8 patients. The branch-and-bound method has lower target coverage than the greedy heuristic in patient I and patient J whose needle configurations were predetermined. This lower target coverage can be because of $\min D_{\text{target}}$ that has been set to 80% of the prescribed dose and because of the predetermined needle configuration. Figure 6.4 displays the comparison in a column plot. Except for patients I and J, the branch-and-bound plans have the better target coverage. However, it is observed that the greedy heuristic results in consistent V100 values for all patients.

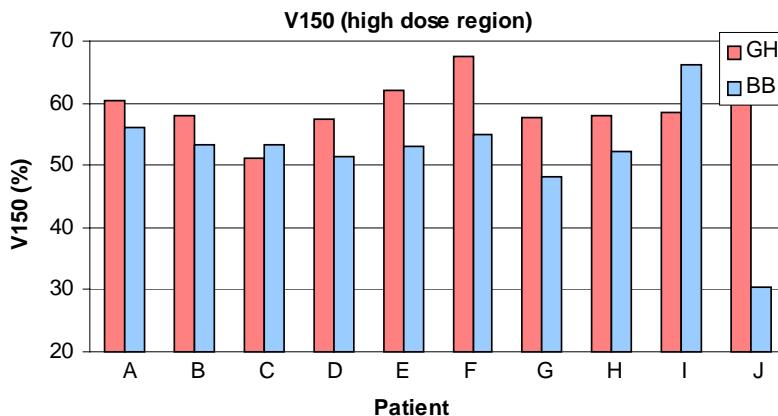


Figure 6.5 V150 (high dose region) comparison between the greedy heuristic (red) and the branch-and-bound method (blue)

The target volume enclosed by a high dose is measured by V150 [61]. Except in patients C and I, the V150 values are greater for the greedy heuristic plans than for the branch-and-bound plans. Since we imposed the upper dose soft-constraint 150% of D_p over the target in the basic MIP model, the plans obtained by the branch-and-bound method tend to have better results on this category. This feature is related to the dose uniformity, which will be discussed later. Figure 6.5 shows the comparison of V150 between the greedy heuristic and the branch-and-bound method in a column plot. The better V100 values and lower V150 values for the branch-and-bound method yield a more homogeneous dose distribution in the target.

The D90 values in all treatment plans obtained by both methods are higher than the suggestion of Stock *et al.*, [64, 65] which is D90 should be between 140 and 160 Gy. $D90 < 140$ Gy had lower rate of free from failure than D90 of ≥ 140 Gy [53]. However, patients who received doses greater than 160 Gy did not show an evidence of better treatment outcomes [64].

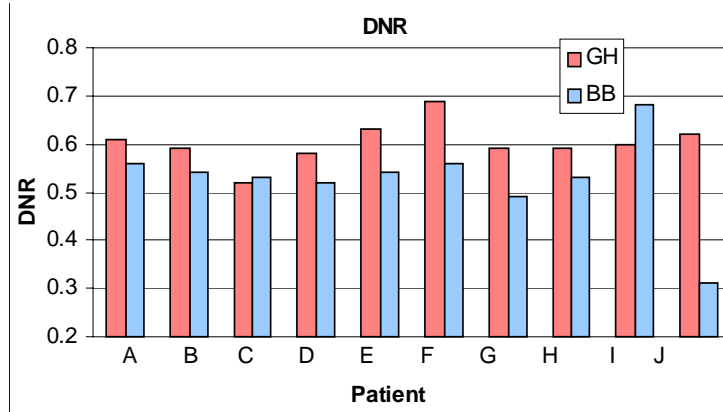


Figure 6.6 DNR (dose non-uniformity ratio) comparison between the greedy heuristic (red) and the branch-and-bound method (blue)

The dose uniformity is measured by the dose nonuniformity ratio (DNR) [60, 61]. A low DNR value indicates more homogeneous dose distribution [60]. Except patients C and I, DNR values by the greedy heuristic are higher than the branch-and-bound method. As it was pointed in the DVH discussion, the branch-and-bound method solving the basic model generally performs a better job with dose homogeneity within the target. Figure 6.6 shows this comparison.

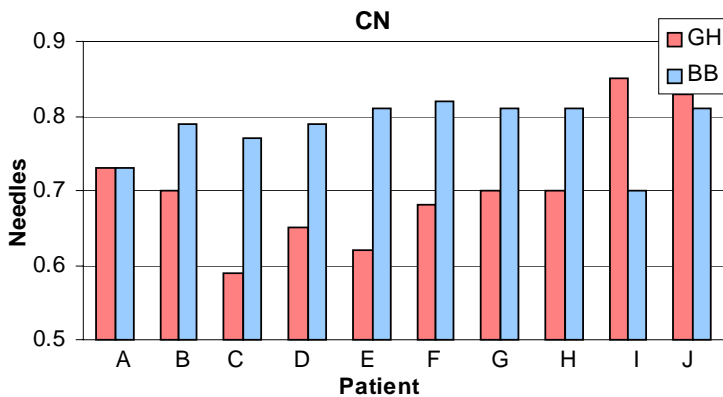


Figure 6.7 CN (Conformation number) comparison between the greedy heuristic (red) and the branch-and-bound method (blue)

The conformation number (CN) values for the branch-and-bound method are overall better than those for the greedy heuristic. The low CN value means that dose is wasted. The wasted dose goes to the normal surrounding tissue or other critical structures and, in addition, some parts of the target do not receive the prescribed dose. Thus, the higher CN value indicates a better dose conformality. Riet *et al.* [56] concluded that the CN value for prostate implants using ^{125}I seeds averaged 0.72 and a treatment plan with a CN greater than 0.60 was conformal radiotherapy. The greedy heuristic results in a satisfying CN value for patients except patient C, where the CN value is 0.01 lower than 0.60. Because the target volume of patient C is so small, the total volume receiving the prescribed dose (V_{D_p} in equation 4.6) is relatively large compared to the target volume receiving the prescribed dose (V_{target,D_p} in equation 4.6). Figure 6.7 shows the CN comparison.

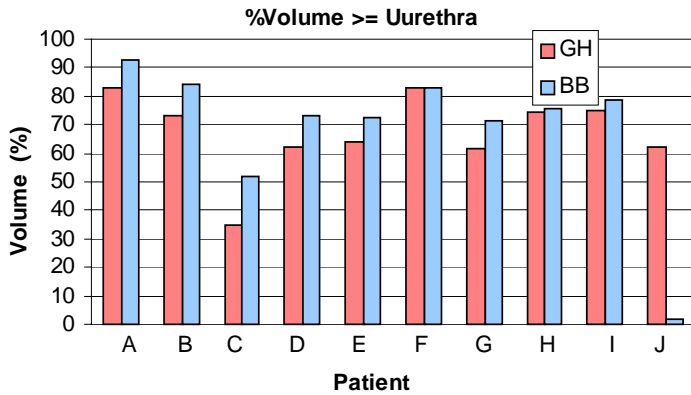


Figure 6.8 Comparison of percentage urethral volume greater than or equal to $U_{urethra}$ between the greedy heuristic (red) and the branch-and-bound method (blue)

Evaluation of the treatment plans for the urethra show that the U360 [16, 40, 69] (urethra volume enclosed by 360Gy) values are very small for all patients in both methods. The percentage volume of the urethra that receives a dose greater than the upper dose constraint ($\%Volume \geq U_{urethra}$) can be evidence for urethra sparing. In most cases, the greedy heuristic has smaller %Volume than the branch-and-bound method; meaning the greedy heuristic performs a better job in sparing the urethra. However, this %Volume value for patient J is very low in the branch-and-bound method. Figure 6.8 shows shorter columns for the greedy heuristic in most patients except in patient J, where the branch-and bound plan has an excellent urethra sparing. This can also seen in the DVHs in figure 6-3(j).

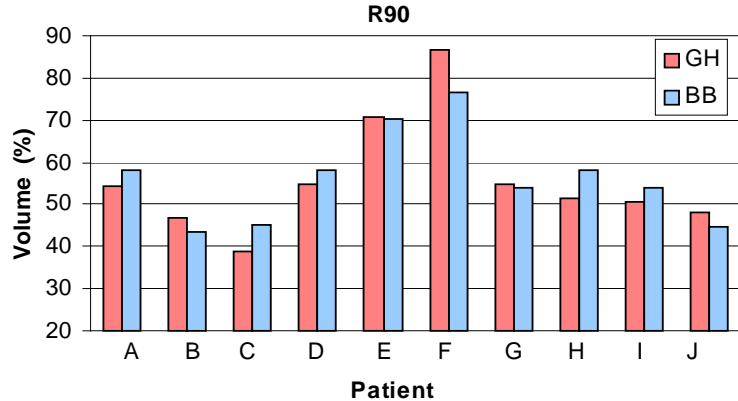


Figure 6.9 Comparison of R90 between the greedy heuristic (red) and the branch-and-bound method (blue)

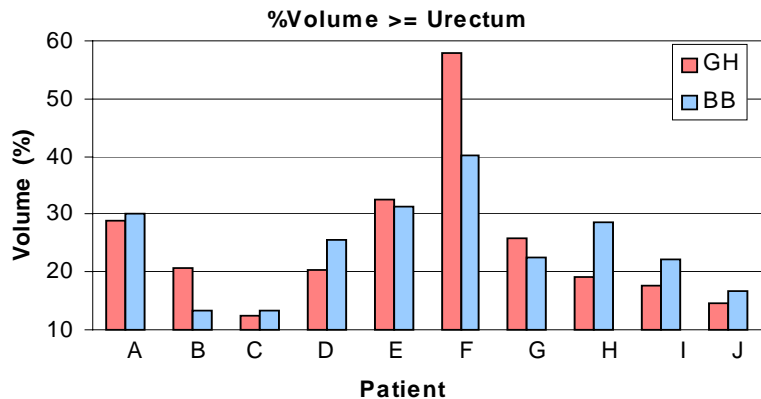


Figure 6.10 Comparison of percentage rectal volume greater than or equal to U_{rectum} between the greedy heuristic (red) and the branch-and-bound method (blue)

The R90 [40, 69] (rectum volume enclosed by 90Gy) and the percentage volume of the urethra enclosed by the upper dose constraint ($\% \text{Volume} \geq U_{\text{rectum}}$) can compare the quality of treatment plans in rectal sparing. Figure 6.9 and figure 6.10 display those values in columns. As discussed with the DVHs, the greedy heuristic and the branch-and-bound method have similar degrees of rectal sparing. For some patients, the greedy heuristic results in smaller value for R90 and $\% \text{Volume}$, and for other patients, the branch-and-bound method has smaller values.

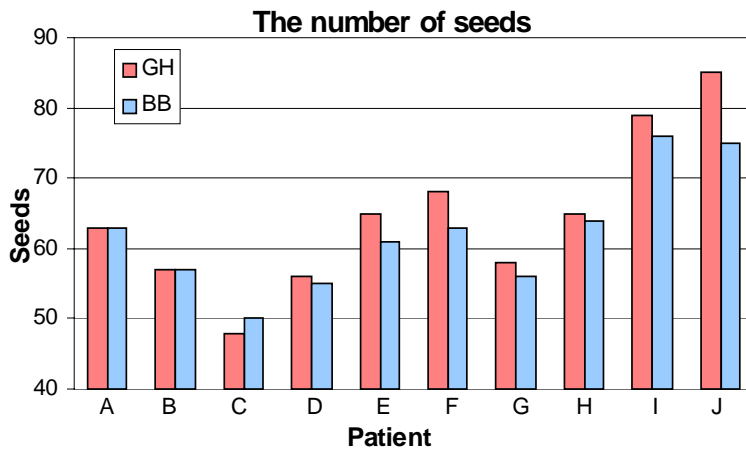


Figure 6.11 Comparison of the number of seeds used in the greedy heuristic (red) and the branch-and-bound method (blue)

The numbers of seeds used in all treatment plans obtained by the greedy heuristic are greater than or equal to those obtained by the branch-and-bound method except for patient C. More seeds in the greedy heuristic plans yield high V150 and high DNR values. Figure 6.11 shows this comparison.

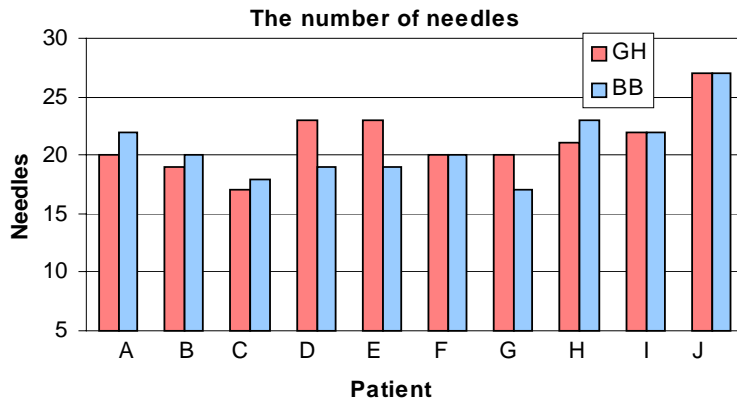


Figure 6.12 Comparison of the number of needles used in the greedy heuristic (red) and the branch-and-bound method (BB)

The numbers of needles used in treatment plans are similar for the greedy heuristic and the branch-and-bound method. This is shown in figure 6.12. For some patients, the greedy heuristic uses fewer needles (patient A, B, C, and H), for other patients, the greedy heuristic uses more needles (patient D, E, and G). For several patients, the greedy heuristic and the branch-and-bound method use the same number of needles (patient F, I, and J). The range of needles used is 17 to 27 depending on the target volume. Note, for patients I and J, we determined the needle configuration manually and used the number of needles, which was obtained by the greedy heuristic.

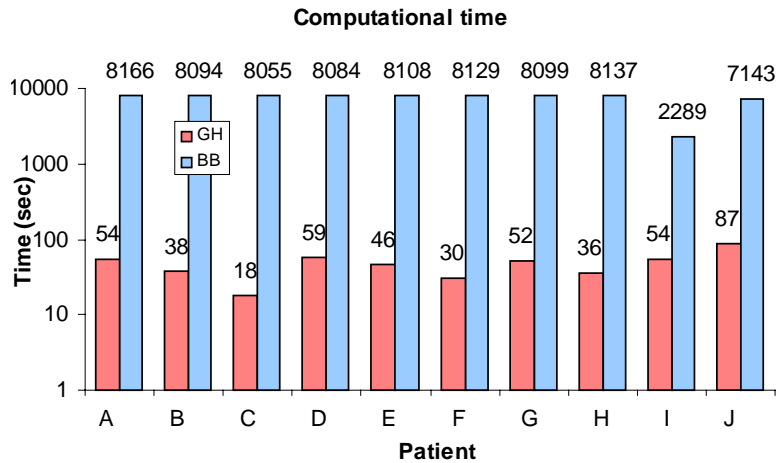


Figure 6.13 Comparison of the computational time spent by the greedy heuristic (red) and the branch-and-bound method (blue)

The greedy heuristic spent 18 to 87 seconds to construct a complete seed configuration, whereas the branch-and-bound method for full optimization required about 8000 seconds to reach a feasible solution. We set a limitation for time in order to terminate the branch-and-bound process in GAMS. We tried different time limitations and found that a feasible solution could require at least 8000 seconds. For patient I, the branch-and-bound method spent about 2000 seconds because the needle configuration was predetermined. However, for patient J, even if the needle configuration was determined in advance, it took about 7000 seconds. It may be because the large number of needles (27 needles) for patient J increases the search space and computational time compared to patient I. Figure 6.13 shows this comparison. Time is in log scale due to the large differences between results for two methods.

The evaluation parameters listed in table 6.3 compare the treatment plans obtained by the greedy heuristic and the branch-and-bound method. The branch-and-bound method shows a better target coverage and dose uniformity. However, the greedy heuristic usually shows a better

urethra sparing. The rectum sparing is similar in the greedy heuristic and the branch-and-bound method. The resulting number of needles is also similar.

The greedy heuristic clearly out performs the branch-and-bound method in the computational time required to arrive at a treatment plan. The automated constraint value selection process scanned through possible combinations of constraint values until a successful solution was reached. The greedy heuristic with this automatic selection of constraint values was still very fast even if it performed many trials because 1) one successful trial of the greedy heuristic takes less than 2 seconds (in Chapter 4 and Chapter 5, we discussed the reasons that the greedy heuristic constructs a seed configuration very quickly), 2) failure trials do not consist of a complete seed configuration so that one failure trial would take less time than one successful trial, and 3) there is only one successful combination of constraint values so that all other trials are failure.

6.4. Conclusion

In this chapter we employed an automatic selection strategy of constraint values. As in Chapter 4 and Chapter 5, the greedy heuristic searches the search space for a seed position, which has a minimum adjoint ratio value. An isodose surface constraint determines the search space at each step, and a selected seed position is added onto the seed configuration simultaneously updating the needle configuration. Once the number of needles reaches a desired preset number, a different isodose surface constraint determines the search space, which is restricted along the selected needles at the same time. We preset two different isodose surface constraints and a max needle constraint for the number of needles. In Chapter 5, all constraint values were selected based on a

trial-and-error process. We had to repeatedly set a combination of the constraint values until a successful seed configuration was found. However, this chapter reduces this effort by employing an automatic selection scheme for the constraint values.

As shown in Chapter 4 and Chapter 5, one successful execution of the greedy heuristic took less than 2 seconds, which was almost 2500 (in Chapter 4) to 4000 (in Chapter 5) times shorter than the time required by the branch-and-bound method. The process for an automatic selection of the constraint values scans possible combinations of the constraint values until a successful seed configuration is achieved.

Since characteristics of constraints are known, we can estimate the ranges of constraint values. The range for C_{needle} can be approximated based on the desired number of needles. We can estimate the desired number of needles from treatment plans used in actual treatments. The range of C_{iso1}^m can be estimated based on the minimum average dose delivered to an entire target by a single source. This minimum average dose value can be computed for each patient case with a known target volume. The range of C_{iso2} can be estimated based on the ultimate dose coverage to the target, which is the prescribed dose level.

The greedy heuristic constructs a seed configuration with each possible combination of the constraint values within the ranges. Starting from the lowest values, the greedy heuristic terminates whenever a successful configuration is reached. The lower the constraint values, the better the treatment plan, because it is desirable to have fewer needles and a more homogenous dose distribution within the target. As discussed in Chapter 4, a smaller isodose surface constraint value will result in a more homogeneous dose distribution within the target.

The results prove that the greedy heuristic with this automated selection scheme can produce good treatment plans very quickly. Moreover, this automatic selection scheme saves the efforts of manually setting all constraint values.

Chapter 7

Conclusions and future work

7.1. Conclusions

The purpose of this study was to find an efficient optimization algorithm for brachytherapy treatment planning. As needs for re-optimization and intra-operative treatment planning increase, the role of fast treatment planning becomes important.

The proposed search strategy was based on the adjoint functions of ROIs and the greedy heuristic. The adjoint function of an ROI provides a sensitivity distribution of the average dose delivered in the ROI to possible seed positions. The adjoint ratio combines the adjoint functions of critical structures in the numerator and the adjoint function of the target in the denominator. The optimization goal is to deliver a desired dose to the target while sparing the critical structures. The adjoint ratio as a function of seed position can estimate the ability of each seed position to achieve this goal. Therefore, each seed position can be ranked in the order of its adjoint ratio value.

The greedy heuristic makes a selection of a seed position that has a minimum adjoint ratio value with the search space. The greedy heuristic searches the search space, which is determined by an isodose surface constraint. The isodose surface constraint excludes an area where sufficient dose is delivered within the target; hence the search space includes seed positions in an underdosed area. The greedy heuristic constructs a complete seed configuration by adding a seed position at each step until the termination criterion is satisfied. By its nature, once the greedy heuristic selects a seed position, it does not revise or remove it from the seed configuration.

Chapter 4 introduced 1) the greedy heuristic search strategy using the adjoint ratio and 2) the isodose surface constraint to determine the search space. In order to focus on these two subjects, we did not include the consideration of needles. The result was compared to the result obtained by the branch-and-bound method solving the basic mixed-integer programming model. The evaluation of the results proved that the greedy heuristic could construct a good seed configuration within a couple of seconds, which is about a factor of 2500 shorter than the branch-and-bound method.

Chapter 5 introduced a needle constraint into the greedy heuristic algorithm. Two isodose surface constraints were used to restrict the search space in different situations, one before and one after the determination of the needle configuration. The greedy heuristic added seed positions onto the seed configuration one-by-one, based on the adjoint ratio. One isodose surface constraint restricted the search space within the target, excluding an area enclosed by the isodose surface. When the number of needles reaches a preset number, the other isodose surface constraint and the needle configuration determined the search space within the target. Values used for the two isodose surface constraints and the desired number of needles were found by trial-and-error. The results demonstrated that the greedy heuristic productively implemented the needle constraint.

In Chapter 6, because the process of selecting constraint values manually conflicts with the purpose of our study, which is developing an efficient optimization algorithm, we employed an automatic selection strategy for the constraint values. Ranges of all constraints were included in the greedy heuristic, which constructed a seed configuration for every possible combination of constraint values until a successful solution was achieved. The resulting treatment plans were compared to those obtained by the branch-and-bound method. The greedy heuristic performed better in some evaluation categories but more weakly in the other categories. In the computational time, the greedy heuristic absolutely outperforms the branch-and-bound method. Even if the greedy heuristic scans many trials with different constraint values, the computation time is just a couple of minutes.

Neither method can be considered superior to the other if we consider the resulting treatment plan itself. Perhaps the branch-and-bound method is more sophisticated at trimming the dose distribution by controlling constraints, whereas the greedy heuristic is a simpler procedure, which does not have detailed control over dose distribution. However, the greedy heuristic can achieve a good seed configuration within a couple of minutes. Moreover, as discussed in Chapter 6, it does not require a user to predetermine constraint values. As mentioned at the beginning of this chapter, the computational time for treatment planning is one of the most emphasized features in the intra-operative procedure or re-optimization process. With a patient being anesthetized in the operating room, this greedy heuristic method can yield a satisfying treatment plan without delaying the operation time.

In this study, the adjoint concept was used in brachytherapy treatment planning optimization. The adjoint concept as adopted in this study refers to that the adjoint function of an ROI which provides the sensitivity of dose in the ROI to source placement. In external beam

therapy, there have been a few studies to take advantage of this adjoint concept. It has been used for an initial guess of the beam weightings [35] and for a determination of beam orientations [25]. Jeraj and Keall [29] commented that the adjoint method could be used as an initial guess of the intensity distribution in an optimization. Difilippo [17] commented that there was a potential for a faster optimization method in the adjoint approach, which was the adjoint ratio as a function of beam position. However, there had been no studies, which have adopted the adjoint concept for brachytherapy treatment planning optimization prior to this study. Moreover, there had been no study to implement the adjoint concept as a major objective function in an optimization process until this investigation.

The primary success of this study is its demonstration of how the adjoint concept can improve the optimization process in radiation therapy treatment planning; not as an assisting function but as a major objective function. This study proves that the adjoint concept can accelerate the optimization process. The proposed optimization method promises a fast treatment planning process, which is essential for the intra-operative process or re-optimization.

7.2. Future work

- 1) The adjoint concept took the form of the adjoint ratio, which was the weighted sum of adjoint functions of the critical structures divided by the adjoint function of the target. For the beginning of this investigation, we set the weightings to unity for all critical structures. The adjoint ratio can be obtained with different weighting values. Seed positions, then, will be ranked differently.

- 2) Currently, the greedy heuristic uses a non-iterative scheme. Once a seed position is selected, it is not changed in a subsequent step. However, modification in a seed configuration can be performed iteratively after the greedy heuristic constructs a solution. This scheme will adopt the greedy heuristic to obtain an initial solution like an initial guess. More refined solution can be obtained by iterative process.
- 3) Seed positions on the peripheral area in the target can be highly weighted so that more needles would be selected on periphery. This weighting scheme can be obtained by the adjoint function of the target. A high gradient of the target adjoint function appears near periphery.
- 4) The ultrasound guided prostate implants utilize the template grid to guide needle insertion. The seed positions are restricted to the grid, which has a lattices form of apertures in 0.5 cm intervals. If we consider a template-free prostate implant procedure, each voxel within the target is a possible seed position. The current optimization methods already pursue enumerable computations with the restricted number of possible seed positions, and this template-free prostate implants could be beyond their computational ability. However, the adjoint function is available for continuous source positions, and the greedy heuristic will easily expand the search space.
- 5) As an extension of this study, the application of the greedy heuristic for optimization in the high-dose rate (HDR) after-loading treatment planning can be investigated. Unlike the selection of a seed position, each decision can represent an increment of discretized dwell time at each seed position. This idea can be applied in intensity modulated radiation therapy (IMRT). Each decision made by the greedy heuristic can represent an increment of beam weighting for each beam position.

- 6) The adjoint concept can be shaped in any form to project sensitivity and importance of sources to a region-of-interest. An optimization tool can be explored to take advantage of is *a priori* information.

Reference:

- [1] *American National Standard Neutron and Gamma-Ray Flux-to-Dose-Rate Factors 1977 – ANSI/ANS – 6.1.1* – (American Nuclear Society)
- [2] Amling C I, Blute M L, Bergstrahl E J, Seay T M, Slezak J and Zincke H 2002 Long-term hazard of progression after radical prostatectomy for clinically localized prostate cancer: Continued risk of biochemical failure after 5 years, *J. Urol.* **164**(1) 101 – 105
- [3] Anderson L L 1976 Spacing nomograph for interstitial implants of ^{125}I seeds, *Med. Phys.* **3**(1) 48 – 51
- [4] Bell G and Glasstone S 1970 *Nuclear reactor therapy* Chap. 1 & 6. (Princeton: Van Nostrand)
- [5] Blasko J C, Ragde H and Schumacher D 1987 Transperineal percutaneous iodine-125 implantation for prostatic carcinoma using transrectal ultrasound and template guidance, *Endocuriel/Hypertherm. Oncol.* **3** 131 – 139
- [6] Blasko J C, Grimm P D and Ragde H 1993 Brachytherapy and organ preservation in the management of carcinoma of the prostate, *Semin. Radiat. Oncol.* **3** 240 – 249
- [7] Brooke A, Kendrick D, Meeraus A and Raman R 1997 *GAMS: Language guide* (GAMS Development Corporation, Washington, D.C.)
- [8] Butler W M, Merrick G S, Lief J H and Dorsey A T 2000 Comparison of seed loading approaches in prostate brachytherapy, *Med. Phys.* **27** 381 – 392
- [9] Cancer facts and figures 2002 (American Cancer Society, Inc., Atlanta, GA 2002)
- [10] Chandrasekhar S 1960 *Radiative Transfer* (New York: Dover Publications)
- [11] Claiborne H C and Trubey D K 1970 Dose rates in a slab phantom from monoenergetic gamma rays, *Nucl. Appl. Tech.* **8** 450
- [12] *DANTSYS: User's guides* 1997 LA – 12969 – M (The Applied Physics (X) Division of Los Alamos National Laboratory, Los Alamos)

- [13] Daskalov G M, Baker R, Little R C, Rogers D W O and Williamson J F 1998 Multigroup discrete ordinates photon transport calculations of water kerma for brachytherapy applications, *Proceedings of the 1998 ANS Radiation Protection and Shielding Division Topical Conference 2* 261 – 268 (LaGrange Park, IL: ANS, Inc.)
- [14] Daskalov G M, Williamson J F, Baker R and Rogers D W O 1998 Dosimetric modeling of the MicroSelectron high-dose rate Ir-192 source by the multigroup discrete ordinates method, *Med. Phys.* **25** A119
- [15] Daskalov G M, Baker R S, Little R C, Rogers D W O and Williamson J F 2000 Two-dimensional discrete ordinate photon transport calculation for brachytherapy dosimetry applications, *Nucl. Sci. Eng.* **134** 121 – 134
- [16] Desai J, Stock R G, Stone N N, Iannuzzi C and DeWyngaert J K 1998 Acute urinary morbidity following I-125 interstitial implantation of the prostate glad, *Radiat. Oncol. Inv.* **6** 135 – 141
- [17] Difilippo F C 1998 Forward and adjoint methods for radiotherapy planning, *Med. Phys.* **25** 1702 – 1708
- [18] D’Souza W D 2000 A sequential mixed-integer optimization framework for permanent brachytherapy implants *Thesis* (Madison, WI: University of Wisconsin – Madison, Department of Medical Physics)
- [19] D’Souza W D, Meyer R R, Thomadsen B R and Ferris M C 2001 An iterative sequential mixed-integer approach to automated prostate brachytherapy treatment plan optimization, *Phys. Med. Biol.* **46** 297 – 322
- [20] D’Souza W D and Meyer R R 2001 Dose homogeneity ad a function of source activity in optimized I-125 prostate implant treatment plans, *Int. J. Radiat. Oncol. Biol. Phys.* **51**(4) 1120 – 1130
- [21] Edmundson G K, Yan D and Martinez A 1993 Intraoperative optimization of needle placement and dwell times for conformal prostate brachytherapy, *Int. J. Radiat. Oncol. Biol. Phys.* **33** 1257 – 1263
- [22] Ezzell G A 1996 Generic and geometric optimization of three-dimensional radiation planning, *Med. Phys.* **23** 293 – 305
- [23] Ferris M C 1998 *Matlab and GAMS: Interfacing optimization and visualization software* (Department of Computer Sciences, University of Wisconsin – Madison, WI)
- [24] Garfinkel R S and Nemhauser G L 1972 *Integer programming* (New York: A Wiley-Interscience, publication John Wiley & Sons, Inc.)

- [25] Gokhale P, Hussein E M A, and Kulkarni N 1994 Determination of beam orientation in radiotherapy planning, **3** 393 – 400
- [26] Grado G L, Larson T R, Balch C S, Collins J M, Kriegshauser J S, Swanson G P, Navickis R J and Wilkes M M 1998 Actuarial disease-free survival after prostate cancer brachytherapy using interactive techniques with biplane ultrasound and fluoroscopic guidance, *Int. J. Radiat. Oncol. Biol. Phys.* **42**(2) 289 – 298
- [27] Holland J H 1975 *Adaptation in natural and artificial systems* (Ann Arbor, MI: University of Michigan – Ann Arbor)
- [28] Holm H H, Juul N, Pedersen J F, Hansen H and Stroyer I 1983 Transperineal 125Iodine seed implantation in prostatic cancer guided by transrectal ultrasonography – The journal of urology, *J. Urol.* **130** 283 – 286
- [29] Jerai R and Keall P 1999 Monte Carlo-based inverse treatment planning, *Phys. Med. Biol.* **44** 1885 – 1896
- [30] ICRU 1997 Dose and Volume specification for reporting interstitial therapy, *International Commission on Radiation Units and measurements Report 58* (Bethesda, MD)
- [31] Kensek R P, Lorence L J Jr., Halbleib J A Sr. and Morel J E 1996 Space applications of the MITS Electron-Photon Monte Carlo Transport Code System. SAND96-1858c (Albuquerque, NM: Sandia National Laboratories)
- [32] Kirkpatrick S, Gelatt C D Jr. and Vecchi M P 1983 Optimization by simulated annealing, *Science* **220** 671 – 680
- [33] Korb L J and Brawer M K 2001 Moder brachytherapy for localized prostate cancers: the Northwest Hospital (Seattle) experience, *Rev. Urol.* **3**(1) 51 – 60
- [34] Kowalok M E and Henderson D L 2001 Adjoint Monte Carlo methods for radiation therapy treatment planning, *American Nuclear Society Annual Meeting* (Milwaukee, WI; June 2001)
- [35] Kowalok M E, Yoo S and Henderson D L 2002 Region-of-interest adjoint functions as an initial guess for iterative inverse treatment planning, *Med.Phys.* **29**(7) *American Associate of Physicists in Medicin Annual Meeting* (Montreal, Canada)
- [36] Langer M, Brown R, Morrill S, Lane R and Lee O 1996 A generic genetic algorithm for generating beam weights, *Med. Phys.* **23** 965 – 971
- [37] Lathrop K D and Carlson B G 1965 Discrete angular quadrature of the neutron transport equation, *LosAlamos Scientific Laboratory Report LA-3186*

- [38] Lee E K, Gallagher R J, Silvern D, Wuu D S and Zaider M 1999 Treatment planning for brachytherapy: an integer programming model, two computational approaches and experiments with permanent prostate implant planning, *Phys. Med. Biol.* **44** 145 – 165
- [39] Lewis E E and Miller W F Jr. 1993 *Computational methods of neutron transport* (LaGrange Park, IL: Ameircan Nuclear Society, Inc.)
- [40] Lowton C A, Won M and Pilepitch M V 1991 Lon-term treatment sequelae following external beam irradiation for adenocarcinoma of the prostate: Analysis of RTOG studies 7506 and 7706, *Int. J. Radiat. Oncol. Biol. Phys.* **21** 935 – 939
- [41] *Matlab User's guide* 1991 (The mathworks, Inc., Natick, MA)
- [42] Merrick G S, Butler W M, Dorsey A T and Lief J H 1999 The potential role of various dosimetric quality indicators in prostate brachytherapy, *Int. J. Radiat. Oncol. Biol. Phys.* **44** 717 – 724
- [43] Meyer R R 1979 *Integer programming* (Madison, WI : University of Wisconsin – Madison, Computer Science Department)
- [44] Meyer R R 2003 Personal communication
- [45] More J J and Wright S J 1993 Frontiers in applied mathematics: optimization software guide (Philadelphia, PA: Society for industrial and applied mathematics)
- [46] Nag S, Ciezki J P, Cormack R, Doggett S, DeWyngaert K, Edmundson G K, Stock R G, Stone N N, Yu Y and Zelefsky M J 2001 Intraoperative planning and evaluation of permanent prostate brachytherapy: report of the American Brachytherapy Society, **51** 1422 – 1430
- [47] Narayana V, Roberson P L, Winfield R J, Kessler M L and McLaughlin P W 1996 Optimal placement of radioisotopes for permanent prostate implants, *Radiology* **199** 457 – 460
- [48] Nath R, Anderson L L, K A Weaver K A, Williamson J F and Meigooni A S 1995 Dosimetry of interstitial brachytherapy sources: recommendations of the AAPM radiation therapy committee task group No. 43, *Med. Phys.* **22** 209 – 233
- [49] Nath R, Anderson L L, Meli J A, Olch A J, Stitt J A and Williamson J F 1997 Code of practice for brachytherapy physics: Report of the AAPM radiation therapy committee task group No. 56, *Med. Phys.* **24** 1557 – 1598
- [50] Nemhauser G L, Kan A H G R and Todd M J 1989 *Optimization* (New York: Elsevier Science Pub. Co.)
- [51] Pashchenko A B, Wienke H and Muir D W 1997 FENDL-2:An improved nuclear data library for fusion applications, 1150 – 1154 *International Conference on Nuclear Data for Science and Technology*, edited by Reffo G, Ventura A and Grandi C (Trieste, Italy)

- [52] Pouliot J, Tremblay D, Roy J and Filice S 1996 Optimization of permanent ^{125}I prostate implants using fast simulated annealing, *Int. J. Radiat. Oncol. Biol. Phys.* **36** 711 – 720
- [53] Prestodge B R, Hoak D C, Grimm P D, Ragde H, Cavanagh W and Blasko J C 1997 Posttreatment biopsy results following interstitial brachytherapy in early stage prostate cancer, *Int. J. Radiat. Oncol. Biol. Phys.* **37** 31 – 39
- [54] Ragde H, Grado G L, Nadir B and Elgamal A A 2000 Modern prostate brachytherapy, *CA Cancer J. Clin.* **50**(6) 380 – 393
- [55] Redpath A 2002 Automatic determination of needle and source positions for brachytherapy of the prostate using ^{125}I odine rapid strand, *Radiother. Oncol.* **64**(2) 215 – 227
- [56] Riet A V, Mak A C A, Moerland M A, Elders L H and Zee W Van Der 1997 A conformation number to quantify the degree of conformality in brachytherapy and external beam irradiation: application to the prostate, *Int. J. Radiat. Oncol. Biol. Phys.* **37** 731 – 736
- [57] Roberson P L, Narayana V, McShan D L, Winfield R J and McLaughlin P W 1997 Source placement error for permanent implant of the prostate, *Med. Phys.* **24** 251 – 257
- [58] Roy J N, Wallner K E, Chiu-Tsao S T, Anderson L L and Ling C C 1991 CT-based optimization planning for transperineal prostate planning with customized template, *Int. J. Radiat. Oncol. Biol. Phys.* **21** 483 – 489
- [59] Sahni S 2000 *Data structures, algorithms, and applications in Java* (New York: The McGraw-Hill Companies, Inc.)
- [60] Saw C B and Suntharalingam N 1991 Quantitative assessment of interstitial implants, *Int. J. Radiat. Oncol. Biol. Phys.* **20** 135 – 139
- [61] Saw C B, Suntharalingam N and Wu A 1993 Concept of dose nonuniformity in interstitial brachytherapy, *Int. J. Radiat. Oncol. Biol. Phys.* **26** 519 – 527
- [62] Serov I V, John T M and Hoogenboom J E 1999 A midway forward-adjoint coupling method for neutron and photon Monte Carlo transport, *Nuc. Sci. Eng.* **133** 55 – 72
- [63] Sloboda R S 1992 Optimization of brachytherapy dose distribution by simulated annealing, *Med. Phys.* **19**(4) 955 – 964
- [64] Stock R G, Stone N N DeWyngaert J K, Lavagnini P and Unger P D 1996 Prostate specific antigen findings and biopsy results following interactive ultrasound guided transperineal brachytherapy for early stage prostate carcinoma, *Cancer* **77**(11) 2386 – 2392
- [65] Stock R G, Stone N N, Tabert A, Iannuzzi C and DeWyngert J K 1998 A dose-response study for $\text{I}-125$ prostate implants, *Int. J. Radiat. Oncol. Biol. Phys.* **41** 101- 108

- [66] Taha H A 1975 *Integer programming: Theory, applications, and computations* (New York: Academic Press, Inc.)
- [67] Tang J S and Hoffman T J 1988 Monte Carlo shielding analysis using an automated biasing procedure, *Nuc. Sci. Eng.* **99** 329 – 342
- [68] Thompson S A, Fung A Y C and Zaider M 2002 Optimal needle arrangement for intraoperative planning in permanent I-125 prostate implants, *Phys. Med. Biol.* **47** N209 – N215
- [69] Wallner K, Roy J and Harrison L 1995 Dosimetry guidelines to minimize urethral and rectal morbidity following transperineal I-125 prostate brachytherapy, *Int. J. Radiat. Oncol. Biol. Phys.* **32** 465 – 471
- [70] Webb S 1991 Optimization by simulated annealing of three-dimensional conformal treatment planning for radiation fields defined by a multileaf collimator, *Phys. Ned. Biol.* **36** 1201 – 1226
- [71] Whitmore W F, Hilaris B, and Grabstald H 1972 Retropubic implantation to iodine-125 in the treatment of prostatic cancer, *J. Urol.* **108** 918 – 920
- [72] Wells M B and Liversay R B 1972 Calculations of tissue kerma factors for monoenergetic x-rays between 0.1 keV and 1.0 MeV, Research Note RRA-N7216 (Radiation research associates, Inc.)
- [73] Williamson J F and Nath R 1991 Clinical implementation of AAPM Task Groupd 32 recommendations for brachytherapy source strength specification, *Med. Phys.* **18** 439 – 448
- [74] Williamson J F, Coursey B M, DeWard L A, Hanson W F, Nath R and Ibbott G 1999 Guidance to users of Nycomed Amersham and North American Scientific, Inc. I-125 interstitial sources: Dosimetry and calibration changes, *Med. Phys.* Version 5.21
- [75] Wolsey L A 1998 *Integer programming*, (John Wiley & Sons, Inc., New York)
- [76] Yang G, Reisten L E, Pai S and Xu Z 1998 A new genetic algorithm technique in optimization of permanent 125I prostate implant, *Med. Phys.* **25**(12) 2308 – 2315
- [77] Yoo S, Henderson D L and Thomadsen B R 2001 Optimization treatment planning for interstitial brachytherapy using the adjoint transport method, *American Nuclear Society Annual Meeting* (Milwaukee, WI; June 2001)
- [78] Yoo S, Kowalok M E, Henderson D L and Thomadsen B R 2002 Greedy (heuristic) algorithm for the optimization of prostate implant treatment planning using the adjoint distribution, *Med.Phys.* **29**(7) *American Associate of Physicists in Medicin Annual Meeting* (Montreal, Canada)

- [79] Yu Y and Schell M C 1996 A genetic algorithm for the optimization of prostate implants, *Med. Phys.* **23** 2085 – 2091
- [80] Yu Y, Schell M C and Zhang B 1997 Decision theoretic steering and genetic algorithm optimization: application to stereotactic radiosurgery treatment planning, *Med. Phys.* **24** 1742 – 1750
- [81] Yu Y, Anderson L L, Li Z, Mellenberg D E, Nath R, Schell M C, Waterman F M, Wu A and Blasko J C 1999 Permanent prostate seed implant brachytherapy: Report of the American Association of Physicists in Medicine Task Group No. 64, *Med. Phys.* **26** 2054 – 2076
- [82] Zagars G K 1994 Prostate specific antigen as an outcome variable for T1 and T2 prostate cancer treated by radiation therapy, *J. Urol.* **152** 1786 - 1791
- [83] Zietman A L, Coen I J, Shinpley W U 1994 Radical radiation therapy in the management of prostatic adenocarcinoma: the initial prostate specific antigen value as a predictor of treatment outcome, *J. Urol.* **151**(3) 640 – 645

Appendix A

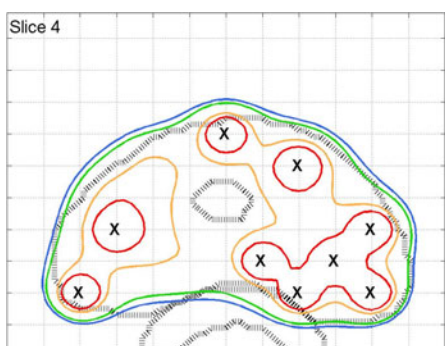
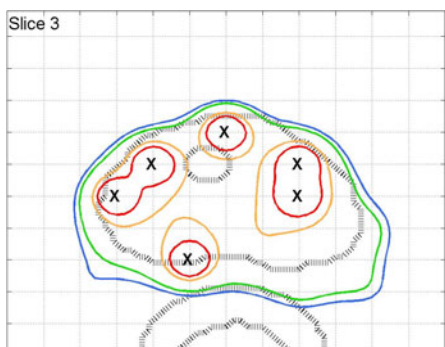
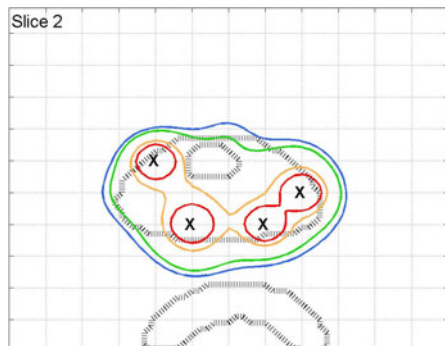
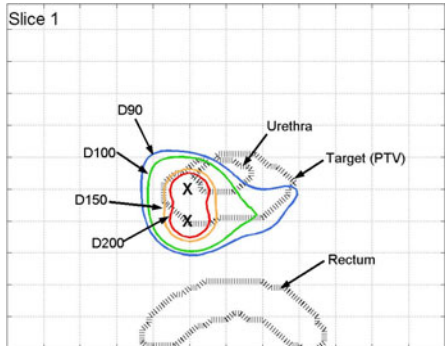
Isodose curves for Chapter 6 patient results

The treatment plans for 10 patients are displayed in this section. Isodose curves for all image slices of each patient and the dose-volume histograms are drawn for the comparison between the greedy heuristic and the branch-and-bound method. The isodose curves of 90%, 100%, 150%, and 200% of the prescribed dose (145Gy) are drawn in blue, green, orange, and red lines respectively, for patients A to H. Patients I and J have a large target volume and the branch-and-bound method used 80% of the prescribed dose for $\min D_{target}$. The 80% isodose curve of the prescribed dose is drawn in sky blue for patients I and J. The target (planning target volume, PTV), urethra, and rectum are contoured in dotted lines. The lattices grid intersections indicate potential needle insertion positions on the template grid. The left column shows the greedy heuristic result, and the right column shows the branch-and-bound result.

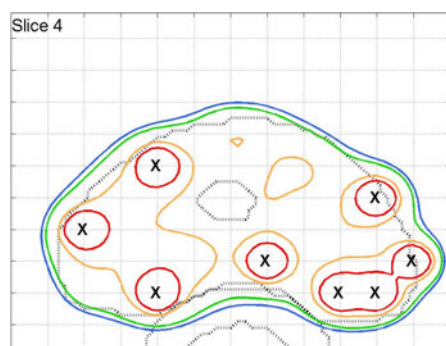
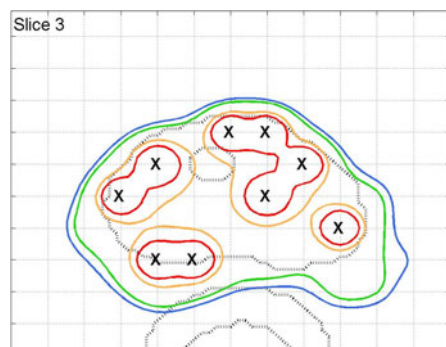
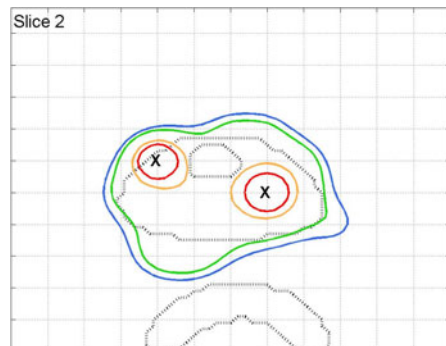
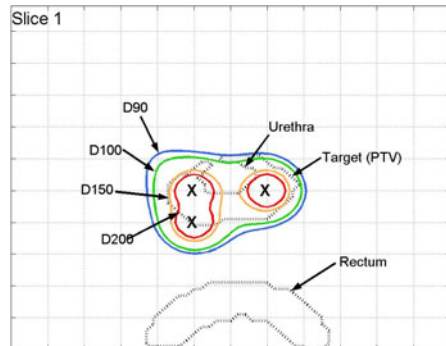
After the isodose curve comparison, the dose-volume histograms are compared for each patient. These curves are also displayed in figure 6.3. GH stands for the greedy heuristic method and BB is the branch-and-bound method.

Patient A

Greedy heuristic

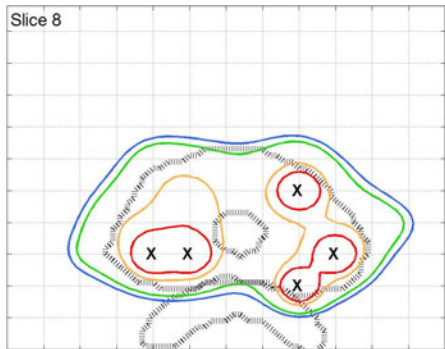
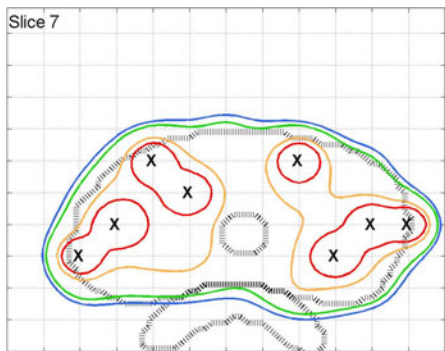
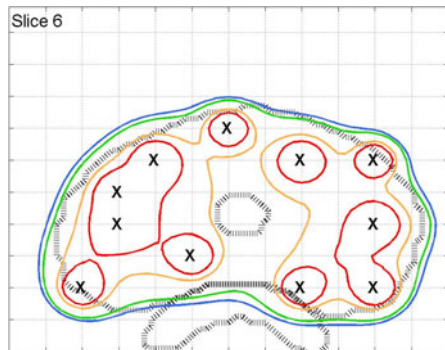
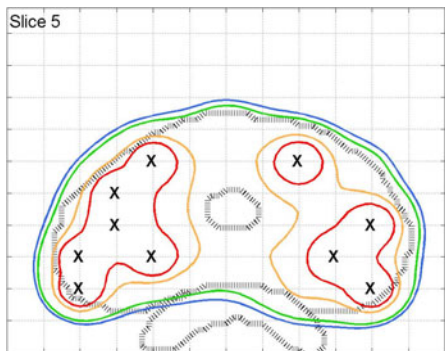


Branch-and-bound

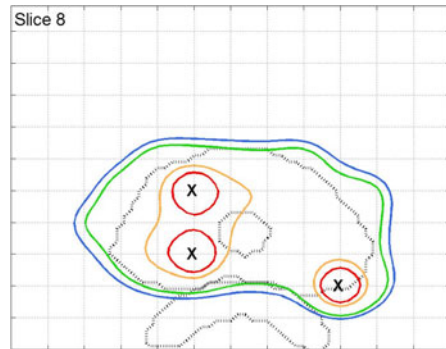
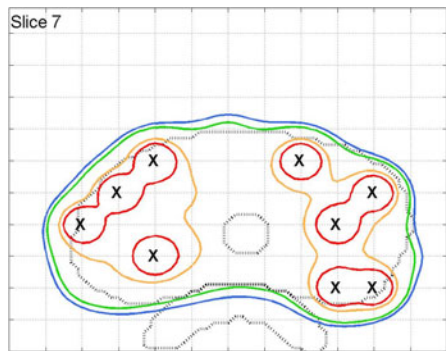
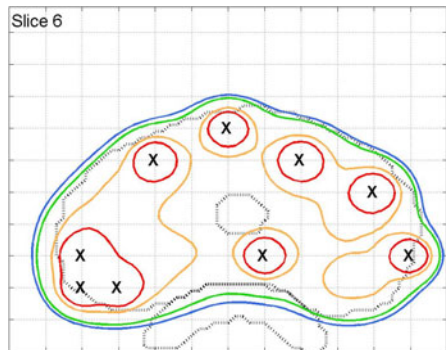
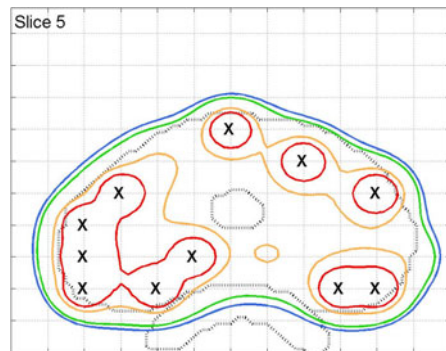


(patient A continued)

Greedy heuristic

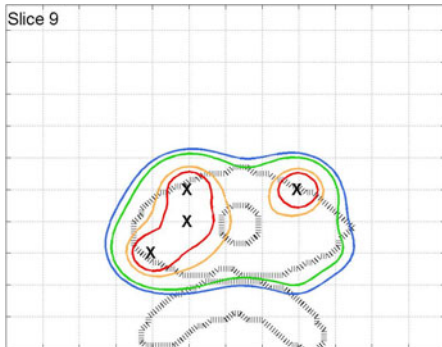


Branch-and-bound

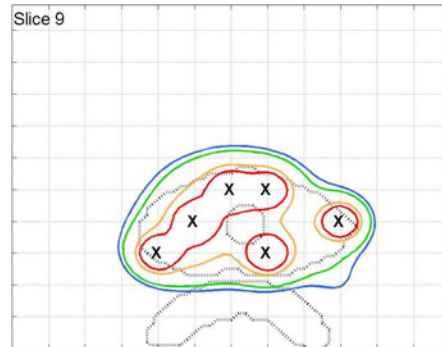


(patient A continued)

Greedy heuristic

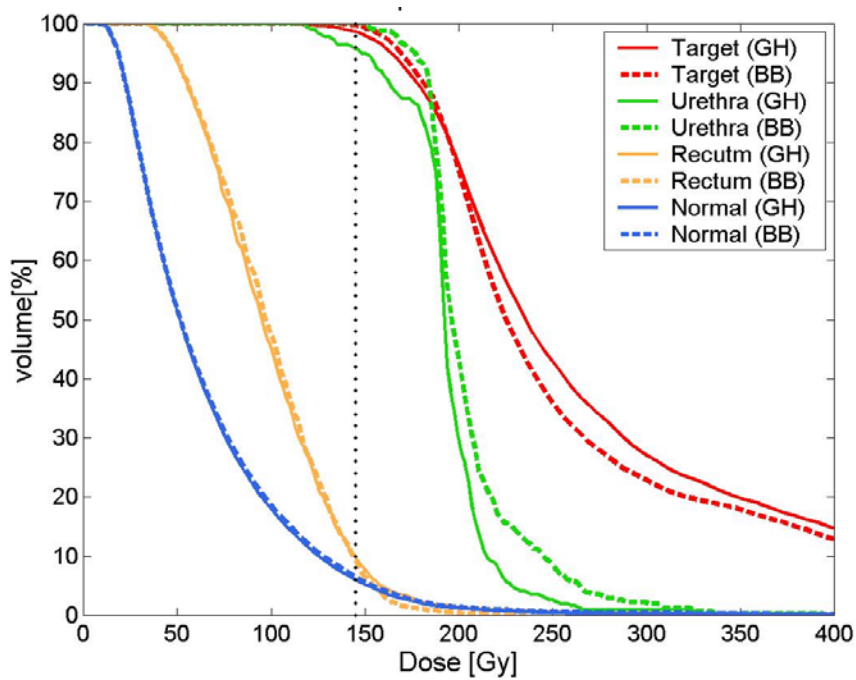


Branch-and-bound



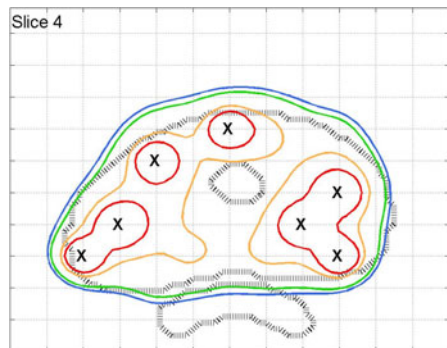
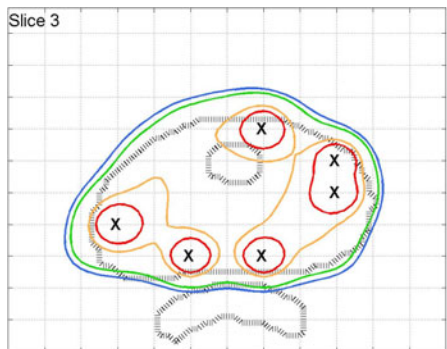
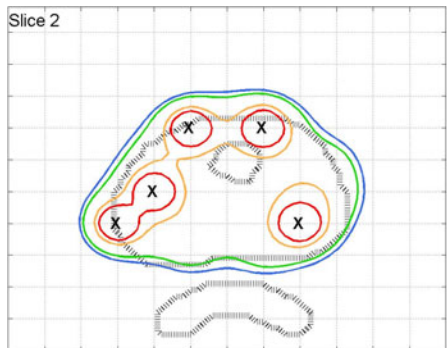
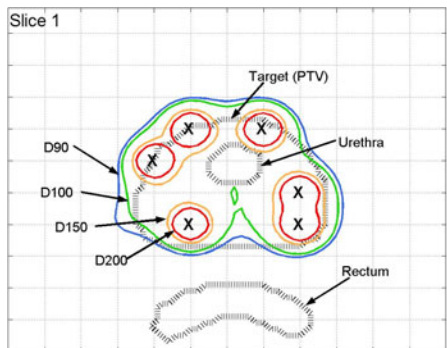
A hand-drawn diagram on grid paper. It features three concentric circles. The innermost circle is filled with a red 'X'. The middle ring is outlined in blue and also contains a red 'X'. The outermost ring is outlined in green and contains a red 'X'. The entire diagram is centered on the grid.

The diagram shows a cross-section of a brain slice, labeled "Slice 10" at the top left. Three distinct regions of interest (ROIs) are outlined with colored circles: a large green circle at the top center, a smaller orange circle positioned below and to the right of the green one, and another smaller orange circle positioned below and to the left of the green one. Each ROI contains a black "X". A dashed black outline at the bottom represents the pial surface.

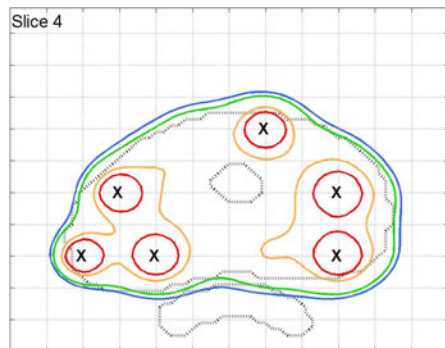
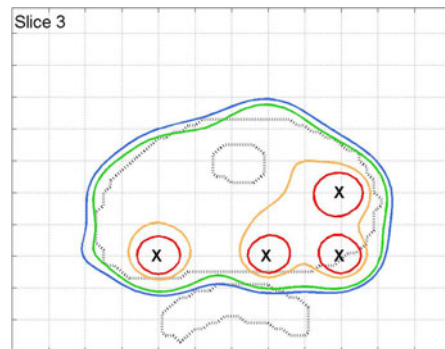
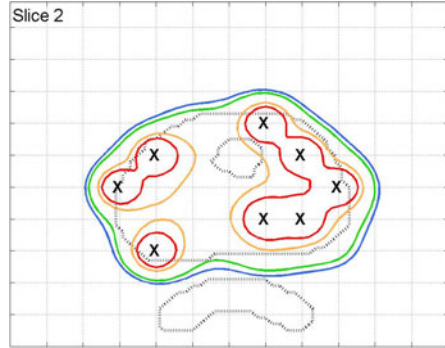
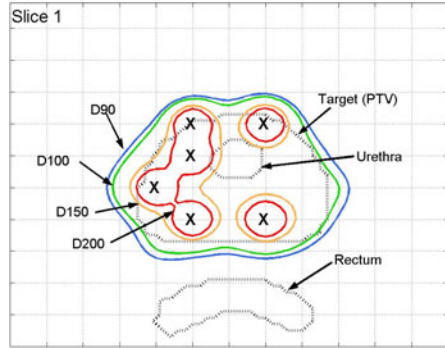


Patient B

Greedy heuristic

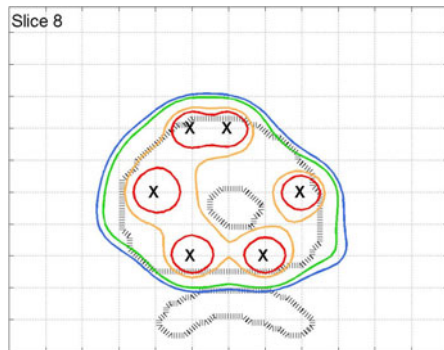
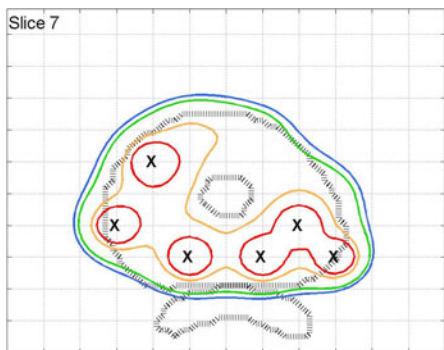
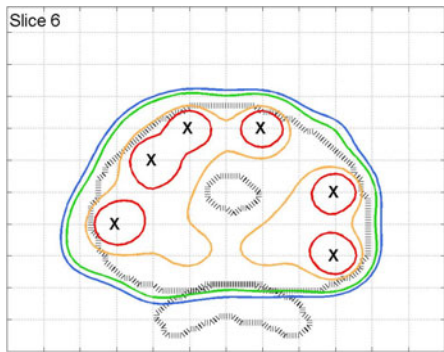
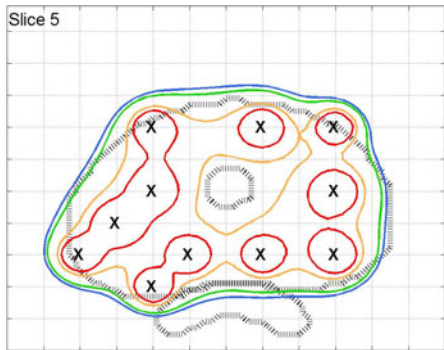


Branch-and-bound

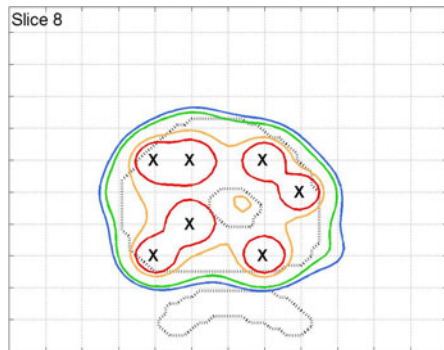
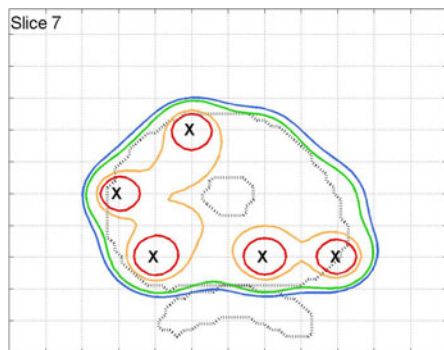
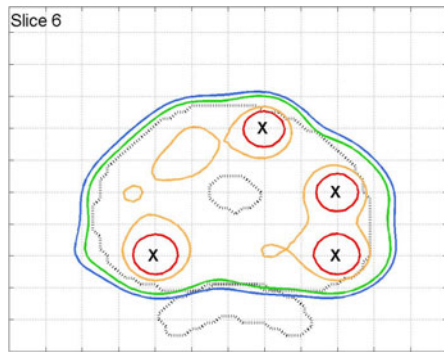
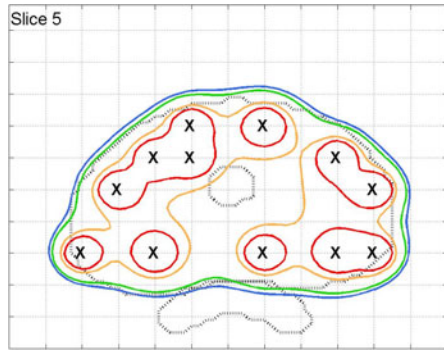


(patient B continued)

Greedy heuristic

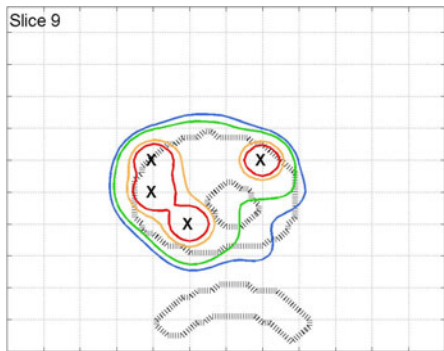


Branch-and-bound

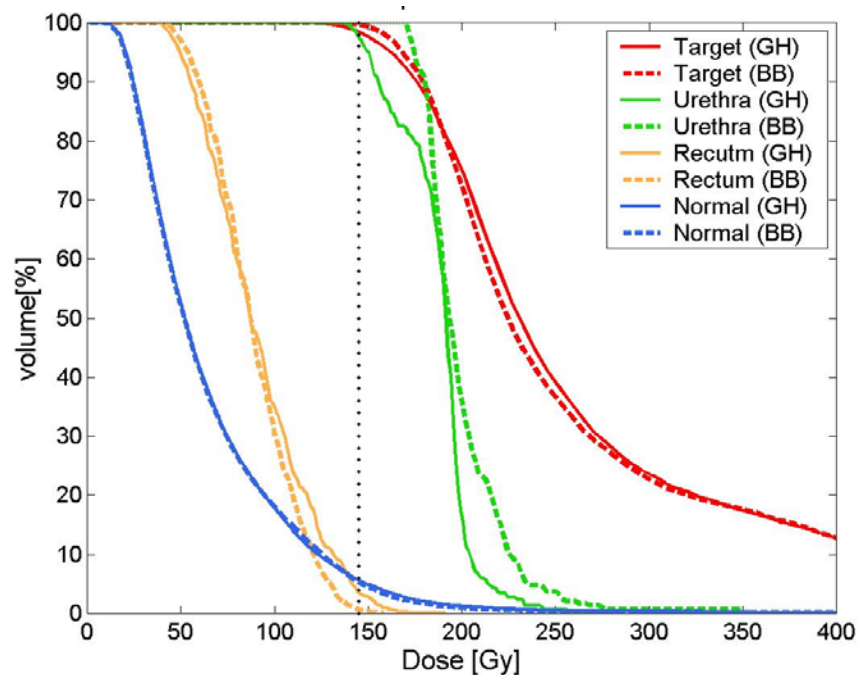
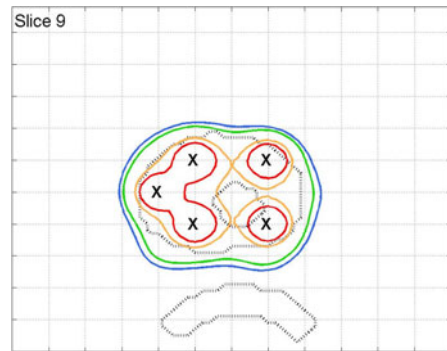


(patient B continued)

Greedy heuristic

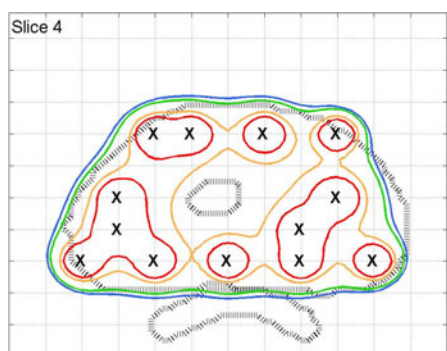
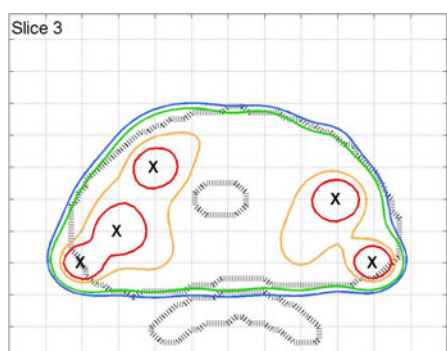
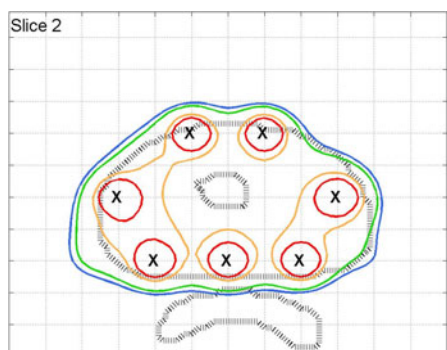
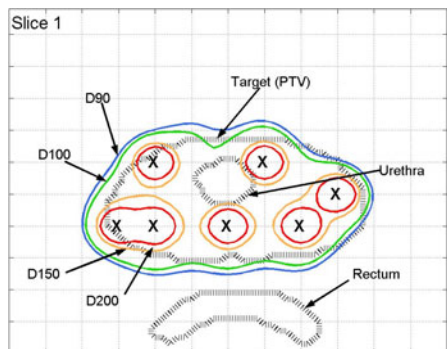


Branch-and-bound

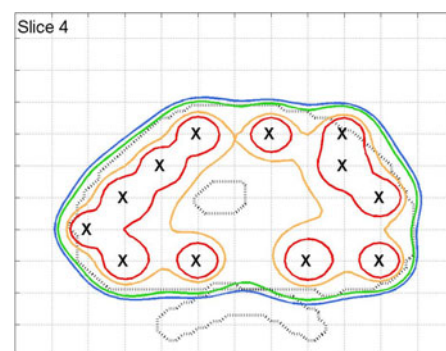
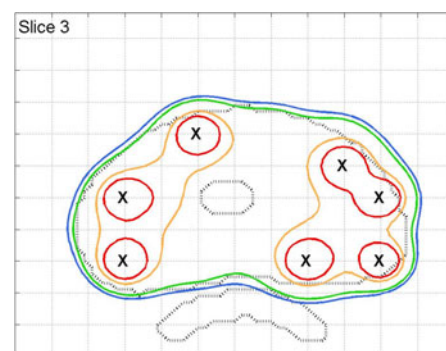
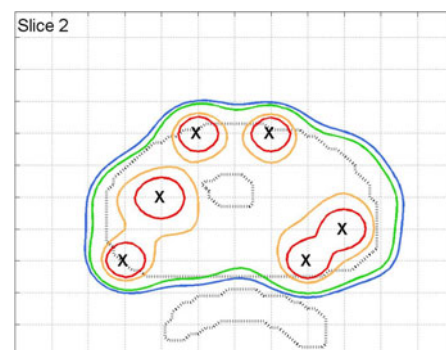
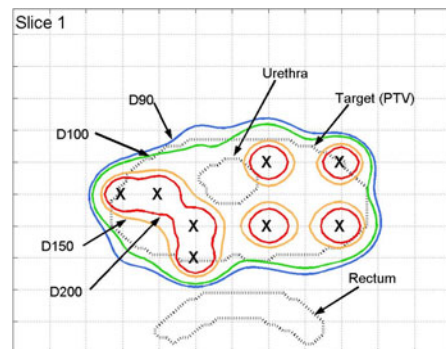


Patient C

Greedy heuristic

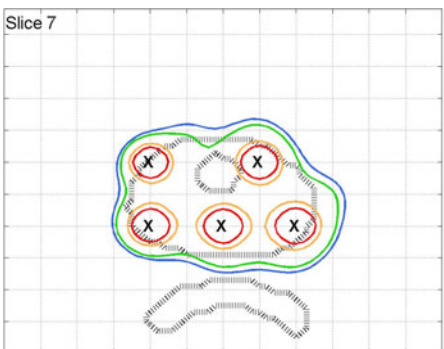
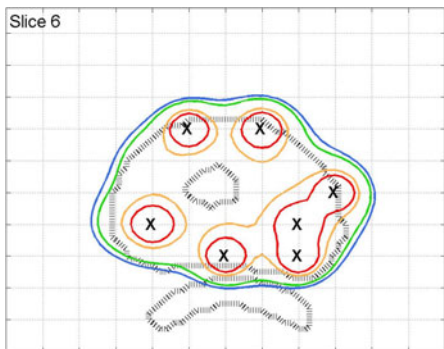
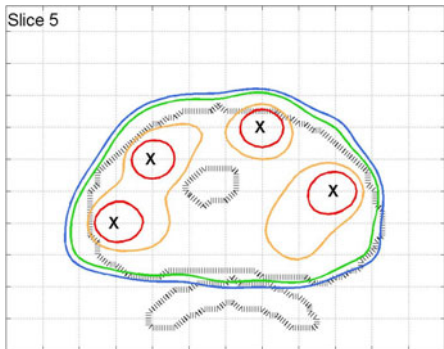


Branch-and-bound

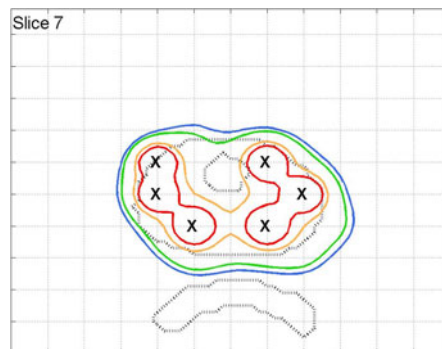
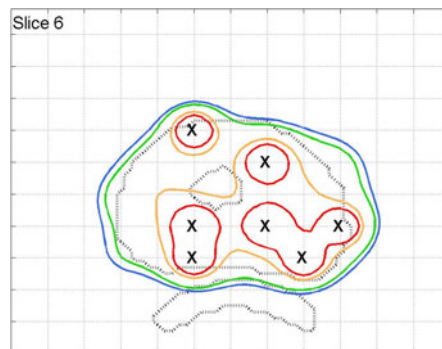
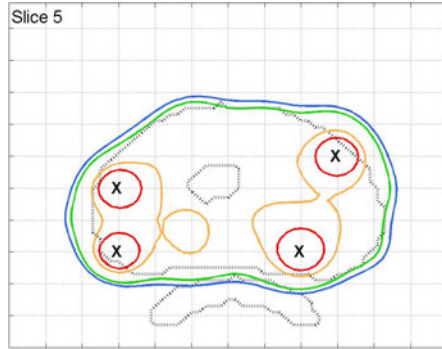


(patient C continued)

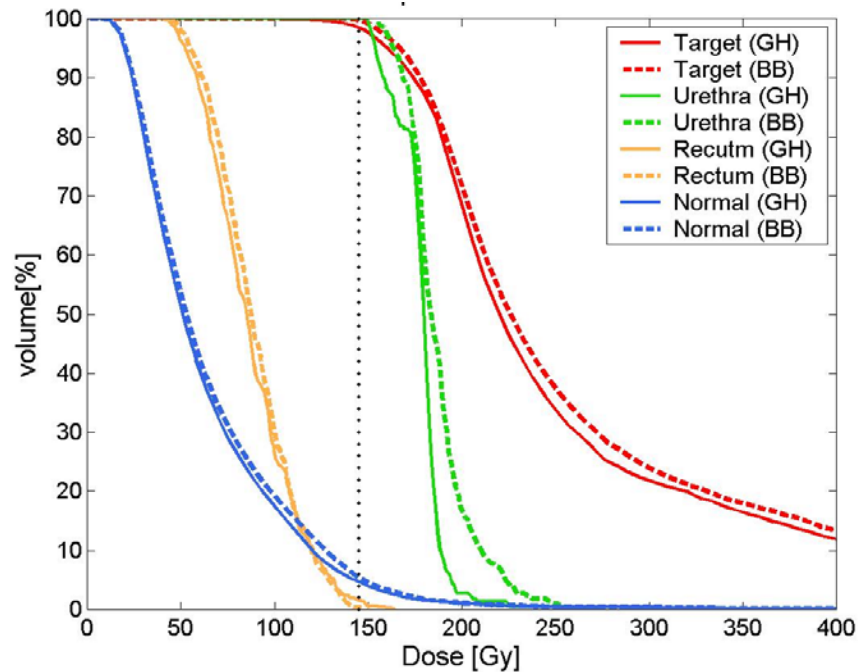
Greedy heuristic



Branch-and-bound

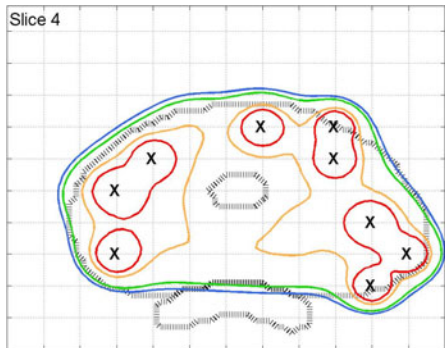
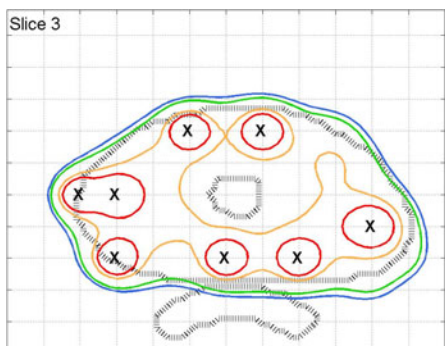
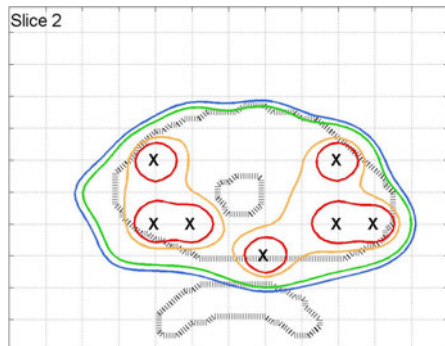
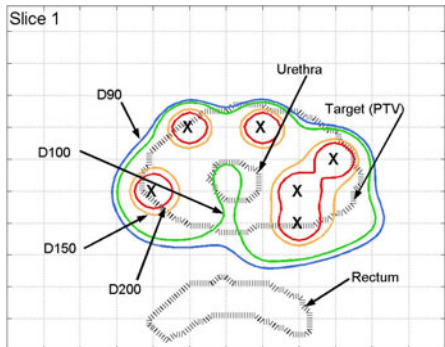


(patient C continued)

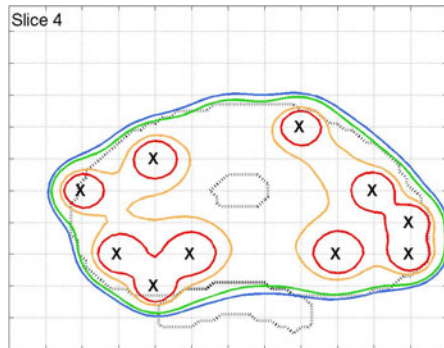
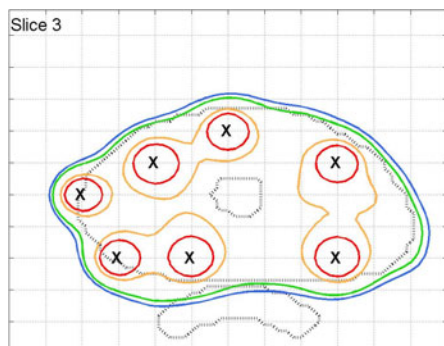
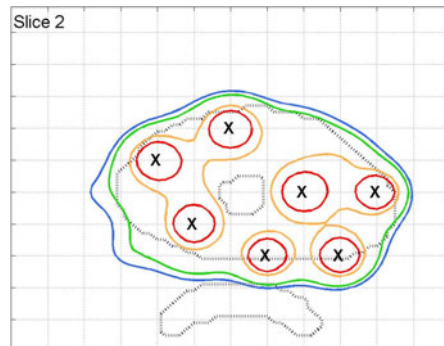
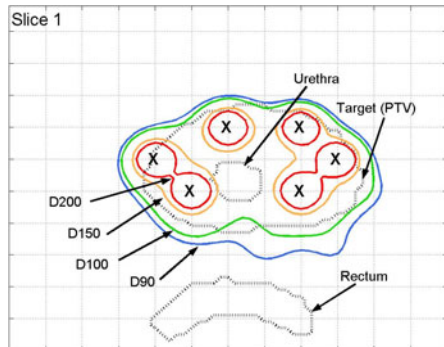


Patient D

Greedy heuristic

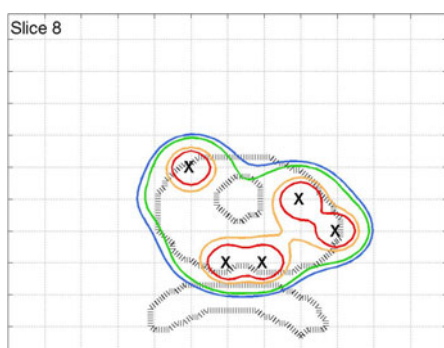
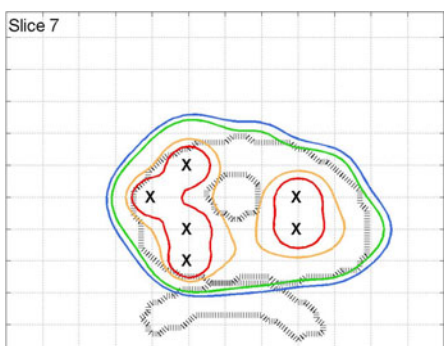
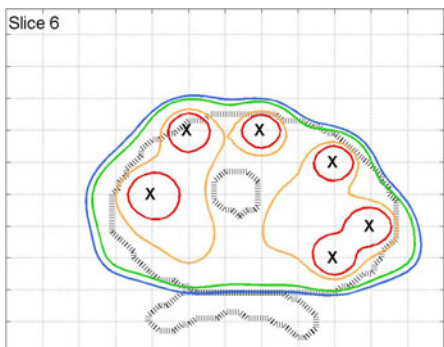
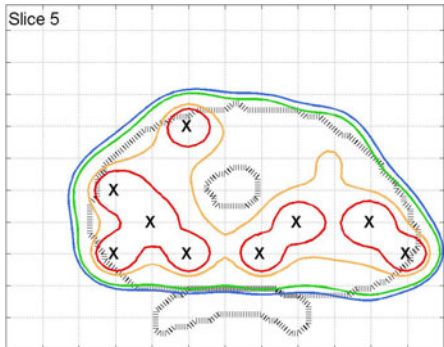


Branch-and-bound

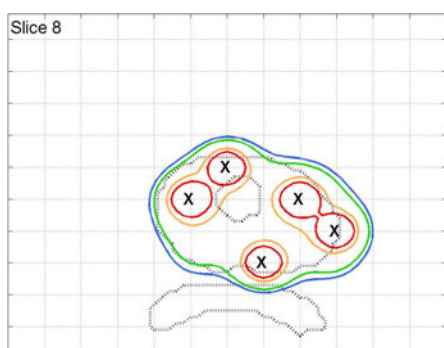
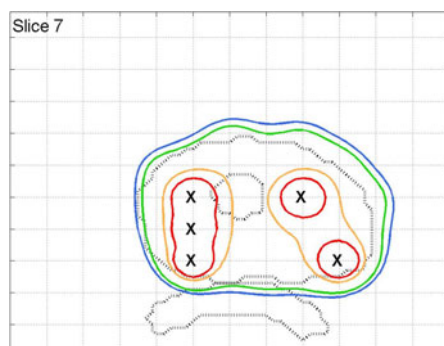
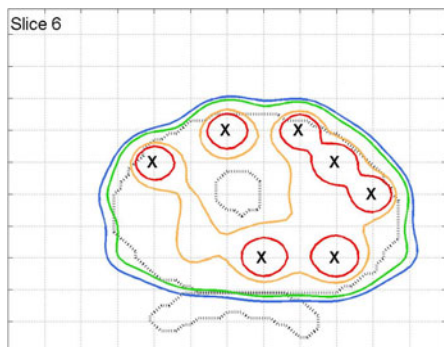
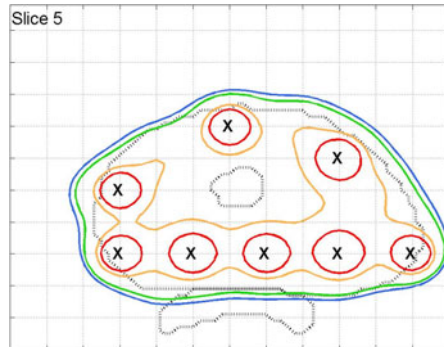


(patient D continued)

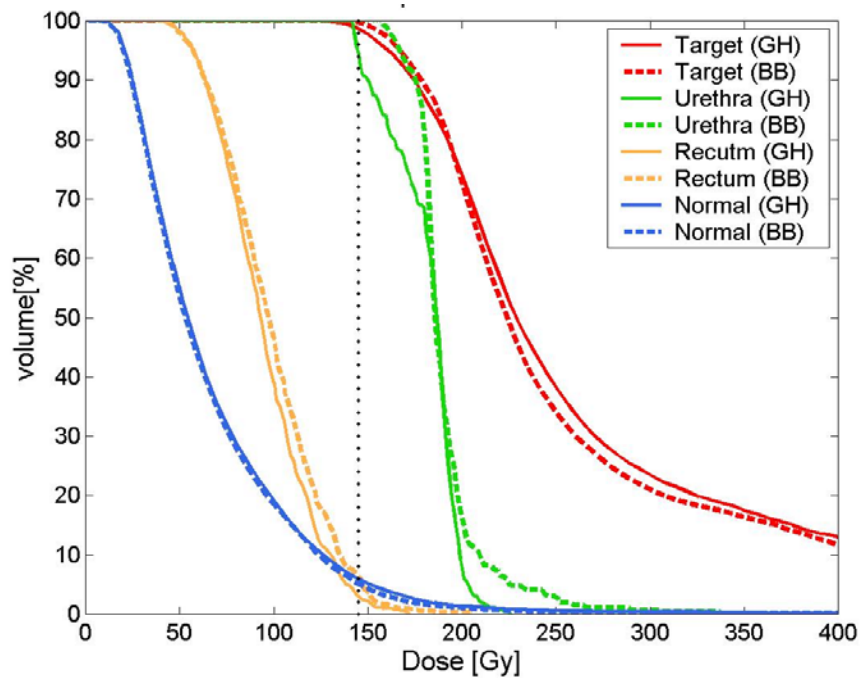
Greedy heuristic



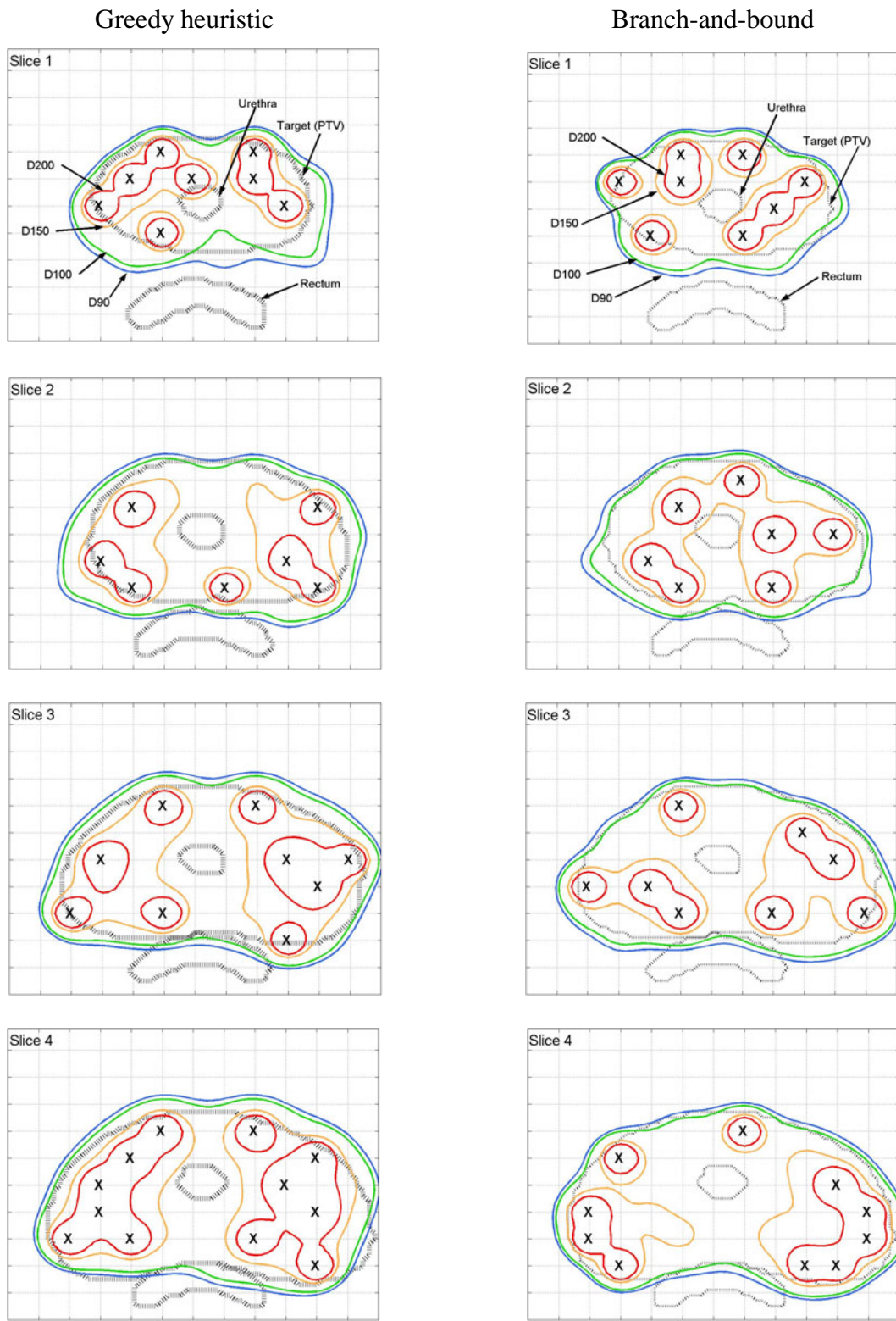
Branch-and-bound



(patient D continued)

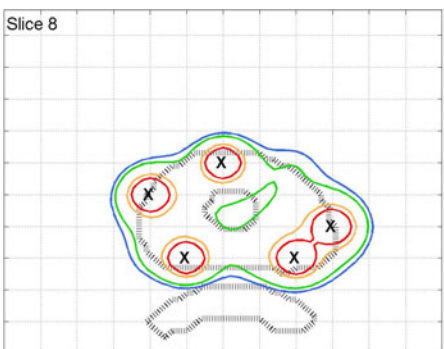
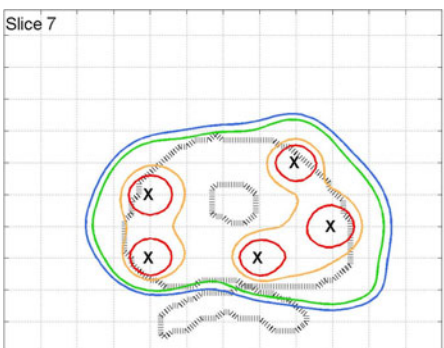
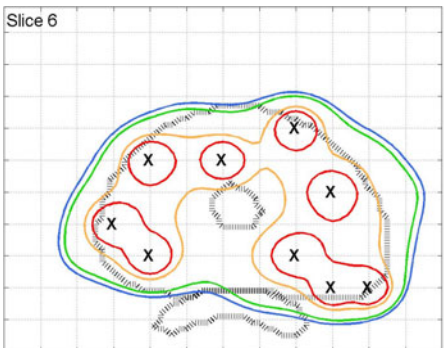
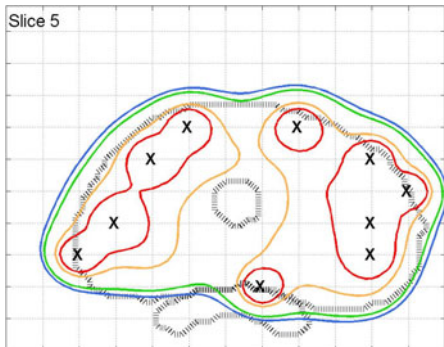


Patient E

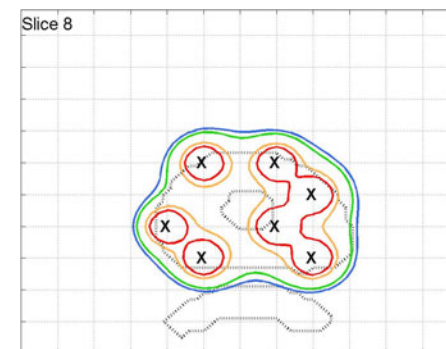
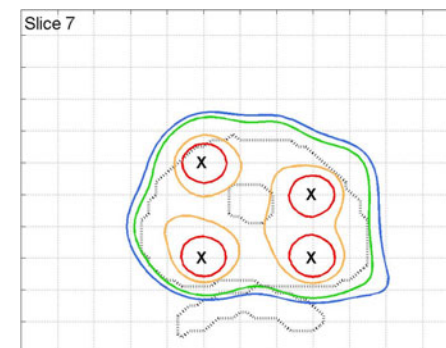
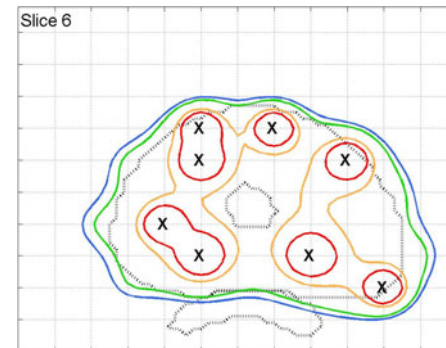
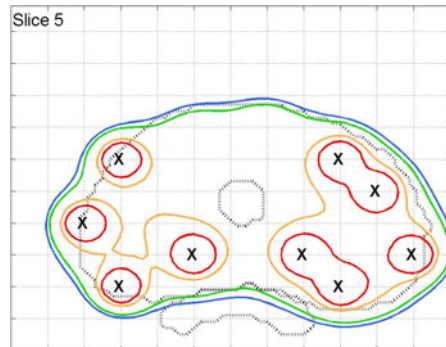


(patient E continued)

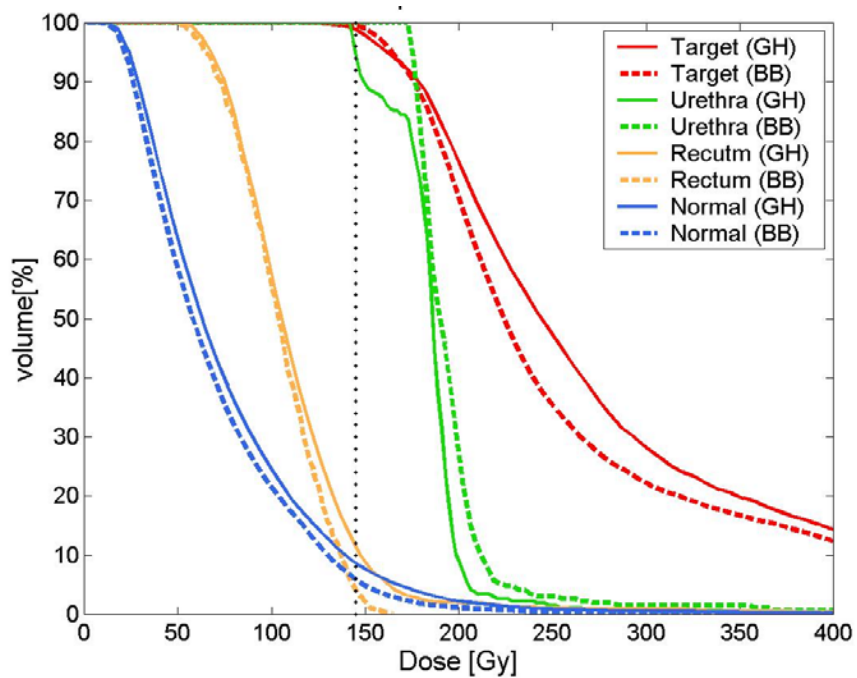
Greedy heuristic



Branch-and-bound

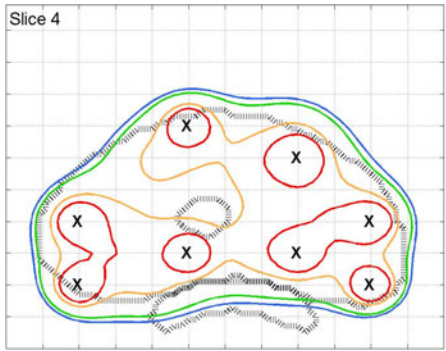
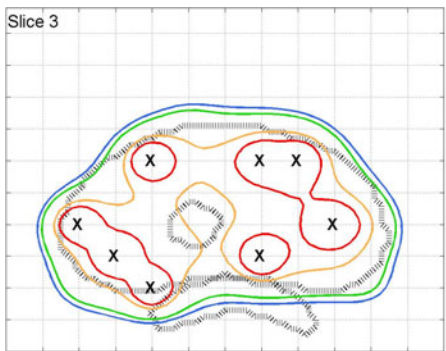
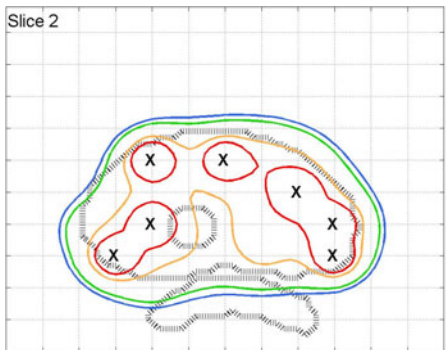
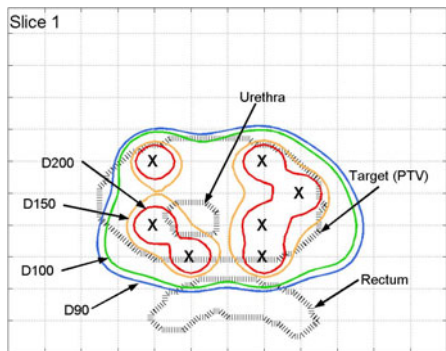


(patient E continued)

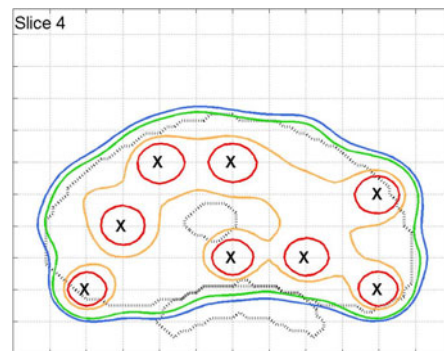
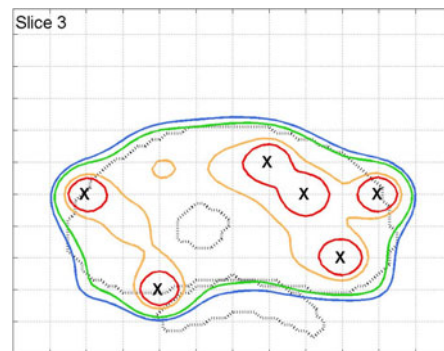
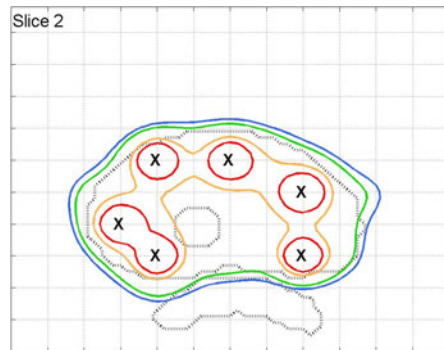
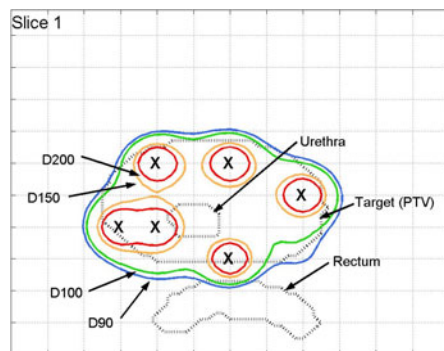


Patient F

Greedy heuristic

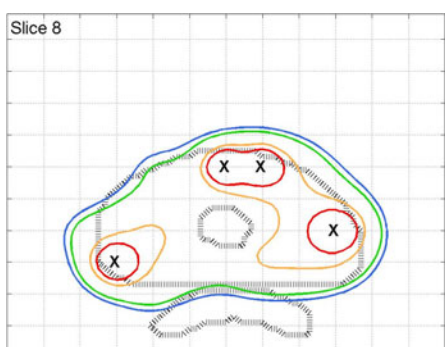
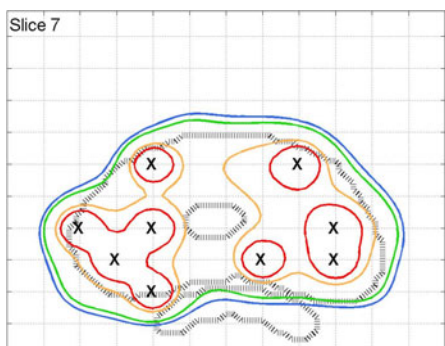
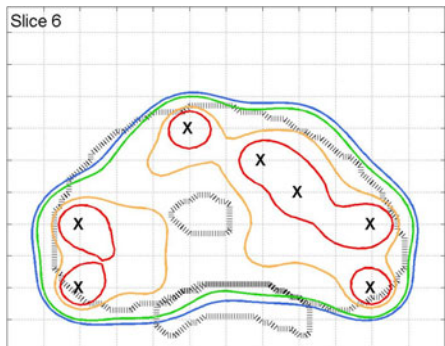
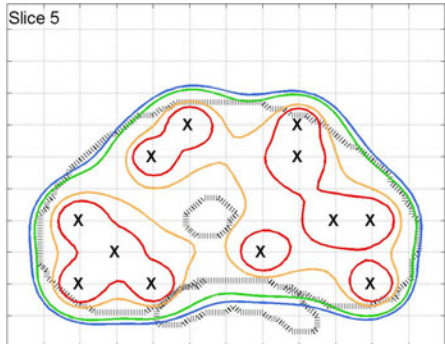


Branch-and-bound

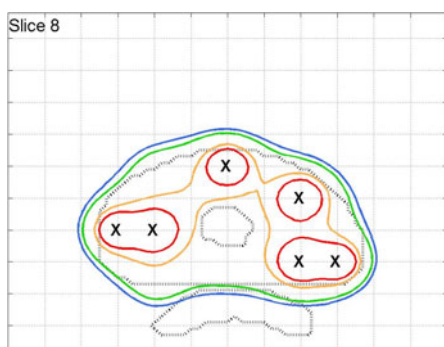
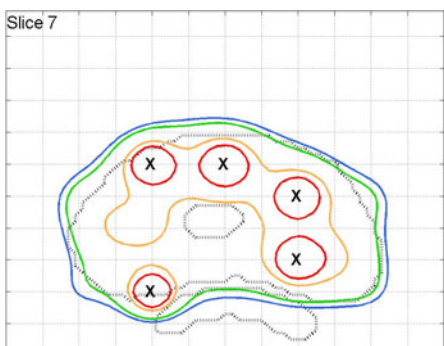
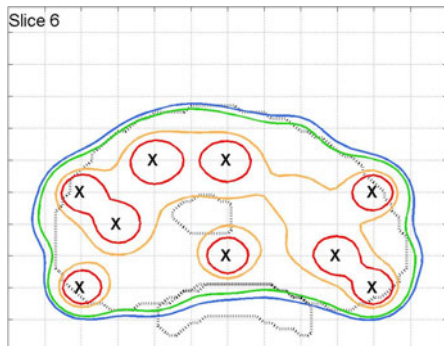
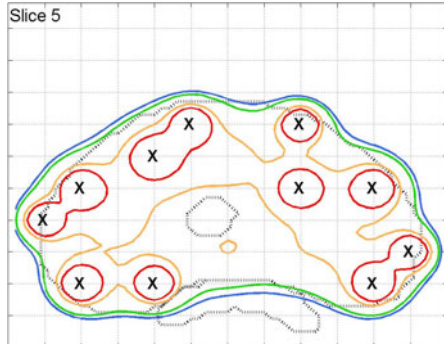


(patient F continued)

Greedy heuristic

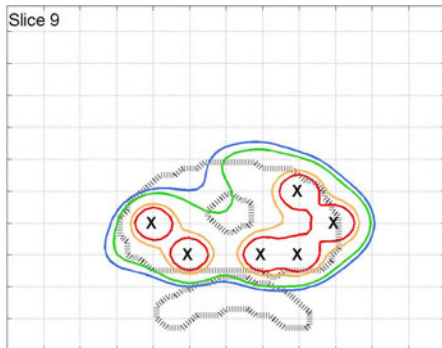


Branch-and-bound

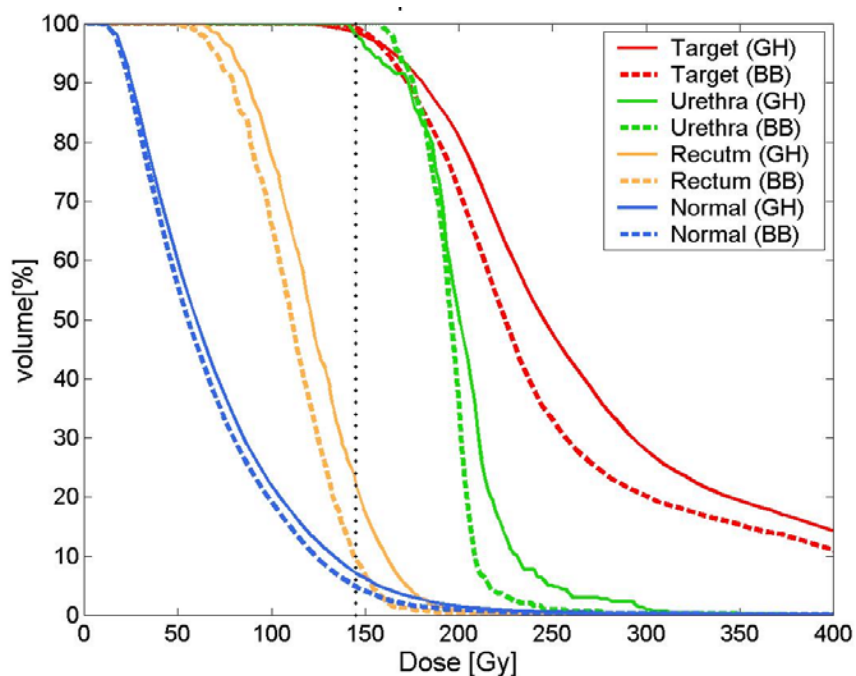
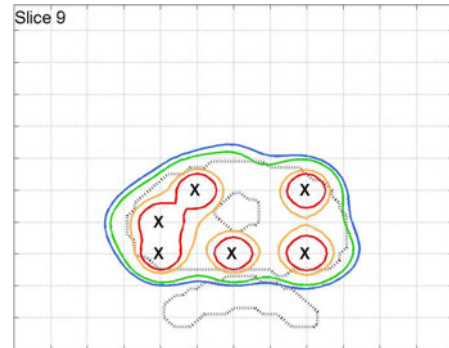


(patient F continued)

Greedy heuristic

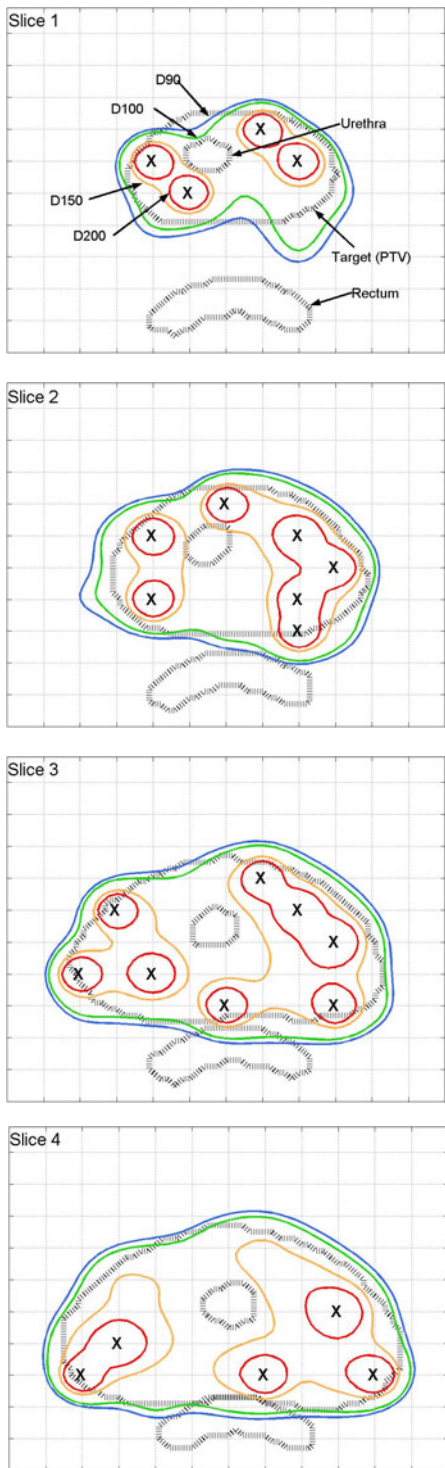


Branch-and-bound

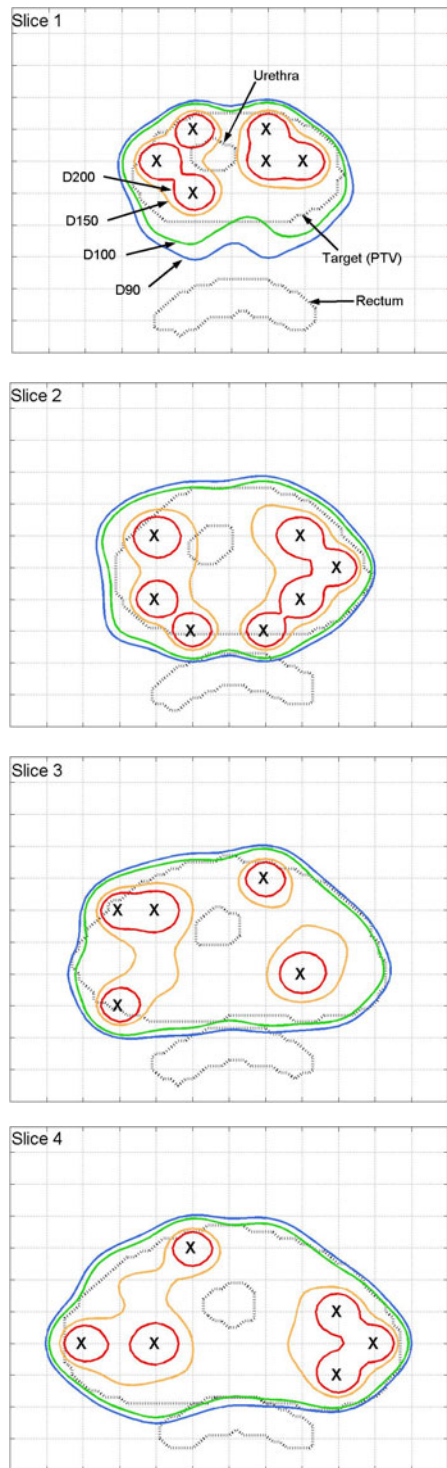


Patient G

Greedy heuristic

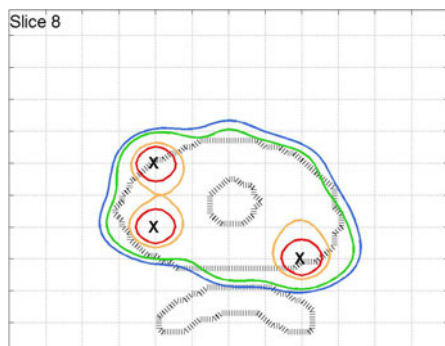
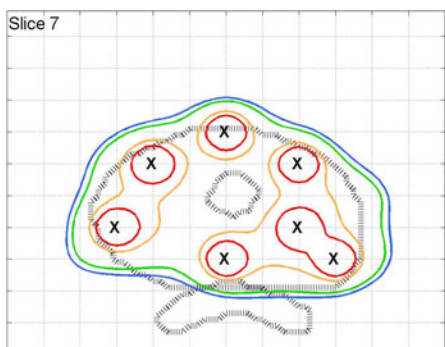
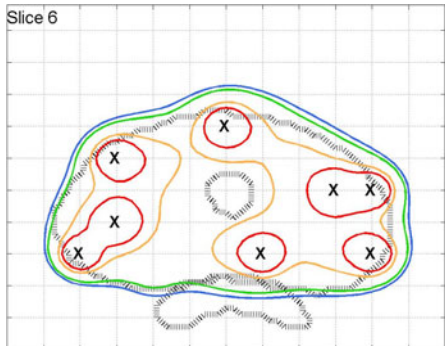
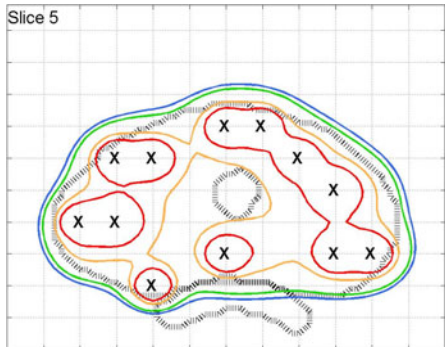


Branch-and-bound

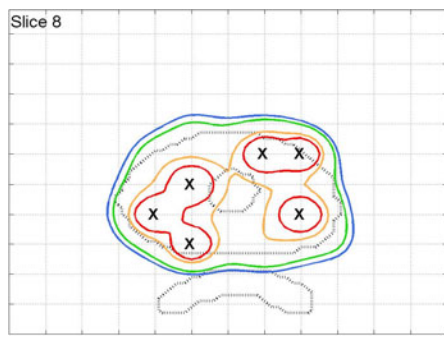
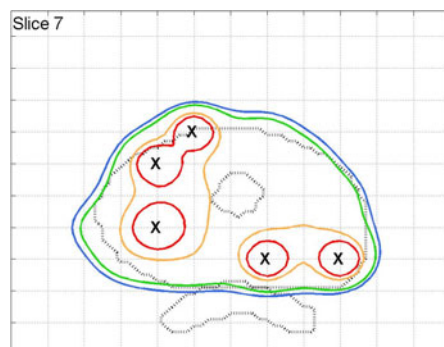
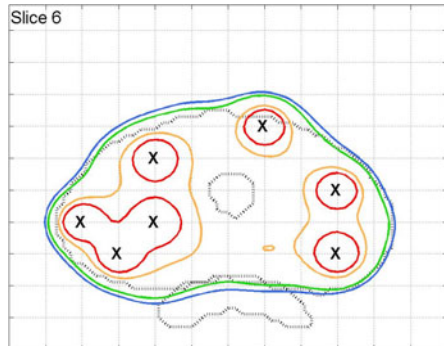
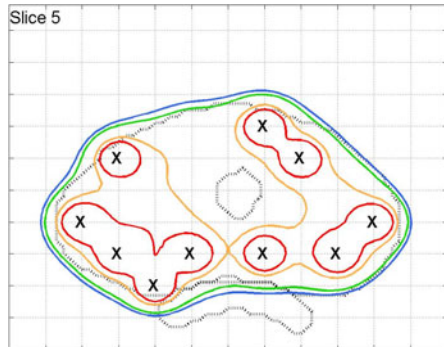


(patient G continued)

Greedy heuristic

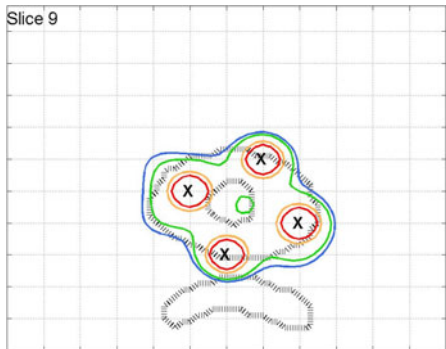


Branch-and-bound

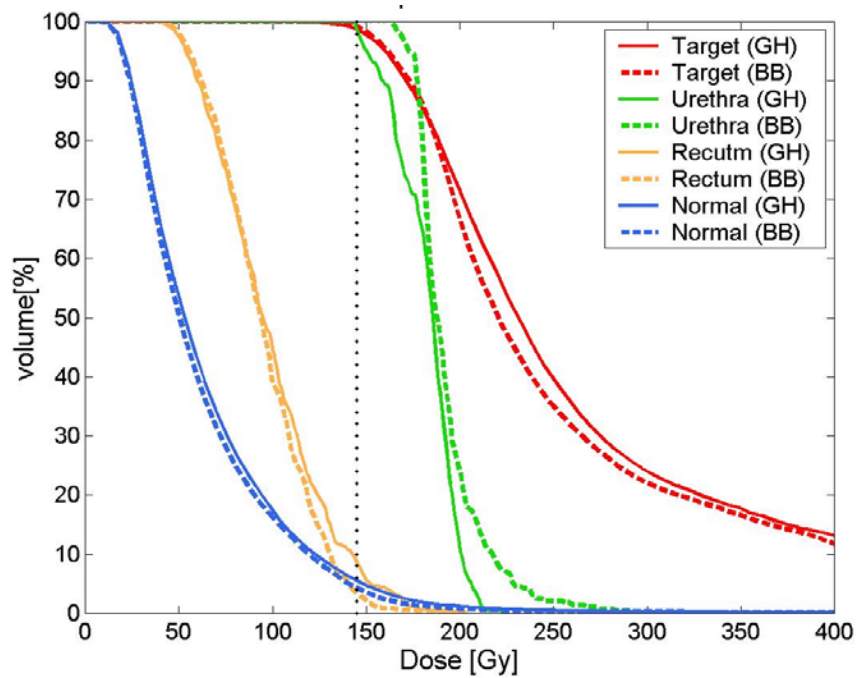
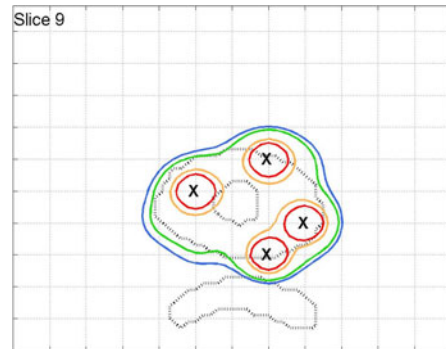


(patient G continued)

Greedy heuristic

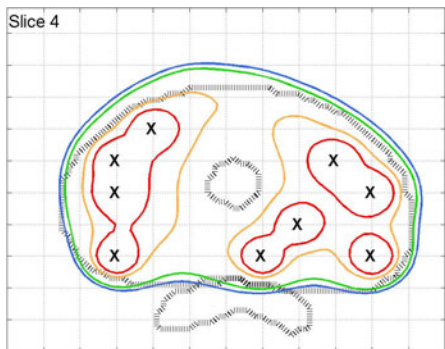
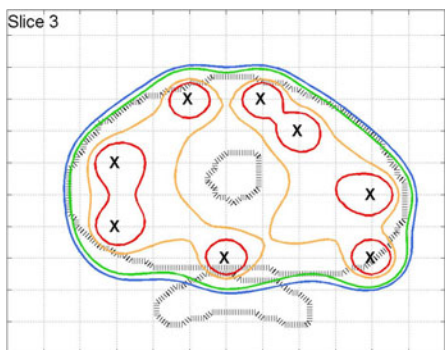
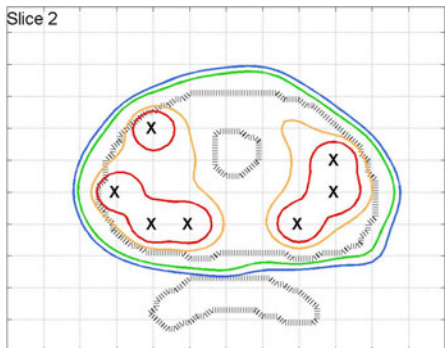
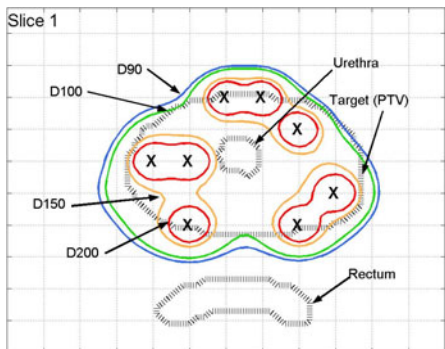


Branch-and-bound

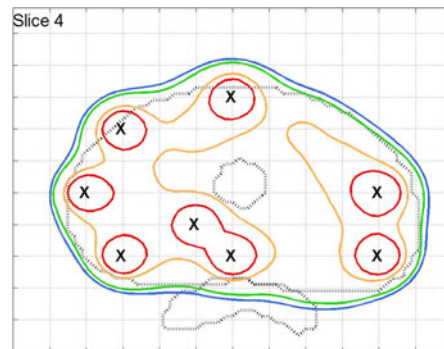
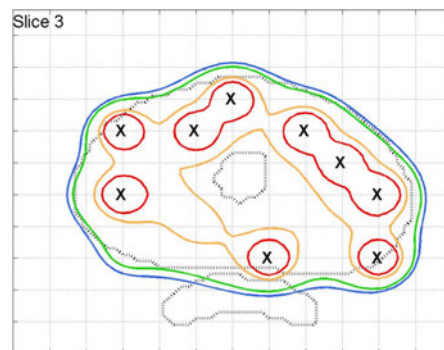
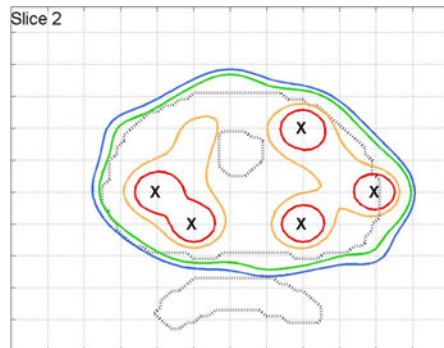
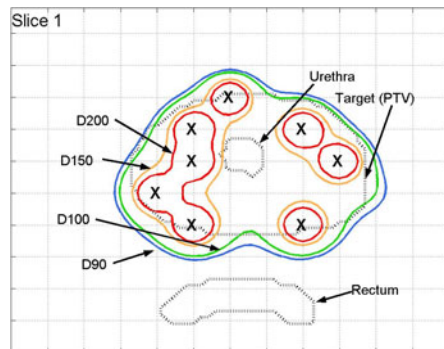


Patient H

Greedy heuristic

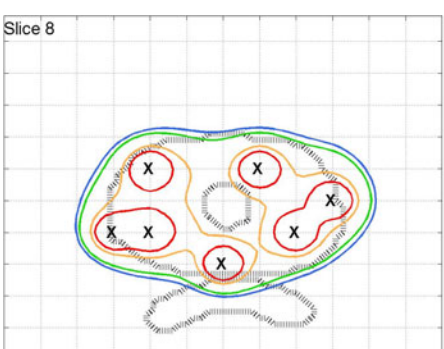
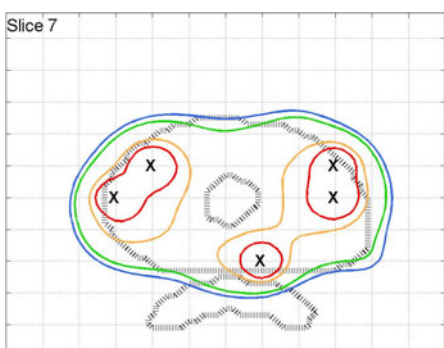
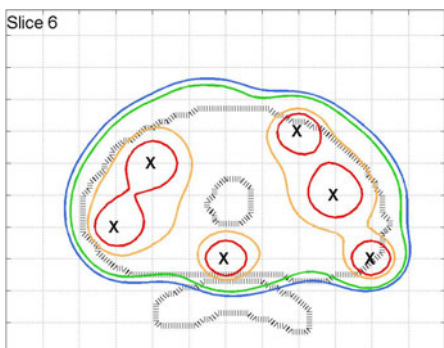
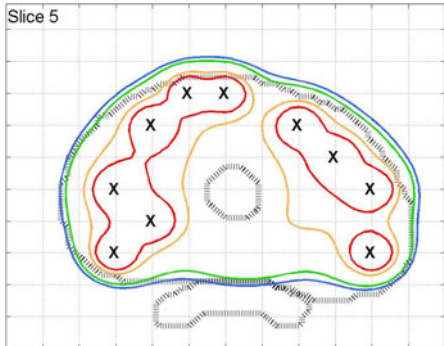


Branch-and-bound

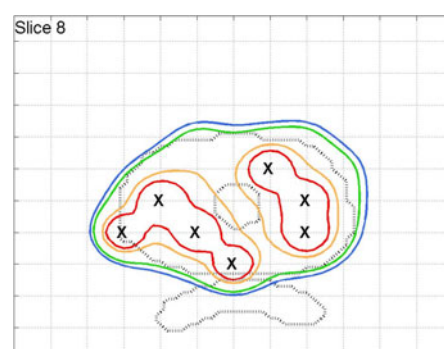
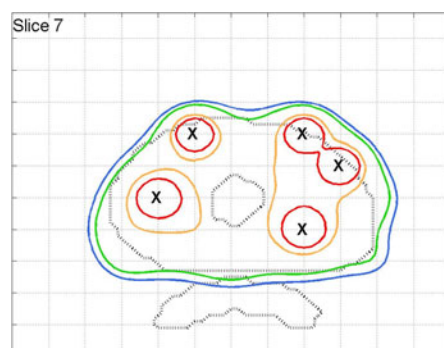
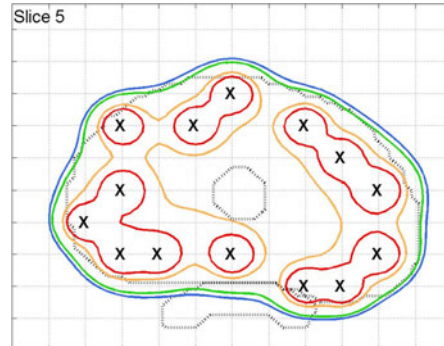


(patient H continued)

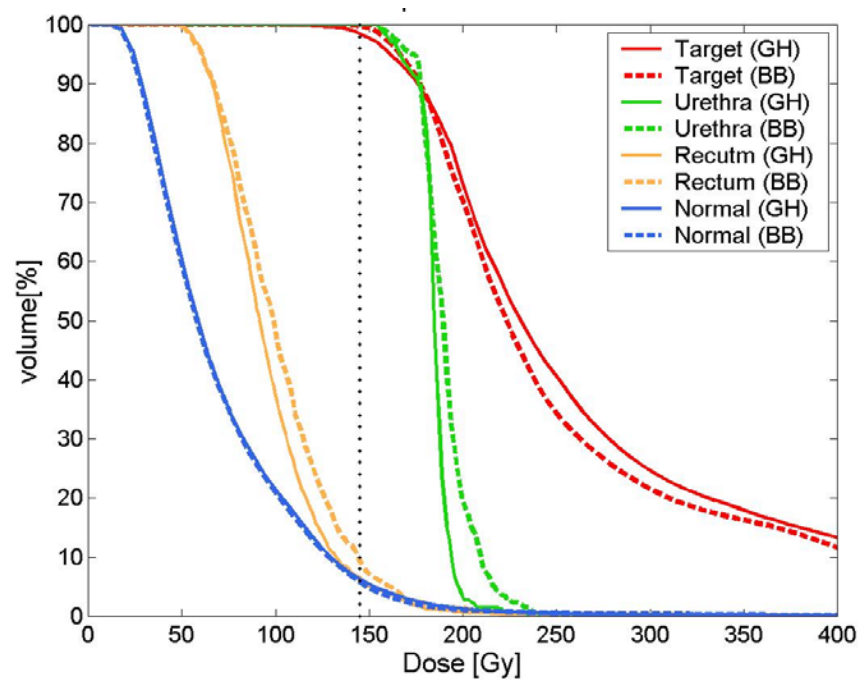
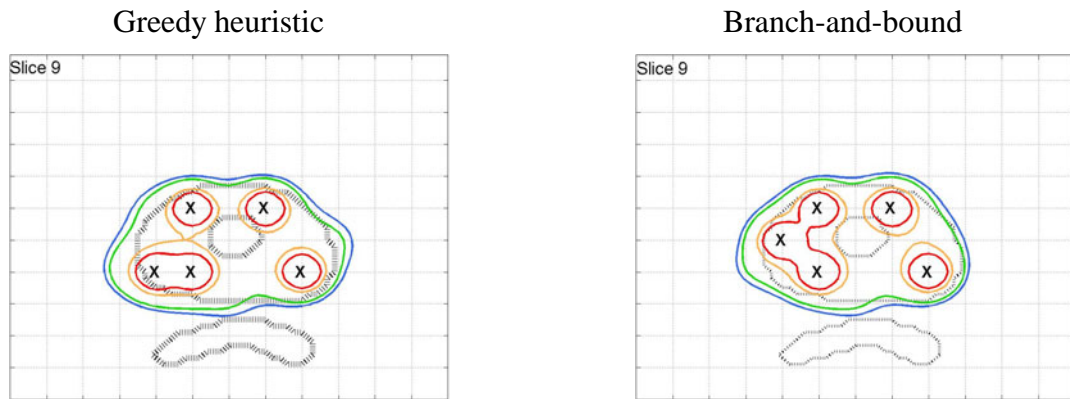
Greedy heuristic



Branch-and-bound

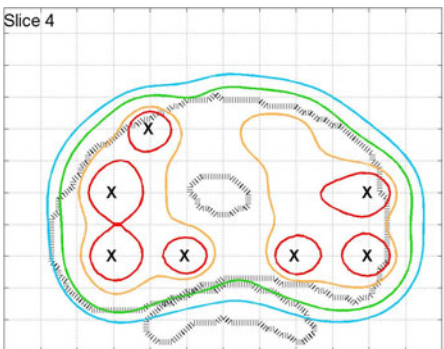
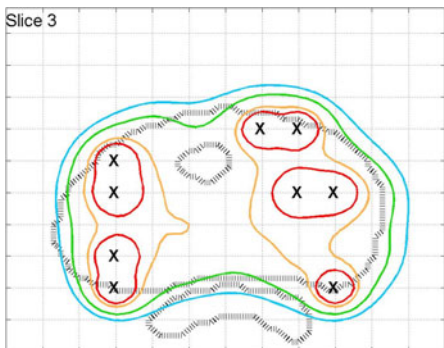
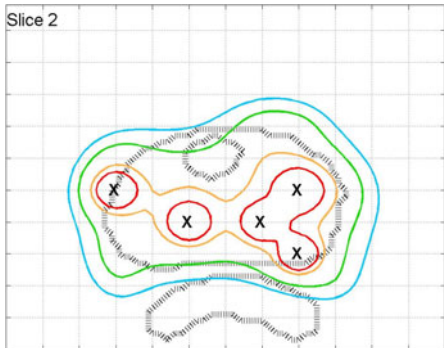
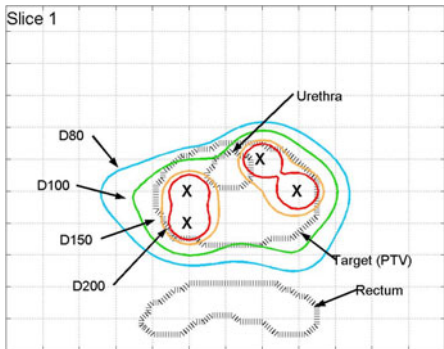


(patient H continued)

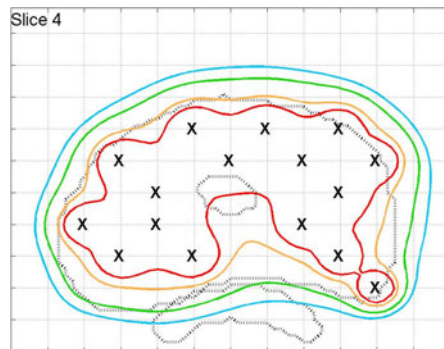
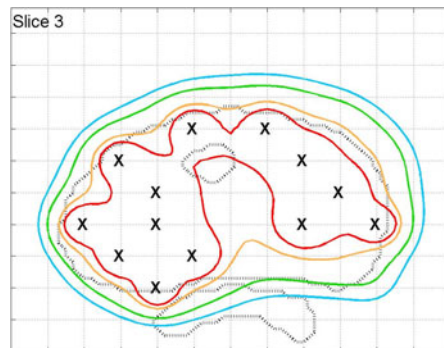
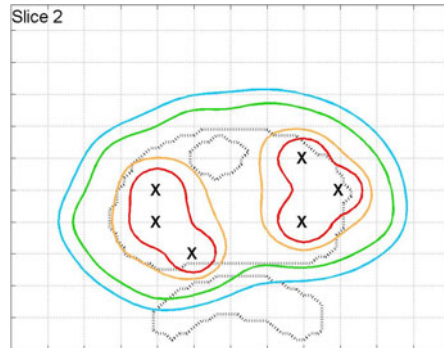
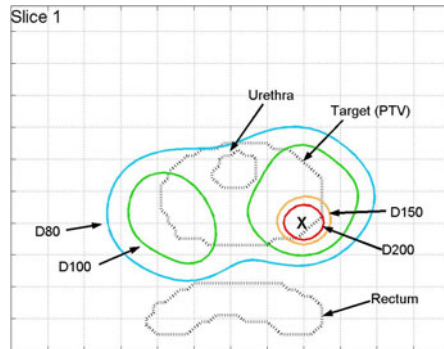


Patient I

Greedy heuristic

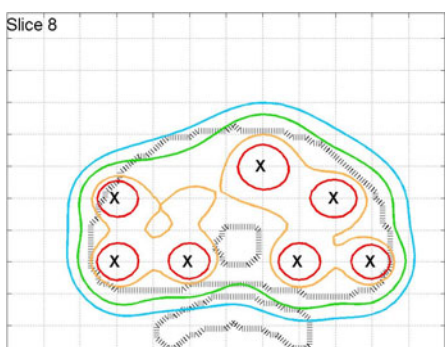
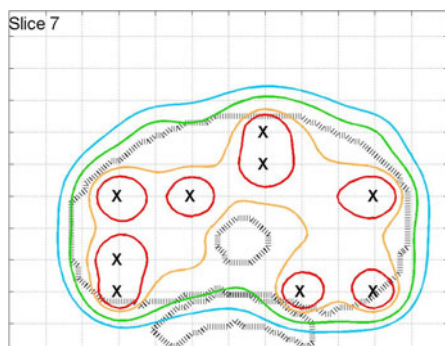
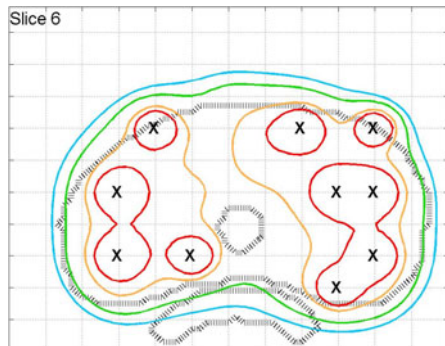
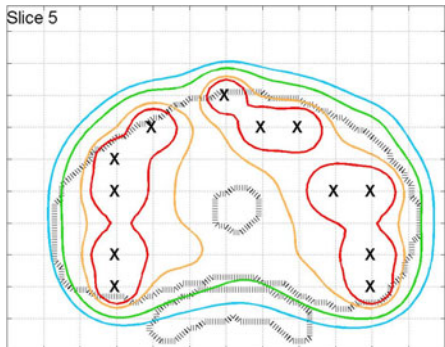


Branch-and-bound

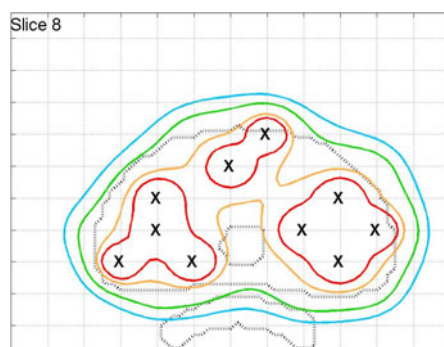
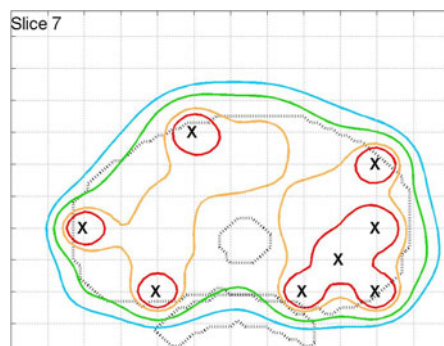
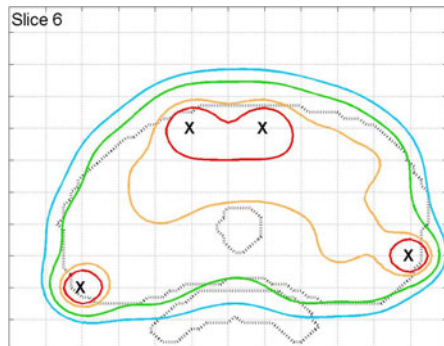
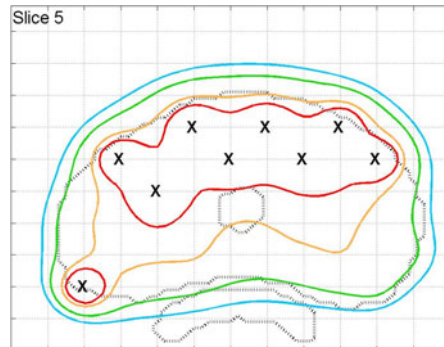


(patient I continued)

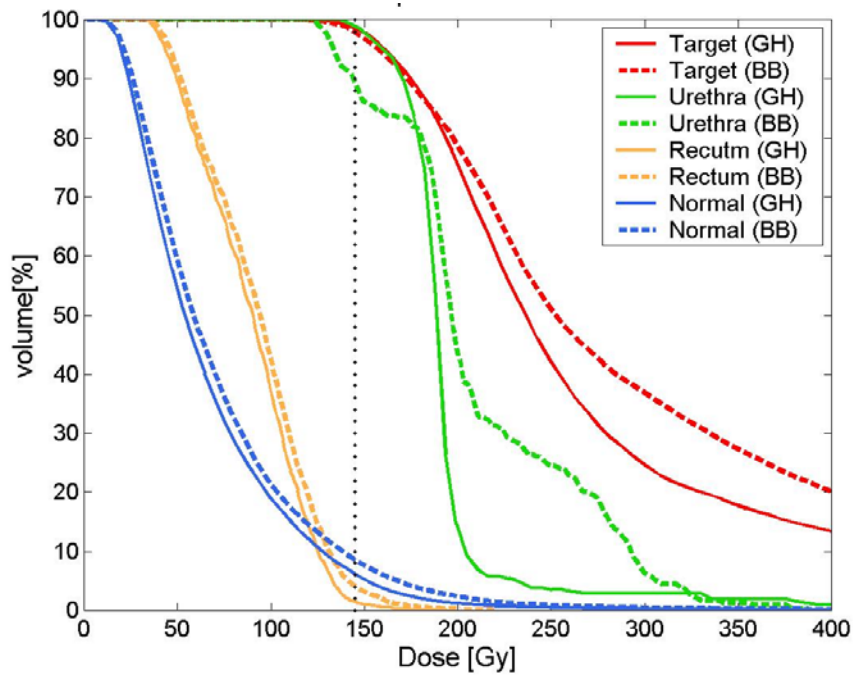
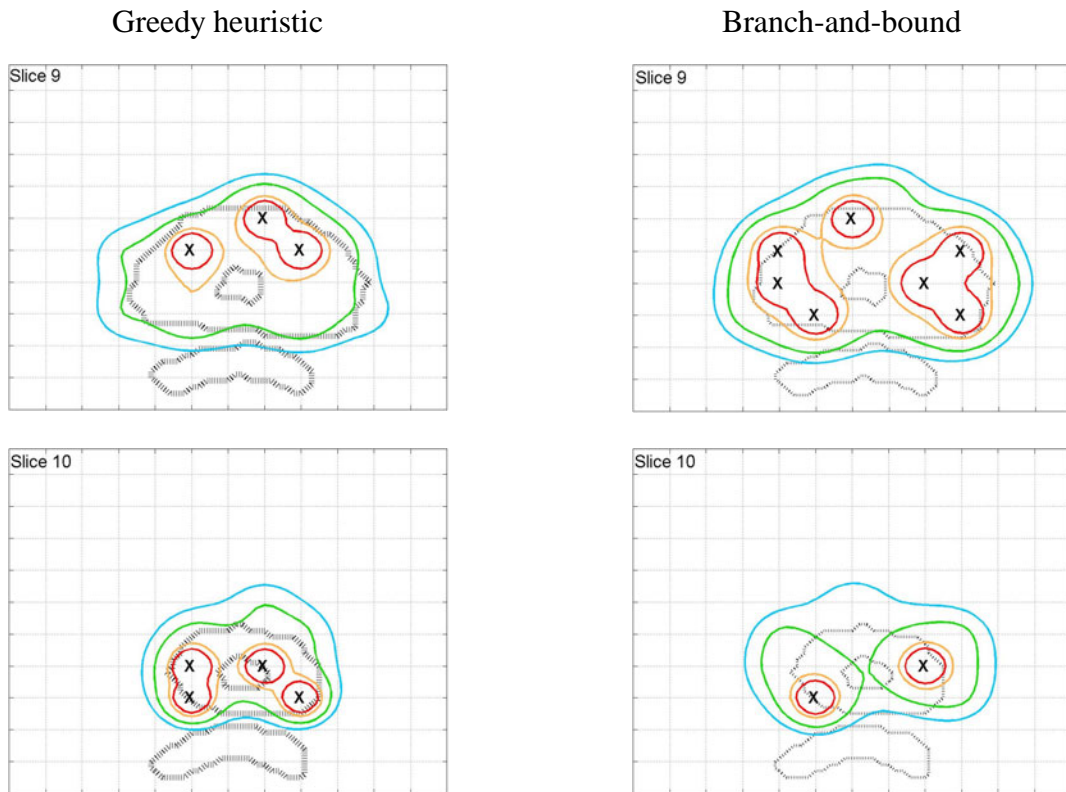
Greedy heuristic



Branch-and-bound

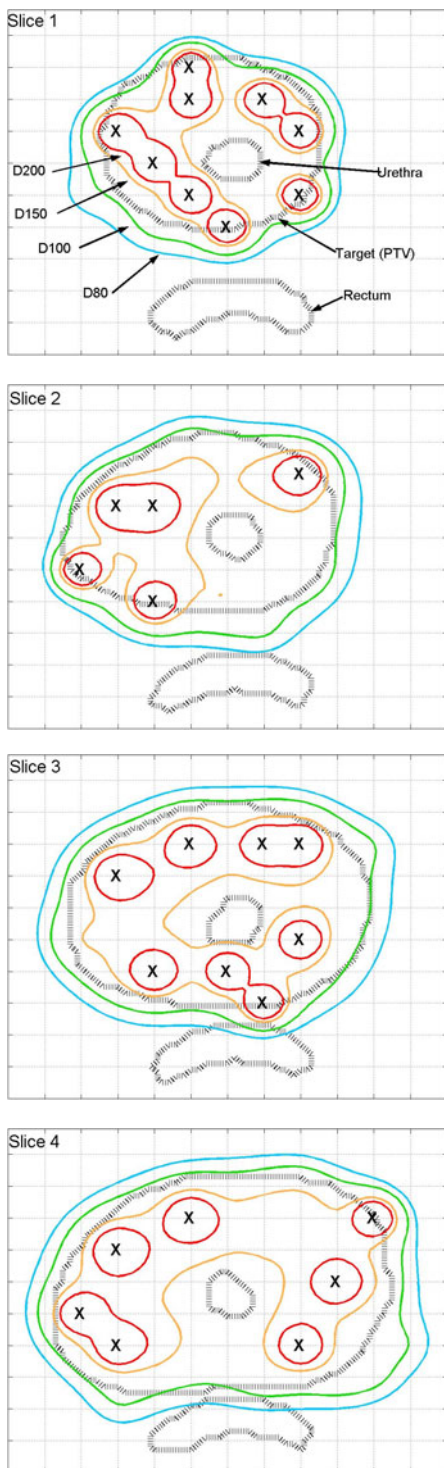


(patient I continued)

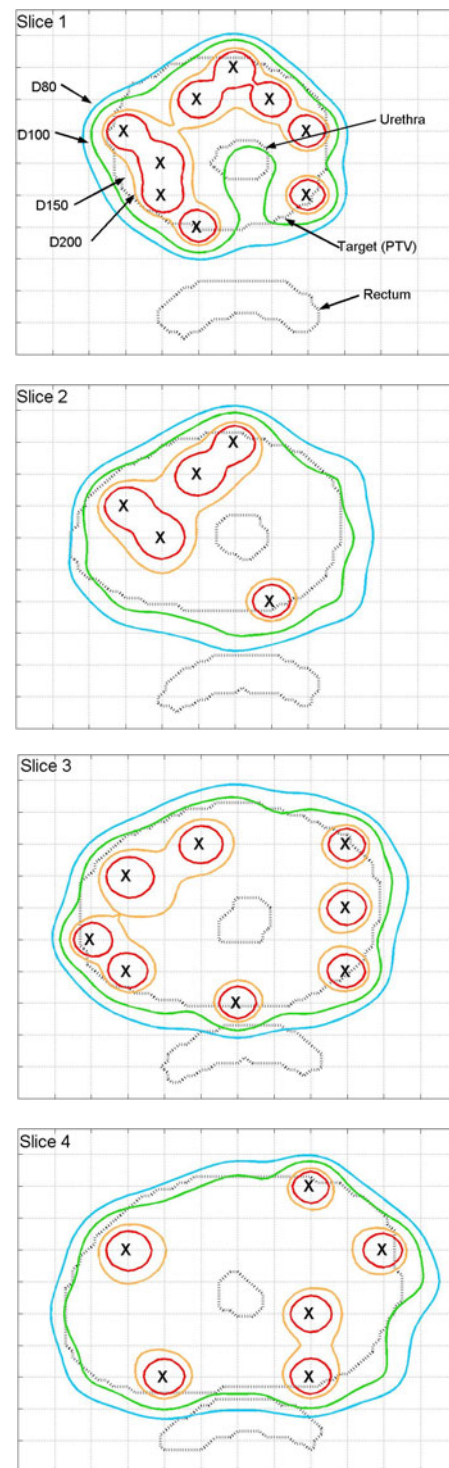


Patient J

Greedy heuristic

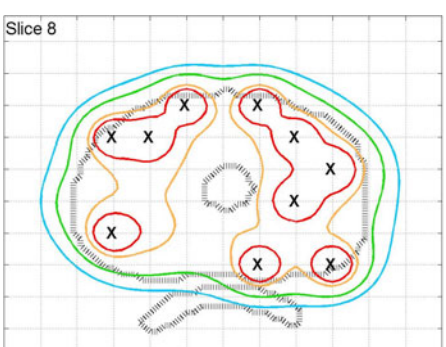
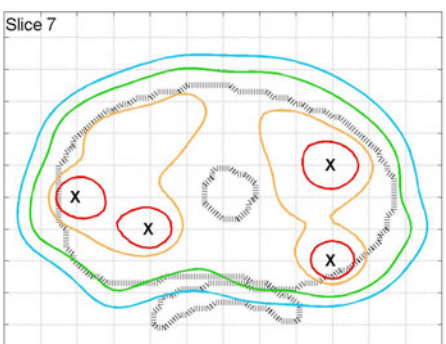
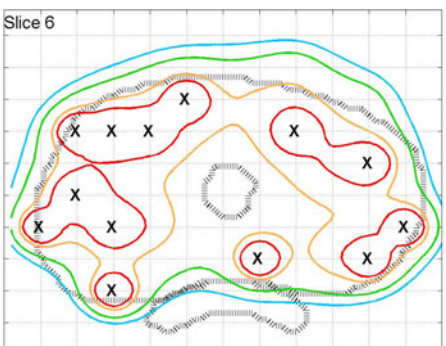
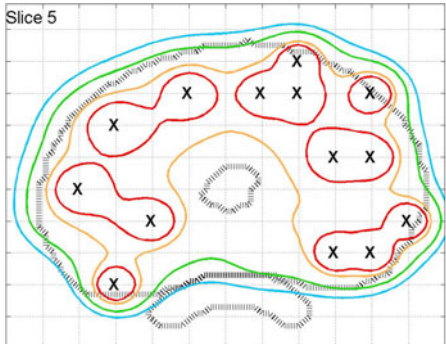


Branch-and-bound

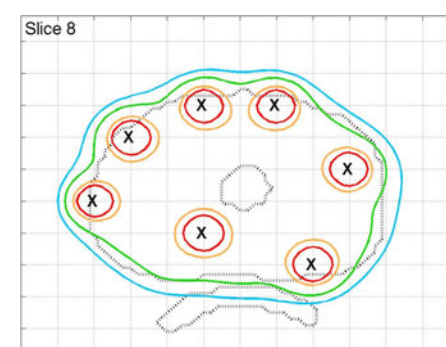
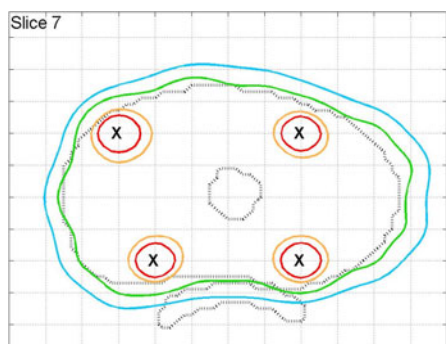
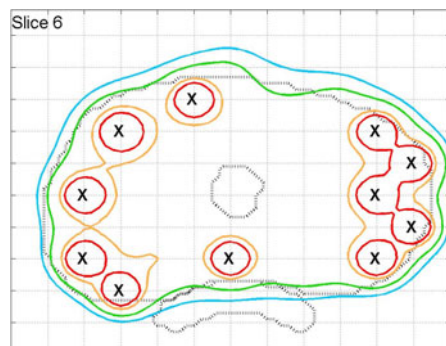
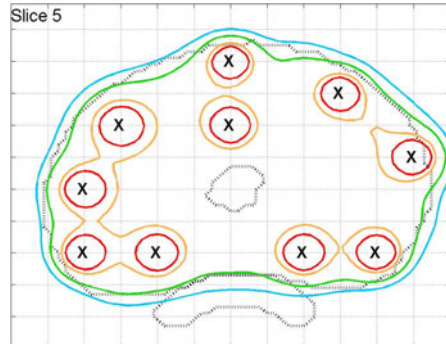


(patient J continued)

Greedy heuristic

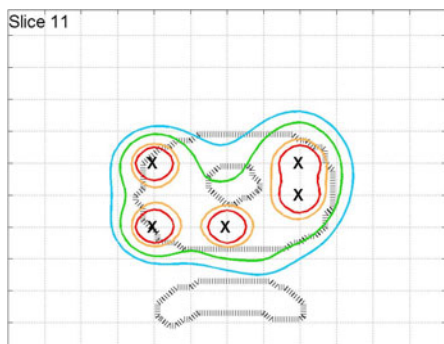
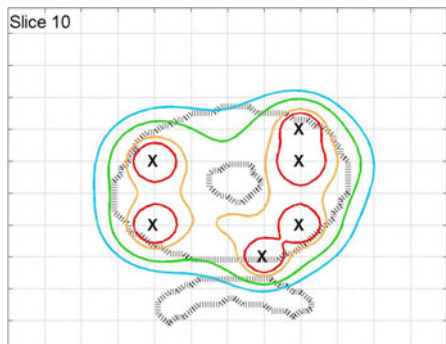
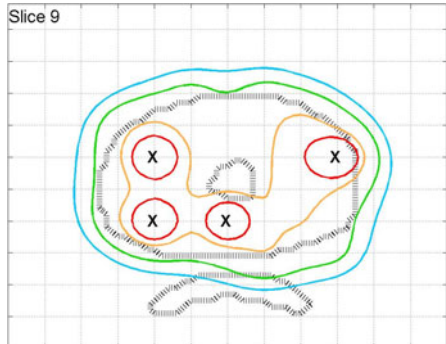


Branch-and-bound

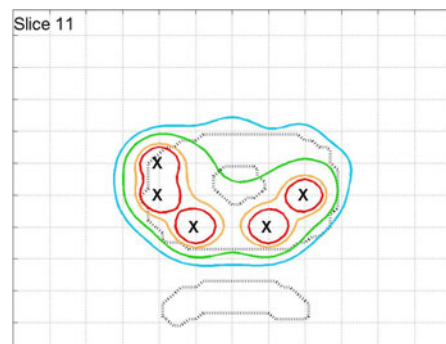
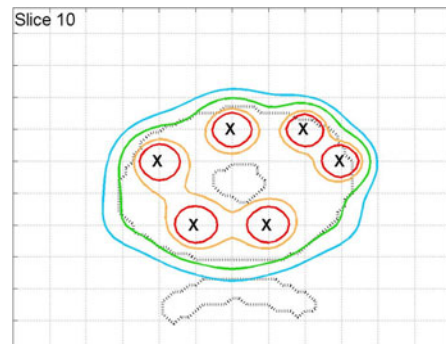
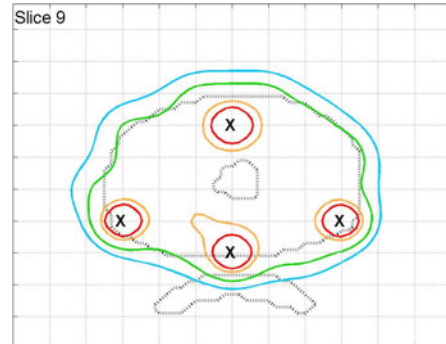


(patient J continued)

Greedy heuristic



Branch-and-bound



(patient J continued)

